Dissertation

vorgelegt von

M.Sc.Eng. Robert Edward Boroch
aus Warschau

Mechanical Properties and Fatigue of Polycrystalline Silicon under Static and High Frequency Cyclic Loading

Dedicated to my Parents

Contents

Acknowledgments

I would like to express my sincere gratitude to everyone who, by their support, encouragement, help or remarks, have contributed to the fulfillment of this work.

I would like to express my deepest thanks to my doctoral supervisor, Prof. Dr. Peter Gumbsch, for his guidance and confidence throughout the entire process and to Prof. Dr. rer. nat. Oliver Kraft for reviewing of the thesis.

I count myself particularly lucky to having pursued this work in the Robert Bosch GmbH Corporate Research for microsystems technology headed by Dr. Stefan Finkbeiner. This department is a great place for an interdisciplinary work, with excellent facilities and helpful, knowledgeable colleagues.

I would like to thank my supervisor and the leader of the reliability group Dr. Roland Müller-Fiedler for giving me the chance of doing my research in his group. The motivating and always constructive discussions, a feeling of freedom and trust as well as his warm support I experienced on **every** stage of my work I will always keep in my memory.

I would like to especially thank our electronics expert Thomas Buck, who, working with full engagement parallel to his Ph.D., created the testing setup for high cycle measurements used in this work, and our FEM specialists Joerg Hauer and Dr. Christian Doering and Dr. Daniel Herrmann for support with numeric simulations.

The work would be much more difficult without the friendly support of Dr. Juergen Graf, Ulrich Kunz, Dr. Edda Sommer, Ralf Boessendoerfer, Antonio Martucci, Dr. Kersten Kehr and Rainer Schink that shared with me their precious experiences and Andreas Horn and Jacek Wiaranowski who made a great job in the lab.

I also want to thank my colleagues from the process group for support in the clean room: Sabine Nagel, Volker Becker and all colleagues from the sensor development department in Reutlingen, especially Dr. Andre Kretschmann, Dr. Patrick Wellner, Dr. Jochen Franz, Dr. Johannes Classen, Johannes Seelhorst, Dr. Nicolaus Ulbrich, Dr. Lutz Mueller, Dr. Heiko Stahl, Dr. Volker Schmitz, Dr. Christian Patak, Udo Bischof and Dr. Christoph Gahn.

As for external support I would like to thank the colleagues from Fraunhofer IWM in Halle. Dr. Matthias Ebert, Jan Schischka and Heiko Knoll. For his very important role I would like to thank my supervisor from IWM Halle Dr. Joerg

Bagdahn for constructive discussions, his expertise and time he spent correcting my thesis.

Finally I would like to thank my parents, without whom I would not be what I am today, and my fiancé Natasa for her patience and support.

Stuttgart, July 6, 2007

1

Introduction

1.1 Motivation and objective of the thesis

In the last years a very fast progression in the field of micro technology has been observed. A lot of products, from ink jet heads to acceleration sensors, are entering the market. Therefore the request for better and more reliable products is still growing. One prerequisite for the widespread use of sensors is low production cost. Silicon micromachining technology offers the possibility to batch-produce sensors, combining standard integrated circuit (IC) technology processes with sensor-specific processing steps, thus effectively reducing the cost compared to conventional devices produced with fine-mechanical technologies [1].
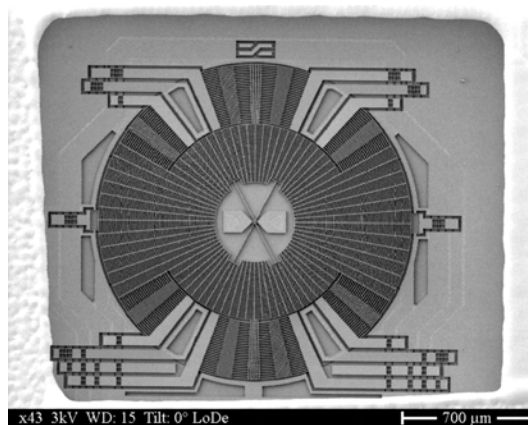
Figure 1.1: SEM image of angular rate sensor fabricated by the Robert Bosch GmbH foundry process using epipoly

An angular sensor produced in silicon micromachining technology is presented in Fig. 1.1 as example of a current marketed mass product.

The implementation of microsystems in automotive applications is certainly one of the driving forces for the breakthrough of Micro-Electro-Mechanical Systems (MEMS) as an industrial technology on the level of mass production. In the

early development phases of microsystems the emphasis was mainly on processes, components and sensor functions. Many of their applications in the vehicles comprise distinct safety features (AirBags, ESP). It is therefore crucial for these micro sensors to assure an accurate, reliable and failsafe operation under very harsh environmental conditions during a lifetime of 10-15 years.
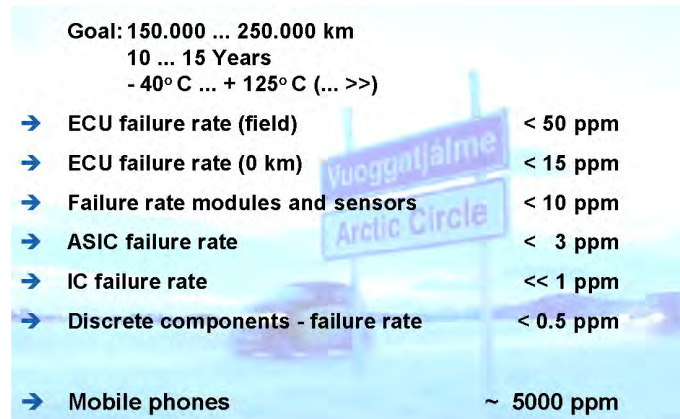
Figure 1.2: Typical reliability requirements in the automotive industry

Typical reliability requirements in the automotive industry are presented in Fig.1.2.

To assure a good quality and high reliability of products, one needs to develop appropriate methods and procedures of material testing in order to gain a better understanding of failure mechanisms, and to be able to predict possible problems and take preventive measures already in the concept and design phase. The expenses to fix problems overlooked in early phases increase drastically with ongoing development.

Generally, there are two major types of failure modes in MEMS built out of brittle materials: static fracture resulting from a high load applied to the functional structure or fatigue fracture associated to changes in the material under a cyclic load. Both will be addressed in the thesis.

Polysilicon as a brittle material exhibits a low strain tolerance and large scatter of observed fracture strengths. The absence of significant plastic deformation [2] and microcracking [3] causes large stress concentrations at microscopic flaws present in the microstructure of every material. The flaw with the most unfavorable combination of size, location and orientation in the stress field will trigger the fracture of the entire component.

The determining strength factor in brittle materials is the size and distribution of the flaws that occur either on the surface or in the interior of the component. Assuming a certain flaw distribution in the material as well as a stress distribution and a given shape of the structure, the size of the structure also becomes an important parameter influencing the fracture strength.

Investigations of strength properties of polycrystalline silicon and characterization of the size effect are the focus of this Ph.D. work. A variety of tensile and bending specimens fabricated in various conditions has been developed and tested. The application of statistic methods based on weakest link theory in strength prediction was also an important part of the thesis.

Various fatigue mechanisms of polycrystalline silicon have been proposed in literature, but one well accepted theory does not exist so far [4]. Investigations of fatigue behavior of Bosch polysilicon under cyclic loading of up to 10^{12} cycles have been conducted in this work. A novel testing device that allows parallel testing of up to 32 specimens has been designed especially for these investigations. Specimens used had a resonance frequency of approximately 90kHz which allows to conduct high-cycle measurements with a relatively good statistic basis. This is extremely important to asses the scatter of results for brittle materials. The existing fatigue mechanisms are discussed in comparison with the experimental results obtained.

The thesis consists of eight Chapters. Chapter one gives a short introduction to the objective of the thesis. In Chapter two a description of test specimen fabrication is given also chip packaging processes as well as material variations in fabrication are introduced.

Chapter three presents basic concepts of linear elastic fracture mechanics, results of literature research on deposition, test methods and mechanical properties of polycrystalline silicon. The Weibull weakest link theory and statistical methods of strength prediction are also described in Chapter three.

Chapter four gives detailed information about measurement techniques and test specimens used in the investigations. The description of strength and fatigue investigations as well as presentation of the results are given in Chapter five. In addition to measurement results that indicate decrease of fracture strength with growing size of specimens, degradation of polysilicon strength under cyclic high stress loading and strengthening under low stress cyclic loading, the fractography took an important place in the thesis.

In Chapter six the results are critically discussed. Chapter seven briefly summarizes the most important results. In the Chapter eight an Outlook is given.

2

Specimens fabrication - the Bosch polysilicon

2.1 Bosch standard foundry process

The material investigated was fabricated using the Bosch mass production micromechanical process.

The Bosch foundry process features a polycrystalline n-doped silicon layer, with a thickness of 10 and 20 μm for the freestanding structures deposited on 6 inch silicon wafers. The surface micromachining of freestanding polysilicon structures consists of several steps presented as follows Fig. 2.1.

Step 1. Substrate, (100) n-type silicon wafer, with resistivity of 1-2 Ω/cm^2, is heated in the atmosphere of the oxygen, resulting with the oxidation of the surface. The 2μm thick layer of SiO_2 serves as electrical isolation between the functional structures and the wafer as well as the sacrificial layer.

Step 2. Deposition of the photoresist and lithographic definition of structure shape. In the following etch step the unwanted resists are removed.

Step 3. The sacrificial layer is structured by etching of regions not covered with photoresist. The following etch step removes the rest of photoresist from the SiO_2 surface.

Step 4. Deposition of polysilicon on the whole area of the wafer.

Figure 2.1: Schematic view of polysilicon micromachining process [5]

Step 5. Deposition and structuring of the photoresist.

Step 6. Structuring of polysilicon functional layer using an anisotropic dry etch technique [6].

Step 7. Release of freestanding functional structures through removal of the sacrificial layer with vapor hydrofluoric acid.

The epitaxial deposition of polysilicon is preceded by the deposition of a 450nm thick seed polysilicon layer with the use of Low Pressure Chemical Vapor Deposition. The layer consists of small randomly oriented silicon crystals serving as a start layer for the epitaxial deposition of a thick polysilicon layer. During epitaxial growth from the substrate gas $SiHCl_3$ at a temperature of 1150°C the layer is n-doted with the additives of PH_3. The grains grow in a columnar structure, nearly perpendicular to the interface with the sacrificial layer. The columnar structure of polysilicon is shown on Fig. 2.2.

With the use of electron back scattering diffraction (EBSD), it was found that the majority of grains have a {110} out-of-plane orientation. The resulting film has a very high roughness. Chemical Mechanical Polishing is used to reduce the roughness to approximately 5nm and achieve the expected thickness.
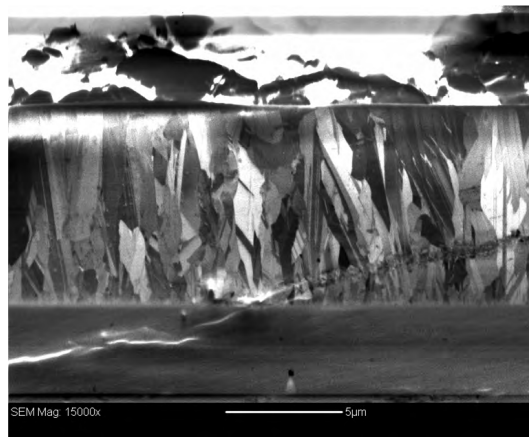

Figure 2.2: Backscatter Electron (BE) image of cross-section image of the polysilicon film
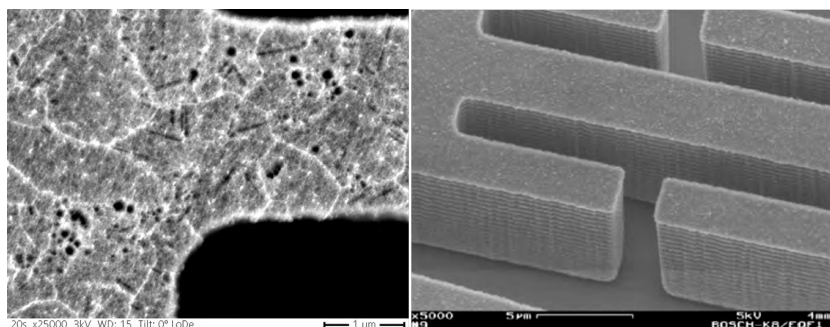

Figure 2.3: Left: top view of the polysilicon microstructure. Grains decorated with Secco etch (HF + $K_2Cr_2O_7$ + H_2O); Right: typical look of the side walls structured with a Bosch process

A special trench technique based on alternating steps of etching with gaseous

SF_6 and passivation with Teflon-similar C_4F_8, allows the formation of vertical side walls with high aspect ratio Fig. 2.3.

The structuring trench process results in a change of dimensions compared to the layout values. Through inhomogeneity of the etching process the width of the structures varies slightly across the wafer and considerably between the wafers. The real width is electrically measured on five positions on the wafer during fabrication process and documented in the charge file. The mean value of all five measurements is taken as a real values for calculation in this work. Typically the structure is 0.60μm narrower than on the layout drawing.

2.2   Glass frit bonding process

The hermetic package is a crucial element to ensure high reliability and lifetime of micro mechanical sensors in automotive applications [7]. The package of the sensors, at wafer-level, protects the micro mechanical structures and has to guarantee a hermetic enclosure during the entire sensor lifetime of up to 20 years.
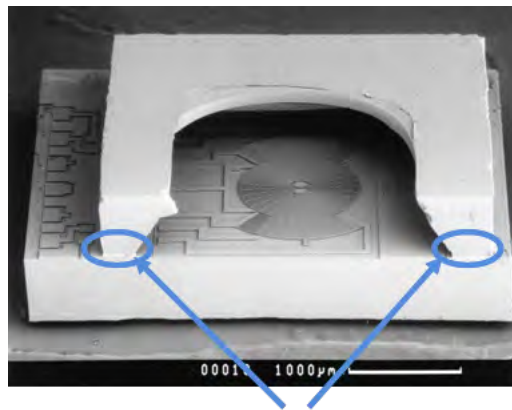
Figure 2.4: Glass frit bonded gyroscope for automotive applications (opened package) [7]

Test specimens used for fatigue investigations in this work are encapsulated with a silicon cap assembled in glass frit bonding process (Fig. 2.4).

Low melting point glasses have been used in industry for many decades for forming hermetic seals. The bonding paste material consists of glass powder, organic binders and solvents and has the form of low viscosity paste. The thermal expansion coefficient of the glass paste is usually adjusted to that of the bonded materials e.g. silicon by admixing certain types of mineral particles to the glass matrix.

The glass frit bonding process is carried out in five steps (Fig. 2.5). In the first step, the glass material is deposited and structured with high precision onto
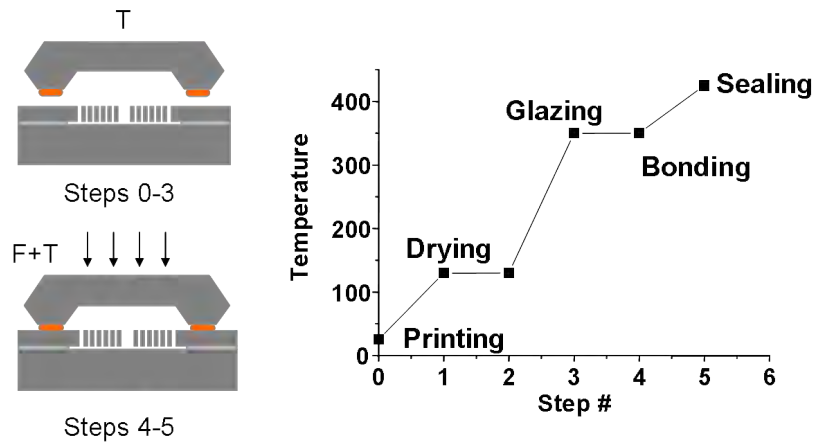
Figure 2.5: Schematic view of glass frit bonding process

the bonded chip surface by means of screen printing. Afterwards, the paste undergoes structural change by a multi-step temperature process, involving removing organic components from the system. In the next step the cap wafer with the glass layer is bonded to the sensor wafer at a temperature of around 450°C. During bonding, a force is applied to the wafer, which leads to a viscous flow of the glass, increasing the bond frame width while reducing its thickness. The bonding process is carried out in vacuum of 10^{-3} bar. The pressure and atmosphere inside of the chip depend on the process conditions. The resonant specimens for the fatigue investigations used in this thesis were driven at the pressure of 1-2mbar.

2.3 Special conditions in polysilicon films processing

In order to investigate the influence of surface quality and composition on fracture strength, the polysilicon test specimens were fabricated with modified processing conditions. For not bonded wafers aimed for static strength measurements the bonding process was simulated through the temperature treatment up to 400°C after micromachining steps ('Temperature'). Extended stripping time has been applied to improve removal of remaining organic residues covering the polysilicon ('Stripper') after the trench process. To investigate the influence of surface silicon oxide on fracture strength, the oxidation of polysilicon was promoted in an ozone atmosphere after releasing the structure by etching of the sacrificial layer ('Ozone'). The roughness of the side-walls has also been modified by changing the etching/passivation ratio in the trench process ('Trenching param.').

3

Fundamentals

3.1 Linear elastic fracture mechanics

3.1.1 An atomic view of fracture

A material fractures when sufficient stress and work are applied on the atomic level to break the bonds that hold atoms together. The bond strength is supplied by attractive forces between atoms. The equilibrium spacing r_0 occurs when potential energy is at a minimum [8].
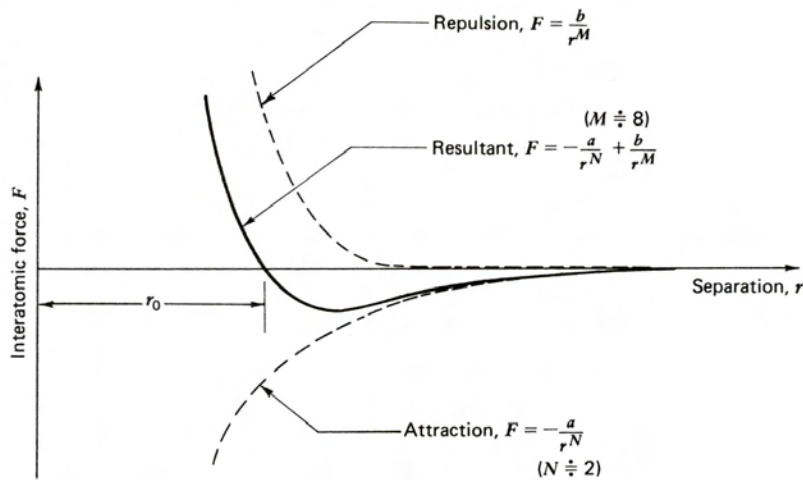
Figure 3.1: Attraction and repulsion forces of an atom as a function of atomic separation [8]

Fig. 3.1 shows schematic plot of attraction and repulsion forces as a function of atomic separation.

Typically the cohesive stress σ_c can be can be approximately estimated as

$$\sigma_c \approx \frac{E}{2\pi} \tag{3.1}$$

3.1.2 Stress concentration effect of flaws

A discrepancy of typically three to four orders of magnitude between estimated and real strength of materials is observed. It is expected that flaws lower the global strength by magnifying the stress locally [8]. Stress analysis by Inglis of an elliptical cavity in a uniformly stressed infinite plate was the important precursor to the Griffith studies described in next section. Analyzing the Y-axis stress component in different places of the crack, the highest value calculated by Inglis was in the point A (Fig. 3.2). The maximal stress was calculated to be:

$$\sigma_A = \sigma \left(1 + \frac{2a}{b} \right) \tag{3.2}$$

The ratio σ_A/σ is defined as the stress concentration factor.
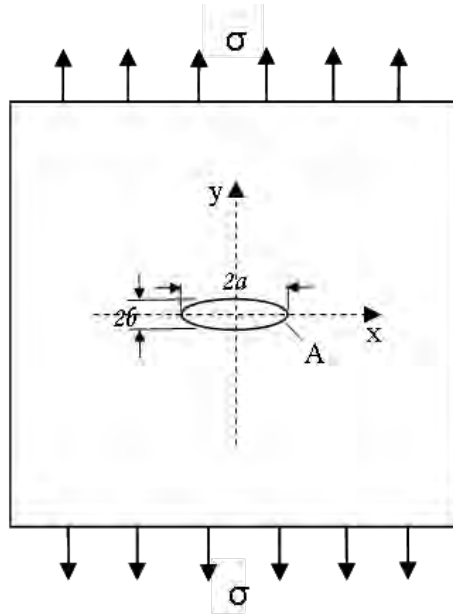
Figure 3.2: Elliptical crack subject to a uniform tensile stress σ

Analysis is based on the assumption that the hole is not influenced by the plate boundaries and that Hooke's law holds everywhere in the plate. The model elliptic hole becomes similar to a real sharp crack when dimension, a, increases relative to, b. The stress in the crack tip can be expressed in terms of radius of curvature ρ as follows.

$$\sigma_A = \sigma \left(1 + 2\sqrt{\frac{a}{\rho}} \right) \tag{3.3}$$

3.1.3 Griffith energy-balance concept

Griffith modeled a static crack as a reversible thermodynamic system [2]. A crack can form, or an existing crack can grow, only if such a process causes the total energy to decrease or to remain constant [8]. The Griffith energy balance for an incremental increase of crack area, dA , under equilibrium conditions can be expressed in the following way:

$$\frac{dE}{dA} = \frac{d\Pi}{dA} = 0 \text{ or } -\frac{d\Pi}{dA} = \frac{dW_S}{dA}$$ (3.4)

Where E is total energy, Π is the potential energy supplied by the internal strain energy and external forces, and W_s is the work required to create new surfaces.

Griffith used the Inglis analysis considering the case of an infinitely narrow elliptical crack to calculate the fracture stress:

$$\sigma_f = \left(\frac{2E\gamma_S}{\pi a}\right)^{1/2}$$ (3.5)

where E is the total energy, and γ_S is the surface energy, and a is the crack radius.

The fracture stress for a penny-shaped flaw embedded in the material can be found in [8].

3.1.4 Crack-tip field and stress-intensity factor
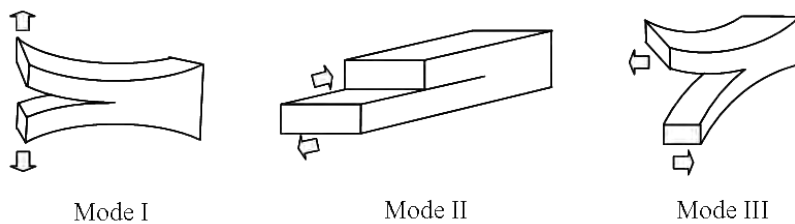
Figure 3.3: The three modes of fracture: I, opening mode; II, sliding mode; III, tearing mode [2]

There are three types of loading that a crack can experience, all are schematically presented in Fig. 3.3. For certain crack configurations subjected to external loading the expressions for stresses in the body have been derived under the assumption of isotropic linear elastic material behavior.

The stress intensity factors can be determined from remote loads and the geometry of the crack by experiment or numerical analysis. For the simple con-

figuration of an edge crack in a semi-infinite plate subjected to remote tensile testing, a closed-form solution can be expressed as [9]:

$$K_I = 1.12\sigma\sqrt{\pi a} \tag{3.6}$$

Solutions for more complicated systems can be found in literature [8].

3.2 Statistical methods in strength prediction of brittle materials

Brittle materials exhibit a low strain tolerance and large scatter of observed fracture strengths. The fracture strength is defined as the normal stress at the beginning of fracture. The absence of significant plastic deformation and microcracking causes large stress concentrations at microscopic flaws, unavoidably present in the microstructure of every material [2,3]. The flaw with the most unfavorable combination of size, location and orientation in the stress field will trigger the fracture of the entire component. Probabilistic component design involves predicting the probability of failure for a mechanically loaded component based on simple specimen strength data. Typically, the fracture strength of material is measured using a simple geometry such as a bend or tensile test specimen. A load is applied until fracture occurs and statistical strength and fatigue parameters are determined from the experimental results. Using these statistical parameters and the results obtained from a finite element analysis, the probability of failure for a component with complex geometry and loading can be predicted [10, 11, 12, 13].
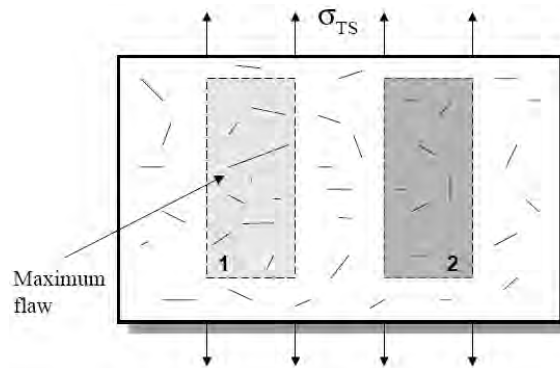
Figure 3.4: Schematic plot for illustration of the size dependent material strength based on the weakest link (biggest flaw) theory [10]

Designing brittle components, including MEMS, to survive in severe loading applications involves the disciplines of statistics and fracture mechanics. Successful application depends on proper characterization of material properties and the use of a probabilistic brittle material design methodology. The underlying Weibull theory is based on the weakest-link (biggest flaw) concept which assumes that the

structure is analogous to a chain with many links [14, 15, 16, 10]. Each link may have a different limiting strength. When a load is applied to the structure such that the weakest link fails, the structure then fails (Fig. 3.4).

For uniaxially stressed components, the two-parameter Weibull distribution for surface residing flaws describes the component failure probability, P_f, as:

$$P_f = 1 - e^{\left(-\frac{\sigma}{\sigma_\theta}\right)^m} \tag{3.7}$$

where σ_θ is the Weibull characteristic strength for a certain test geometry and σ is the applied load.

Alternatively, the probability of failure can be written as:

$$P_f = 1 - e^{-\int \left(\frac{\sigma(x,y,z)}{\sigma_{0A}}\right)^m dA} \tag{3.8}$$

we can define

$$A_{eff} = \int \left(\frac{\sigma}{\sigma^*}\right)^m dA \tag{3.9}$$

so that

$$P_f = 1 - e^{-\left(\frac{\sigma^*}{\sigma_{OA}}\right)^m A_{eff}} \tag{3.10}$$

A is the surface area, $\sigma(x, y, z)$ is the uniaxial stress at a point location on the body surface, and m and σ_{0A} are the modulus and scale parameter of the Weibull distribution, respectively. σ^* is the highest stress value in the model of the object. Depending on the nature of the strength-controlling flaw, the failure probability can also be treated as volumetrically dependent. An analogous equation based on volume can be derived for flaws residing within the body of the component.

The Weibull modulus is a measure of the dispersion of strength (a larger value of 'm' equates to a narrower distribution) while the scale parameter is the strength of a unit area of material at 63.21% probability of failure and is thus a strength material property [15, 17].

The scale parameter σ_0 has the peculiar unit of $MPa \cdot (meters)^{2/m}$ (or $MPa \cdot (meters)^{3/m}$ for volume flaws).

The integration of Eq.3.8 for a uniform stress in the uniaxially loaded test sample (gauge section of a tensile specimen) and the approaches of Eq.3.7 and Eq.3.9 are related by the equations

$$\sigma_{0A} = \sigma_\theta A_{eff}^{1/m} \text{ or } \sigma_{0V} = \sigma_\theta V_{eff}^{1/m} \tag{3.11}$$

Since σ_{0A} and m are material parameters, it is possible to predict the strength of a given specimen (#1), σ_1, having an area A_1 or volume V_1, knowing the strength of another specimen (#2), having an area A_2 or volume V_2, using the following equations,

$$\frac{\sigma_1}{\sigma_2} = \left(\frac{A_2}{A_1}\right)^{1/m} \text{ or } \frac{\sigma_1}{\sigma_2} = \left(\frac{V_2}{V_1}\right)^{1/m} \tag{3.12}$$

$$\sigma_\theta = \frac{\sigma_{0A}}{A_{eff}^{1/m}} \text{ or } \sigma_\theta = \frac{\sigma_{0V}}{V_{eff}^{1/m}} \tag{3.13}$$

where A_{eff} and V_{eff} are the effective volume and area of the component, respectively. The effective area or volume of a given component is defined to be equal to the area or volume of a tensile specimen, subjected to uniform axial tensile stress equal to the maximum effective stress in that component. In a complex structure, the effective stress depends on the multiaxial stress state, fracture criterion and flaw shape.

Failure of cracks subjected to mixed-mode loading is described in terms of failure criterion $g(K_I, K_{II}, K_{III})$ [13]. Failure occurs if the critical value of g is exceeded. The mixed-mode loading can be expressed in terms of an equivalent mode I stress intensity factor, defined as:

$$g(K_I, 0, 0) = g(K_I, K_{II}, K_{III}) \tag{3.14}$$

The failure criterion $g \geq g_c$ can be reformulated in terms of the mode I fracture toughness K_{Ic}:

$$K_{Ieq} \geq K_{Ic} \tag{3.15}$$

There are various failure criteria for cracks subjected to mixed-mode loading available in literature. Statistical calculations presented in this work have been based on the empirical criterion of Richard [18] implemented in the STAU program [13]. The criterion is based on a curve fit to a large set of data obtained with fracture mechanics specimens subjected to mixed-mode loading [13, 18].

The equivalent mode I stress intensity factor K_{Ieq} is given by [13]:

$$K_{Ieq} = \frac{1}{2} \left(K_I + \sqrt{K_I^2 + 4\alpha_1^2 K_{II}^2} \right) \tag{3.16}$$

The equivalent stress takes into account the effect of mixed mode loading on the behavior of a randomly oriented crack in a multiaxial stress field. This equivalent stress is calculated using a criterion for mixed-mode failure of the form given in Eq.3.17 [13].

$$\sigma_{eq} = \frac{1}{2} \left[\sigma_n + \sqrt{\sigma_n^2 + 4\tau_{II}^2 \alpha_1^2 \left(\frac{Y_{II}}{Y_I} \right)^2} \right] \tag{3.17}$$

A well established program to determine the failure probability of brittle components is the STAU (ger. STatistische AUswertung) program developed by the Research Center Karlsruhe in cooperation with industrial partners, including Robert Bosch GmbH. Based on a 3-D stress distribution and the known shape of the probability distribution, which is reflected through the Weibull modulus m, the effective volume or area can be calculated. The efficiency of application of statistic methods based on the weakest link theory in the strength prediction of

brittle materials will be presented on the example of polycrystalline silicon in the further chapters of the thesis.

3.3 Polysilicon - a basic material for MEMS industry

Due to polysilicon having similar mechanical properties to single crystal silicon, the ease of its deposition and structuring as well as its ability to modify the electrical properties by means of doping, polysilicon became a fundamental material of the semiconductor industry [19,20]. The surface micromachining method used for structuring of functional polysilicon layers as we know it today was first demonstrated by Howe and Muller in the early 1980s [21]. In the following chapters a compact introduction into the polysilicon deposition techniques, microstructure and its mechanical properties is given.

3.3.1 Deposition and microstructure of polycrystalline silicon

For most applications, polysilicon is deposited using gas phase decomposition of silane, in a low-pressure Chemical Vapor Deposition (LPCVD) furnace, at temperatures ranging from 580 to 650°C and pressures ranging from 25 to 150Pa, on wafers up to eight inches in diameter [22, 23, 24, 25, 26].

A general issue for the formation of thick films of polysilicon in classical LPCVD processes is the low deposition rate. Most of polysilicon micromachined structures are thus based on layer thicknesses of 2-5μm. The use of an epitaxial reactor, and for example SiH_2Cl_2 as a gas substrate, allows deposition of thicker layers of 10-20 μm within reasonable deposition times. The deposition rate in an epitaxial reactor at a temperature of 1000°C reaches 0.55 μm/min, which is approximately 30 times higher than typical values for LPCVD [27, 28].

Polysilicon is made up of small single-crystal domains (grains), whose orientations vary with respect to each other. The grains are separated by grain boundaries. The deposition at a temperature below 570°C results in amorphous layers. At higher temperatures the grain structure changes in a dramatic way. For example, at 600°C, the grains are very fine, while at 625°C the grains are larger and have a columnar structure aligned perpendicular to the plane of the substrate [1, 29, 30]. Detailed information concerning grain growth phenomena which occurs during film formation can be found in [31,32,33]. As with grain size, the crystalline orientation of the polysilicon grains is dependent on temperature. Polysilicon deposited at 600 to 650°C has a preferred 110 orientation. At higher temperatures, a 100 orientation dominates [1].

During the fabrication of micromechanical systems the deposited films undergo typically few high-temperature processing steps (doping, annealing, thermal oxidation) leading to recrystallization and change of the microstructure of the material [1, 34].

There is a big variety of parameters influencing the microstructure and thus the mechanical properties of the polycrystalline silicon [35, 36, 37, 38, 39]. While comparing characteristics of different polycrystalline materials from the literature, deposition and processing conditions should be taken into account.

3.4 Fracture toughness of polysilicon

The fracture toughness characterizes the material's resistance against crack propagation. The fracture toughness does not depend on the specimen's size [30]. The fracture toughness $K_{I,crit}$ of a brittle material can be calculated from:

$$K_{I,crit} = \sigma Y(a)\sqrt{\pi a} \qquad (3.18)$$

where a is a crack size, $Y(a)$ is a geometric function characterizing the shape and length of the crack, as well as the geometry of the specimen and the specific loading situation. $Y(a)$ can be derived using either analytical solutions or numerical simulations.

The determination of fracture toughness is usually based on appropriate fracture mechanics tests of samples containing a crack-like defect of a defined known length [40]. Bagdahn et al. performed both tensile and bending tests on pre-cracked polysilicon beams with notches created both indenter and FIB. Resulting cracks are presented in Fig. 3.5.

(a)

(b)
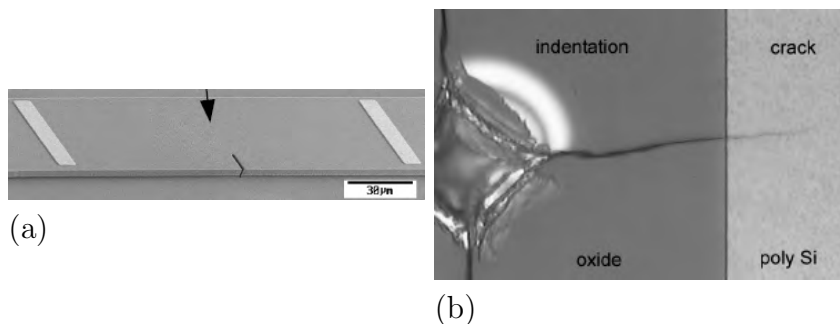
Figure 3.5: Pre-cracked specimens used for fracture toughness measurements by Bagdahn et al. [40]. a) FIB pre-cracked specimen, b) specimen pre-cracked with nanoindenter

The fracture toughness of the FIB notched bend specimens had an average value of 1.1 $MPa\sqrt{m}$. An average fracture toughness of 2.15 $MPa\sqrt{m}$ was calculated for focused ion beam specimens investigated in tensile testing. In contrast, the average fracture toughness of the pre-cracked samples was 0.86 $MPa\sqrt{m}$ [40]. Sharpe et al. [41] derived a value of 1.4 $MPa\sqrt{m}$ for tensile specimens with central notch. Kahn [42] reported values of 1.1 $MPa\sqrt{m}$ measured for notched electrostatically loaded specimens.

Known from the literature [43] values of K_{IC} are in the range from 0.75 to 4.5 $MPa\sqrt{m}$. The scatter in the fracture toughness values is presumably the function of the measurement technique and the crack-like defect creation method and resulting sharpness of the crack. These dependencies are supported by the results of Myers et al [44] who investigated the effect of notch radius on the fracture of single crystal silicon along the 111 plane. Reported fracture toughness varied from 1.24 to 2.85 $MPa\sqrt{m}$ for radii 80 to 580μm.

In this work the fracture toughness of polysilicon was accepted to be 0.85 $MPa\sqrt{m}$ [45].

3.5   Methods of thin film strength testing

The fracture strength, fracture toughness, Young's modulus, residual stress and Poisson ratio are the crucial mechanical parameters to be taken into account while designing reliable MEMS devices. The properties of thin films are strongly dependent on deposition and processing conditions and may be substantially different than those of the bulk material [46]. For several years, researchers worldwide have been trying to determine the mechanical properties of thin polysilicon films. The measurement of the mechanical properties consists of a few steps including:

- Fabrication and mounting of a specimen

- Measurement of specimen's dimensions

- Controlled application of the force or displacement

- Measurement of the force

- Measurement of the displacement, or preferably, strain.

However, ASTM standards define the procedures of material characterization. Their direct application in MEMS material testing is difficult due to the small dimensions of specimens. Numerous complications with the application of standard equipment in testing of tiny specimens resulted with development of novel miniaturized testing setups. In many cases the testing devices are integrated with test specimen and fabricated by common micromachining steps [47, 48].

Popular testing techniques such as tensile [49, 50, 51, 52, 53, 39, 54], beam-bending [55, 56, 57], membrane-bulge [58, 59, 60], and frequency-response testing [61, 62, 63, 64, 65] as well as nanoindendation techniques [66] are utilized in the characterization of mechanical properties of MEMS materials. In the following chapters a compact overview of testing methods is given and example results of the investigations are presented.

3.5.1   Tensile testing of polysilicon

Greek et al. [67] performed mechanical testing of epitaxial deposited polysilicon with a thickness of 10.5μm, with the use of tensile specimens consisting of a released beam with a ring, fixed at one side to the substrate. The testing unit, placed in the chamber of a Scanning Electron Microscope, consisted of a piezoelectric actuator and a force sensor connected to a cylindrical tungsten wire. Force was applied by a tungsten probe placed in the ring along the beam axis. The displacement value measured by a sensor consisted of the deflection of the measurement system and the desired strain of the sample. Young's modulus was calculated based on measurements of two structures with different lengths, under assumption that the elasticity of the testing setup is a constant for both measurements. Therefore there was no need to use special instruments or techniques to measure the strain of the specimen.

Chasiotis et al. [68,69] employed Atomic Force Microscopy (AFM) to obtain deformation records of thin polysilicon films. The AFM acquired local surface topographies of a specimen surface in a Non-Contact Mode. The investigations were conducted without any special equipment for strain measurements.
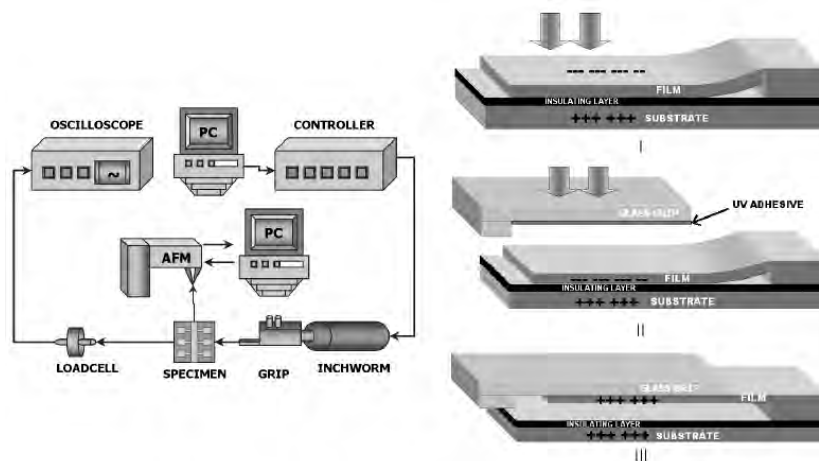
Figure 3.6: Left: schematic view of experimental setup; Right: Successive steps of film gripping, I - the film is forced electrostatically to lie flat on the substrate if it is bent due to residual stress gradient, II - the glass grip with a UV curable adhesive layer is moved towards the surface of the film, III - the same charge is induced in the substrate and the film to overcome any stiction forces by repelling the film from the substrate and forcing it to adhere to the UV adhesive under the grip [68]

The AFM data were analyzed by Digital Image Correlation (DIC) to derive local strain fields with spatial resolution on the order of nanometers. Tensile specimens were 'dog-bone' shaped with a large paddle for convenient UV adhesive gripping (Fig. 3.6). The experimental apparatus employed an inchworm actuator to impose displacement on the specimens with resolution of 4nm and a miniature tension-compression load cell with 10^{-4} accuracy. In addition to the in-plane

properties, the relative out-of-plane surface properties can be obtained via phase imagining AFM.

Figure 3.7: Schematic drawing of tensile testing using electrostatic force grip [70]

Tensile testing reported by Tsuchiya et al. [70] was based on electrostatic gripping technique presented in the Fig. 3.7. The tester constructed in a Scanning Electron Microscope was equipped 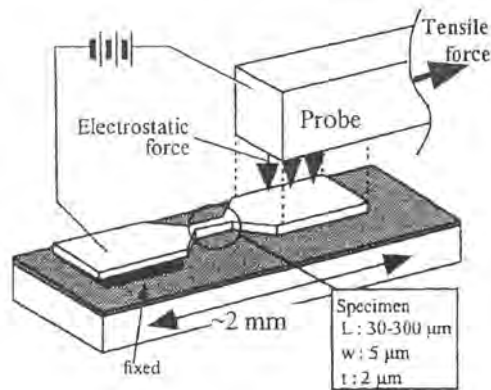with a load cell for force measurement and a piezoelectric actuator. A specimen can be easily fixed or released from the tester grip by applying or cutting off the electrical power supply. The voltage applied between the specimens and the probe to fix the sample during tensile testing was 150-200V. The described method can be only used for conducting materials. Insulating materials e.g. SiO_2 can be fixed by arranging two electrodes on a probe or by making an electrode on the free end of the specimen [49]. A large number of specimens needed to perform statistical evaluation could be tested without any demanding sample preparation.

Sharpe et al. [53,71,72] tested polysilicon specimens of different planar dimensions and thicknesses of 2.5 and 3.5μm. The die with the polysilicon specimens was glued to a five-axis stage controlled by piezoelectric motors, used to align the specimen with the electrostatic gripper introduced by Tsuchiya as described above. The load cell was mounted on a single-axis picomotor stage used to pull the specimen. The major innovation was strain measurement with the use of laser-based interferometry, from two gold lines deposited onto the central portion of the specimen [73]. The set-up for interferometric measurements is shown in Fig. 3.8. The movement of the interference fringes as the specimen is strained is monitored with photodiode arrays controlled by a computer to enable real time, high resolution strain measurements.

Using a similar method, Yi and Kim [74] measured Young's modulus and the fracture strength of single-crystal-silicon. The direct tension testing can be used for determination of Young's modulus, Poisson's ratio and fracture strength testing, in a most direct manner. The described methods are very effective. The requirements for sample alignment and deflection measurement are very stringent
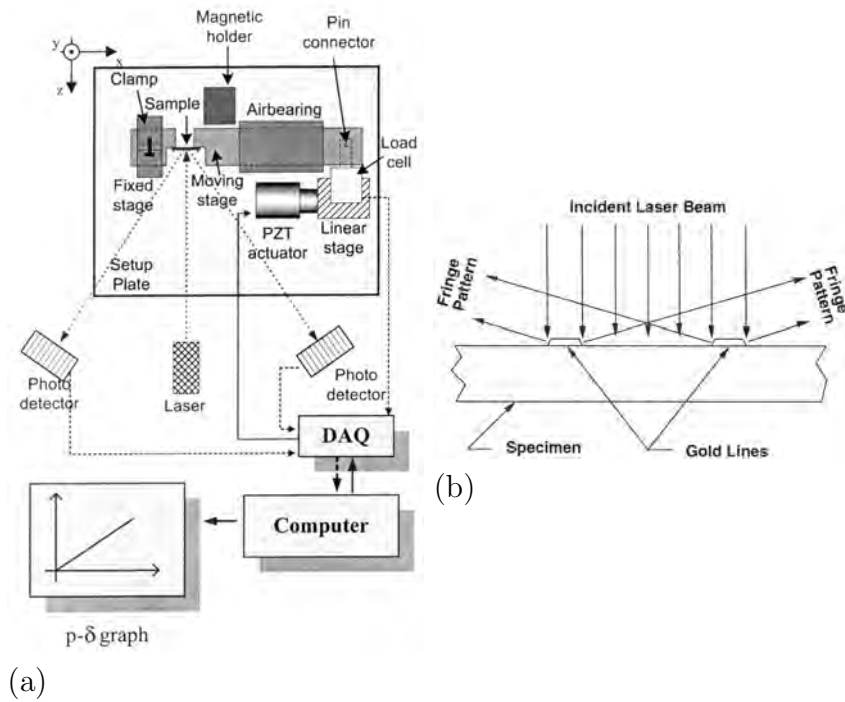
Figure 3.8: a) schematic view of testing setup based on interferometric tension measurement principle [74], b) schematic of the interferometric strain/displacement gage [75]

in the case of direct tension testing [76]. When the measurements are performed properly, the data can be easily interpreted.

3.5.2 Beam-bending testing of polysilicon

The testing procedure based on beam-bending has already been used in 1957 by Pearson to determine the mechanical properties of silicon wickers [77]. Since this time the method became a standard in the investigations of mechanical properties of MEMS materials.

The interesting idea of polysilicon fracture strength testing with the use of a thermal actuator, was presented by Kapels et al. [78]. The thermal actuator consists of two narrow beams with a thickness of 4μm, which expand due to electrical heating during the test, and a cold plate to which a short fracture beam is attached. The mechanical deflection is measured with the use of nonius with a resolution of 5nm. Using different types of beams, authors could compare the fracture strengths measured under uniaxial tension and bending load. To investigate fracture in the tension and bending case, authors used 5μm long and 0.7μm wide fracture beams for uniaxial loading and 4μm long and 2.5μm wide beams rotated by 90° for bending test.

Ding et al. [79] applied the nanoindenter to apply the load during the beam-bending test of 2.4μm thick LPCVD polysilicon. The method was based on mea-

surements of deflection of an end-loaded, free-standing, cantilever, until the fracture occurred. The system had load resolution of 10μN and depth displacement of 1nm. During testing, the micro-beams were deflected at a constant velocity.

In order to achieve a very high load resolution with nanometric precision in the measurements of cantilever deflection, many researchers conducted their investigations with the Atomic Force Microscope in a contact mode. Sundararajan et al. investigated the bending strength of single crystal silicon (001) beams with average thickness of 255nm [80]. The testing setup based on Atomic Force Microscopy is presented in the Fig. 3.9. The three-sided pyramidal diamond tip mounted on a rectangular stainless steel cantilever was used for the bending tests. The vertical deflection of the tip was measured with the use of a laser and a photodiode array.
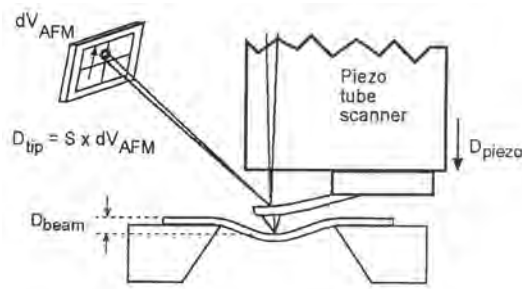

Figure 3.9: Schematic of nanobeam bending experiment using AFM [80]

The sensitivity of the cantilever was calibrated prior to the bending test [81, 80]. Tensile testing reported by Tsuchiya et al. [70] was based on the electrostatic gripping technique presented in the Fig. 3.9.

The investigations of Namazu were conducted on single crystal silicon [82] using an Atomic Force Microscope. Authors tested 255nm thick silicon beams with a width ranging from 200 to 800nm fabricated on Si diaphragm by means of field-enhanced anodization using AFM and anisotropic wet etching. Bending tests, for micro- and millimeter scale beams fabricated by a photolithography technique were carried out using an ultra-precision hardness and scratch tester.

The mechanical properties of 15μm thick epitaxial polysilicon were also investigated by Carli at al. [83]. A comb-finger type micro-motor was used as a source of mechanical load. For determination of fracture strength, two cantilever beams with variable cross-section were used. The first girder was designed with a sharp notch placed in the area of highest bending moment (Model R1 Fig. 3.10). The second cantilever was designed using a large constant radius of curvature for the notch (Model R2 Fig. 3.10). Both beams maintained a very small inertia, in a restricted length, allowing high bending stresses with reduced displacement requirements at failure. The experimental procedure of evaluation of failures stress was based on the measurements of the displacement and the calculation of the applied force for the measured voltage values at rupture of the specimen. The

FE method was used in estimation of peak stress value at failure when the corresponding force value was an input for the simulations.
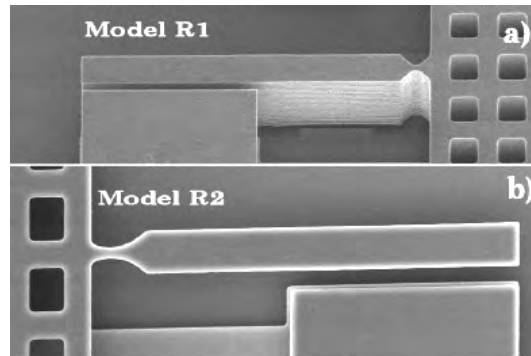

Figure 3.10: Test structures for ultimate stress evaluation, a - Model R1 - sharp notch, b - Model R2 large and smooth notch [83]

Another example of electrostatic actuator application for bend testing of polysilicon was presented by De Masi et al. [84,52]. These authors developed two types of on-chip tests to evaluate the elastic Young's modulus and the fracture strength of 15μm thick epitaxial polysilicon. A pure tension test and a single-edge-notched tension test were performed using an electro statically actuated device that consisted of parallel plate capacitors. The set of 287 elementary cells generated a maximal force of 14mN [51].

Cacchione [85] performed out-of-plane bending experiments with the use of an integrated actuator, based on electrostatic attraction forces, in order to measure the fracture strength of 0.9μm thick polycrystalline silicon.

Beam bending testing has the advantage of being simple compared with the direct tension test. The force applied during the test is smaller than in the case of direct tension tests and the resulting mechanical deflection of the specimen is large enough to be measured using optical microscopy. The bending test is free of the difficult problems of sample gripping and the results of the test are not affected by slight misalignments in the loading direction [76].

3.6   Fracture strength and size effect in polysilicon

Greek et al. [67] conducted tensile testing on epitaxial polysilicon films with a thickness of 10.5μm, fabricated in different doping and annealing conditions. The test beams were 250μm and 1000μm long. The mean values of Young's modulus were in the range 160 - 167GPa with estimated error of approximately 3%. Results of fracture strength testing were analysed with the use of a Weibull distribution. Mean fracture strength was in the range 1.08-1.25 GPa, while the Weibull modulus 'm' was in the range 6.1-11.7.

The 'dog-bone' type of specimens fabricated from 2μm thick polysilicon was used by Chasiotis et al. [68, 69] for tensile testing. The gage section was 400μm long and 50μm width. The average Young's modulus value of 160 GPa [69] was obtained from strain computed with Digital Image Correlation of AFM test recordings. The measured value of fracture strength was 1.00 ± 0.1GPa. In addition, the AFM data have shown an influence of the grain structure on the character of crack propagation. Authors observed a preference for intergranular fracture, while other researchers have reported transgranular fracture of polysilicon [86]. Authors concluded that observations probably represent an effect of the etching process on the grain boundary strength.

The same method was applied by Knauss et al. [87] to investigate the existence of size effect in the measurement of mechanical strength for micron sized geometries. The 'dog-bone' specimens were fabricated with elliptic perforations, so that the aspect ratio and notch radii led to constant stress concentrations under varying notch radii. The radius of curvature varied between 1 and 8μm. The gage section of the free-standing beam varied from 250x30x3 to 700x340x2μm (length x width x thickness). The stress concentrations varied from K=3 for specimens with circular holes, to K=11 for specimens witch elliptical notches of high aspect ratio. Tensile strength of the specimens in the absence of any notches and of stress concentrations was measured to be about 0.85GPa. However, for smaller radii of curvature it is clearly seen that the values of the local strength systematically increase up to 1.8GPa with decrease in the radius of curvature.

The 5μm wide and 30, 100 and 300μm long LPCVD polysilicon specimens with thickness of 2μm have been tested by Tsuchiya et al. [70]. The mean values of tensile strength were 2.0-2.6GPa, and tensile strength decreased with increasing specimen length. The mean strength of the 30μm long specimens was about 30% higher than that of 300μm long specimens. The scatter of measured values also decreased with increasing length of the specimens. The measured mean tensile strength is 6-8% of the theoretical strength of single crystal silicon [88]. The size of the flaw calculated using Griffith's equation was 28-47μm. Based on the experimental results Tsuchiya et al. concluded that flaws such as surface roughness should be considered as the initiation of polysilicon film fracture.

In other work Tsuchiya [89] tested 2μm and 5μm width specimens with length of 30, 100 and 300μm. More than twenty specimens of each size were tested in air and vacuum, respectively. The fracture strength measured in vacuum was higher than in air. The size effect with regard to length was observable but not to width. Using the Weibull statistics, the fracture origin was predicted to be located at either the side surface or on the edge of the specimen. This was confirmed by SEM fracture analysis [50].

Ding et al. [90] investigated the fracture strength of 2.4μm thick LPCVD polysilicon in bending. Authors have shown that the strength of specimen's decreased with increasing effective volume and surface area, but increased with in-

creasing in surface-to-volume ratio. The size of critical flaws was calculated to be 58-117nm, which was in the same order of magnitude as surface roughness and slightly smaller than the grain size of the material tested.

The measurements of fracture strength on 255nm thick single crystal silicon by Sundararajan et al. [80] resulted in fracture strength of 19.2GPa. Previously reported values of fracture strength measured with the use of micrometer-sized specimens were in the range from 1 to 6GPa [80]. Authors concluded that strength of brittle materials shows a specimen size dependence. Crack length, of 1-3nm, computed from the Griffith's equation was similar to the maximum peak-to-valley values measured with AFM. Authors suggested that the surface roughness of the specimen affects the bending strength of the beams.

Namazu et al. [82] reported that the values of Young's modulus are independent from the dimensions of specimens. The average bending strength for the 200nm wide nanometer scale beam was 17.53 GPa, which is 2.3-4.7 times larger than the bending strength on the micrometer scale and 38 times larger than that on the millimeter scale. The specimen size also affected the shape parameter m which increases with a reduction of the specimen size.

Sharpe et al. [53,71,72] tested polysilicon tensile specimens with widths from 2 to 50μm and lengths from 50 to 500μm and thickness of the material ranged from 2.5 and 3.5μm. The strength measured on the smaller specimens averaged 1.45±0.19MPa in contrast to 1.20±0.15MPa of the wider specimens. The round-robin [91] reported higher strengths in bending for the same material, 2.7±0.2 by Brown and 2.8±0.5GPa by Johnson.

In the investigations of Kapels et al. with the use of a thermal actuator [78] the fracture strength for polysilicon under uniaxial load was found to be 2.9±0.5MPa, in the beam-bending test the measured fracture strength was 17% higher.

Bagdahn et al. [92] have conducted a series of tensile strength tests on 3.5μm thick polysilicon specimens with a central hole, and with symmetric double notches and width of 20 and 50μm. The measurement setup by Sharpe [53] was applied. Bagdahn summarized results of his investigations and literature research in the form of plot presented in Fig. 3.11 showing clearly the trend toward decreasing fracture strength with increasing specimen size [93].

The literature research clearly shows a size effect in polysilicon. In most of cases the investigations show that defects presented on the surface are with high probability the weakest-point and lead to fracture. Application of the Weibull theory and statistical methods taking into account a size effect, can support the analysis of experimental results and help to compare measurement results i.e. of tensile and bending tests for the same material. Statistic methods can be also applied to estimate the material constants σ_{0A} and σ_{0V} and based on that to predict the fracture strength/fracture probability of other structures in a defined loading situation.
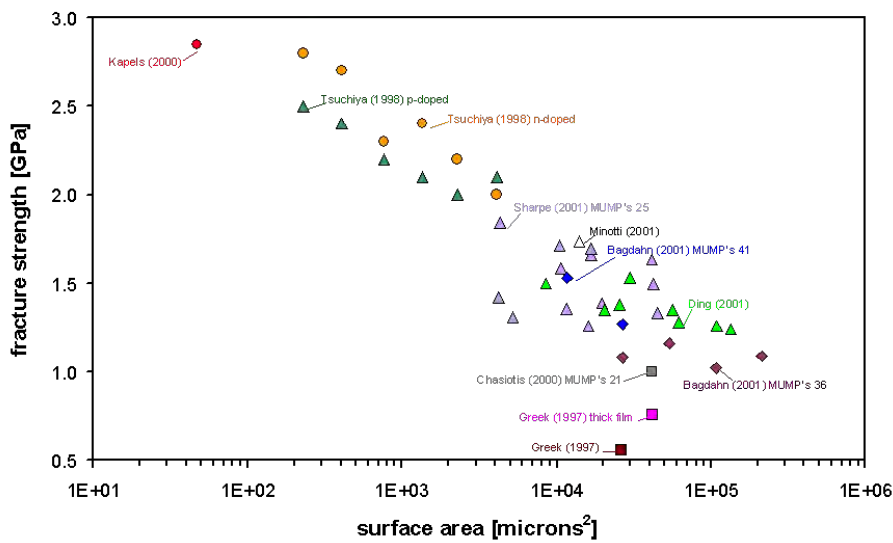
Figure 3.11: Tensile strength versus total surface area [93]

3.7 Fatigue testing of polysilicon

Static or quasi-static loading is rarely observed in MEMS engineering practice, making it essential for the designer to address the implications of repeated loads. Fatigue may be characterized as a progressive failure phenomenon that proceeds by the initiation and propagation of cracks to an unstable size. The first fatigue investigations were already being conducted during the first half of the nineteenth century. In 1829 Albert performed the first probable fatigue study of iron chain. In 1860 Woehler conducted systematic investigations of fatigue failure in railroad axles for the German Railway Industry. He observed that the strength of the steel axles subjected to cyclic loads was much lower than the static strength. His work led to the characterization of fatigue behavior using stress amplitude-life (S-N) curves and the concept of the fatigue endurance limit [94].

Fatigue of silicon was first demonstrated in 1992 by Connally and Brown [95]. Polysilicon as an ideally brittle material at room temperature was not expected to be susceptible to dynamic fatigue. This surprising discovery gave the beginning of many intensive investigations. The following chapter gives a brief summary of investigation methods and their results.

3.7.1 Loading techniques

The selection of the testing method is a very important part of the planning phase of every experiment. One has to take into account the demanded forces, deflections as well as the testing frequency, which is the major parameter influencing the testing time and therefore cost. A variety of different technical solutions can be used in fatigue investigations.
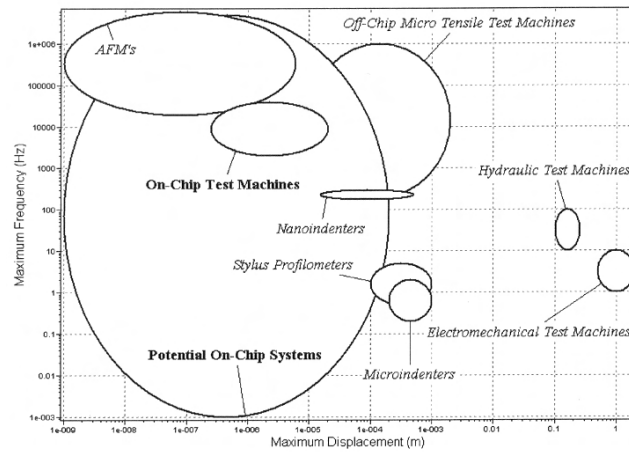
25

Figure 3.12: Comparison of different loading techniques used in micromechanical testing [96]

The testing frequency varies from thousandths parts of Hz up to MHz and the mechanical displacement introduced by the actuator, scales by nine orders of magnitude. All loading techniques can be divided into two general groups, external and integrated loading. Spearing [96] compared a variety of different techniques available in Fig. 3.12.

Minoshima et al. [97] applied a nanoindenter in fatigue investigations. The free-standing microcantilever beams, fabricated from single crystal silicon, were tested by pushing downwards in laboratory air and water. The testing frequency was 0.1Hz and a stress ratio of 0.1. Similar fatigue investigations can be performed on membranes or beams arranged in a three-point bending testing.

Bagdahn and Sharpe [98,40,99] worked with the tensile specimen as presented in Fig. 3.13. Tests were carried out with frequencies of 50, 200, and 1000Hz with either a piezoelectric actuator or a small loudspeaker. The testing frequency of 6000Hz was achieved with a small loudspeaker oscillating with its resonant frequency.
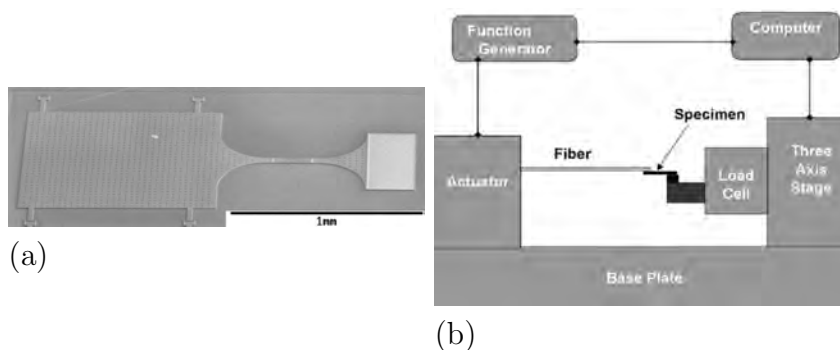

(a)

(b)

Figure 3.13: a) SEM photograph of polysilicon tensile specimen, b) schematic of tension-tension fatigue setup [98]

Tsuchiya tested the fatigue of silicon on a piezoelectric shaker. Vibrations of the shaker were transmitted onto the beams oscillating with high amplitudes in their resonant frequency [100].

Many examples for application of integrated actuators can be found in literature. The silicon test specimens can be easily integrated with microactuators by fabricating in the same steps of micromachining technology. In most of cases the actuation is based on electrostatic forces induced between comb or parallel plate electrodes.
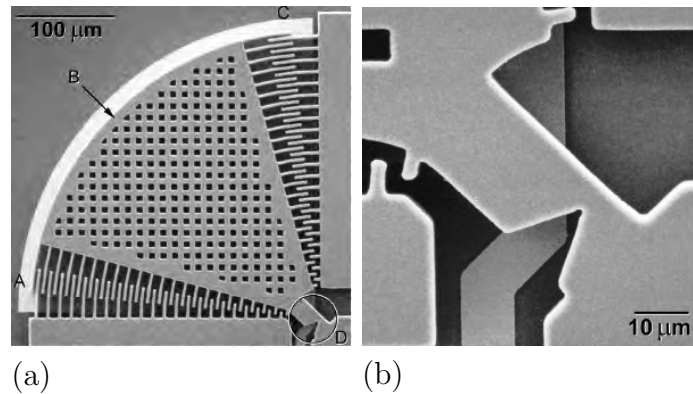

(a)   (b)

Figure 3.14: Scanning electron micrographs of the stress-life fatigue characterization structure. The electrostatic comb drive actuator (A), resonant mass (B), capacitive displacement transducer comb (C), and notched cantilever beam specimen (D) are shown in an overview on the left. A detail of the notched beam is shown on the right [101]

A very known example is the fan-shaped electrostatically actuated test structure presented by Muhlstein and Brown - Fig. 3.14 [101]. The notched beam designed for testing at resonant frequency of approximately 40kHz was approximately 40μm long, 19.5μm wide and 2μm thick. Van Arsdell used specimens of similar geometry with different planar dimensions and resonant frequency of approximately 50kHz [102, 103]. The stress ratio was -1. The control of the specimen's amplitude in the function of the applied voltage (calibration) has been done using the microvision system developed by Freeman and presented in Fig. 3.15 [104].

A similar oscillator was also fabricated in single-crystal silicon [9] (Fig. 3.16).

Kahn et al. [105] studied fatigue behavior of polysilicon with the use of an on-chip electrostatically driven actuator presented in Fig. 3.17. Two different devices were fabricated from doped silicon, containing either 1456 or 2040 pairs of comb fingers, which pull the actuator to the left when the voltage is applied. Specimens were fabricated from 5.2μm thick LPCVD polysilicon film. The devices were also fabricated from undoped silicon. In order to achieve sufficient conductivity, allowing electrostatic actuation, the devices were sputter-coated with approximately 10nm of palladium. The presented design varies from the oscillator presented by Muhlstein, in the option to conduct the investigations with various
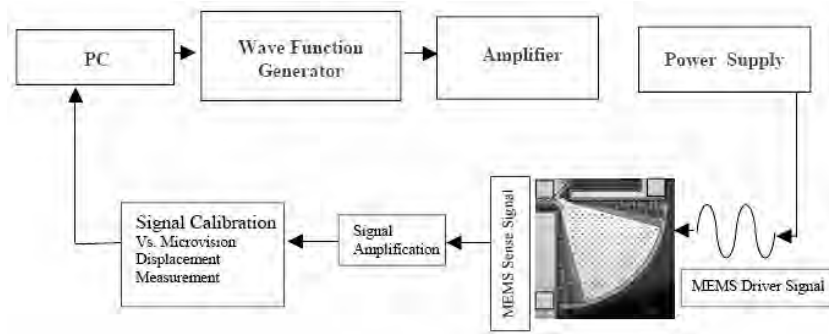
Figure 3.15: Schematic of microelectronic circuits for the control of the MEMS [104]
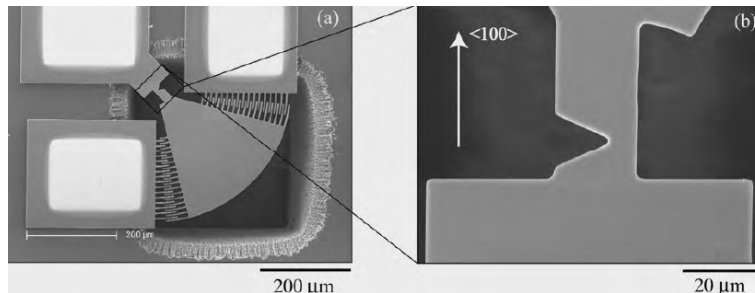
Figure 3.16: SEM images of the micron-scale fatigue characterization structure (thickness: 10μm) and the notched cantilever-beam specimen (inset) [9]

ratios of compressive to tensile stress. The resonant frequency was approximately 20kHz.
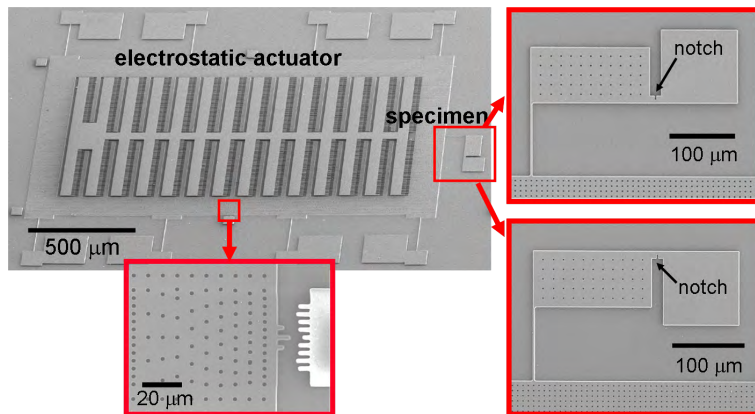
Figure 3.17: Scanning electron microscopy (SEM) images of a micromachined device for measuring bend strength and fatigue resistance, left - the electrostatic actuator integrated with the fracture mechanics specimen, right - higher magnification rotated images of two single edge-notched fatigue specimens that can be integrated with the actuator, the bottom inset shows the notch area after testing, bottom - higher magnification rotated image of the measurement scale [3]

Kapels et al. [78] used in their fatigue investigation of polysilicon fatigue,

a novel thermal actuator that permitted monotonic and tension-tension loading presented in Fig. 3.18. By cycling electric heating of the arms, the actuator pulls the test specimen in tension-tension with a frequency of 1Hz.
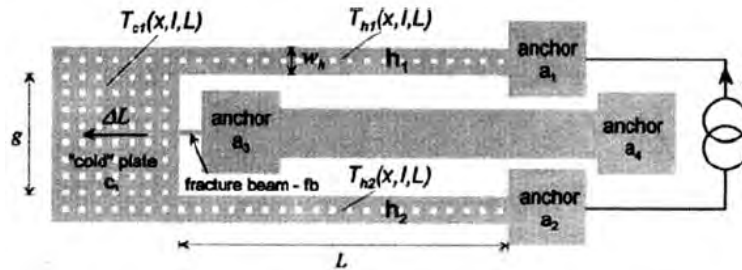
Figure 3.18: Schematic of the Kapels et al. device [78]

The general advantage of loading techniques based on the principle of mechanic, without the use of electric current is the possibility to conduct the investigations in a different atmosphere (also corrosive) or even directly in water. The major drawback of the mentioned systems is the problem of alignment and low testing frequency. Also parallel testing is very difficult due to the cost of multiple setups of equipment, needed laboratory space and personal handling. The charm of specimens driven with the forces of electrostatics is the potential of using high testing frequency, the lack of alignment problems and the possibility of parallel testing, like that described in Chapter 4 of this thesis. The development of reliable supporting electronics demands experience in working with low power electrical signals.

3.8 Fatigue behaviour of polysilicon

Van Arsdell et al. [102] developed an experimental protocol for studying slow crack growth in LPCVD polysilicon, based on the frequency change of a notched rotational oscillator and nonlinear dynamics. The notch in the 2μm thick specimens was introduced with a nanoindenter. The electrostatic forces were used for actuation with the resonant frequency of 45-50 kHz. The resonant frequency of a pre-cracked specimen, driven over a period of 20 hours, decreased by 1400 Hz. The frequency of the uncracked specimen driven in the same conditions was stable to within $\pm$ 2Hz. Experiments conducted in damp air (50%, 70% relative humidity) demonstrated that polysilicon MEMS are susceptible to subcritical crack growth. No clear relationship between crack growth rates and stress intensity was observed. Authors claimed that a subcritical crack growth is due to a stress corrosion cracking mechanism, involving the native oxide film, rather than the polysilicon itself.

Muhlstein et al. [106, 101, 107, 45] used a polysilicon fatigue characterization structure originally developed by Van Arsdell [102] presented in Fig. 3.14. The

specimens were excited at the resonant frequency at a defined excitation voltage for a period of time. The extensive FE and numerical modeling by Muhlstein et al. helps to understand the changes in the dynamic response of the device, due to accumulation of oxides, debris, and moisture and crack growth [106]. The experiments were conducted under controlled environmental conditions: 50, 75% relative humidity, in laboratory air, and in a vacuum ($2 \cdot 10^{-7}$ mbar). Authors observed that polysilicon undergoes faster degradation in the presence of moisture compared to in dry laboratory air. The model suggested that for specimens driven in air for approximately 1nm of crack extension, a 1Hz change in natural frequency should be observed [101]. The investigations with use of high-voltage transmission electron microscopy (HVTEM) revealed thickening of the oxide layer of up to 150 nm for specimens fatigued in air (Fig. 3.19) [108, 107, 109].
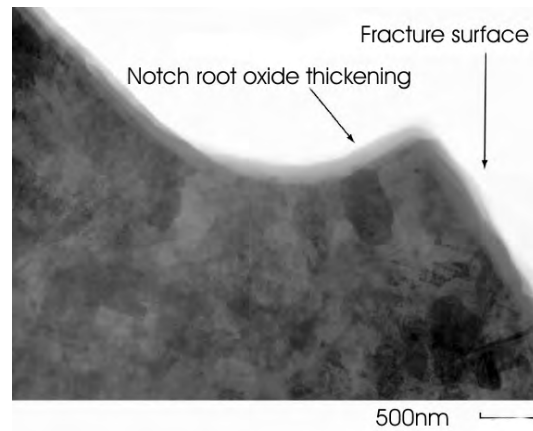
Figure 3.19: HVTEM image of the notch region in an unthinned polycrystalline silicon test sample, showing enhanced oxidation at the notch root, that failed after $3.56 \cdot 10^9$ cycles at stress of 2.26GPa [107]

Fatigue cracks are believed to initiate in silicon, during the local oxidation and stress corrosion cracking of the native SiO_2 layer. In order to verify the proposed theory Muhlstein et al. deposited an alkene-based monolayer on the surface of test specimens before the native oxide was formed. Although the deposition caused degradation of fracture strength of specimens, the experiments on protected polysilicon specimens confirmed that lifetimes were not affected by the applied cyclic stress [110]. Specimens tested in a vacuum did not fail even at high stresses, after cycling in excess of $10^9 - 10^{10}$ cycles.

The thickness of oxide layers, observed by Alsem et al. [108] on the surface of vacuum tested films, ranged from 15 to 30nm. They were not thick enough to accommodate the critical crack size to cause the failure of the entire structure [111].

Authors also investigated the fatigue behavior of 20μm thick, p-type (110), single-crystal silicon structures with similar geometry [112]. The silicon cantilever beams exhibited a time-delayed failure under fully-reversed, cyclic stress in room

temperature air with 50% relative humidity. The specimens were driven with constant amplitudes ranging from 4-10GPa for 1-5min and the resonant frequency was recharacterized. The resonant frequency of the specimen was observed to decrease monotonically, before the specimen failed at the notch. It was observed that single crystal silicon films can fail at stresses as low as one-half of their fracture strength when such stresses are applied cyclically, in a moist environment, for in excess of 10^{10} cycles. Although this trend has not been previously observed in case of any bulk brittle material [112].

Similar in the case of investigations on polysilicon, authors claimed that failure of thin films occurs by stable propagation of cracks due to susceptibility of silicon-based oxides to stress corrosion cracking. A 'reaction layer' fatigue mechanism, consisting of three steps [109] has been proposed (Fig. 3.20):

- Growth of initial post-release oxide layer under mechanical stress during cyclic loading

- Moisture assisted cracking of the oxide layer, resulting with stable crack growth

- Provided that oxide layer is thick enough, the catastrophic failure occurs when the crack size reaches the critical size
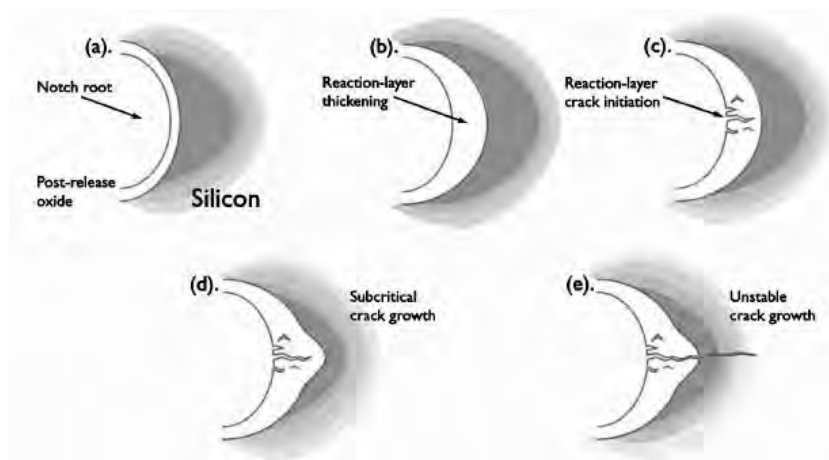
Figure 3.20: a) Schematic of the 'reaction-layer' fatigue mechanism at the notch of the polycrystalline silicon cantilever beam, b)localized oxide thickening at the notch root, c) environmentally assisted crack initiation in the native oxide at the notch root, d) additional thickening and cracking of reaction layer, e) unstable crack growth in the silicon film [108]

Allameh et al. conducted an experimental study of surface topology evolution during cyclic actuation of polysilicon MEMS structures [104, 113, 114]. The Atomic Force Microscopy was used to reveal local changes in grain morphology

and orientation on the semiconductor surface. The test specimen used was based on original design by Van Arsdell [115].

Specimens were actuated with voltages of 100, 110, 120, 130, 135, 140, 142.5, 145V, each for one hour except for the last actuation voltage that led to the failure of the sample after about 30min. Specimens were examined with AFM before actuation, after 5 minutes into the actuation and at the end of actuation for each loading step. The results of the study have shown that the surface of the polysilicon undergoes discernible changes under such loading conditions. The analysis of AFM profiles revealed that the surface features on the polysilicon sample elongate in the direction of the applied load.
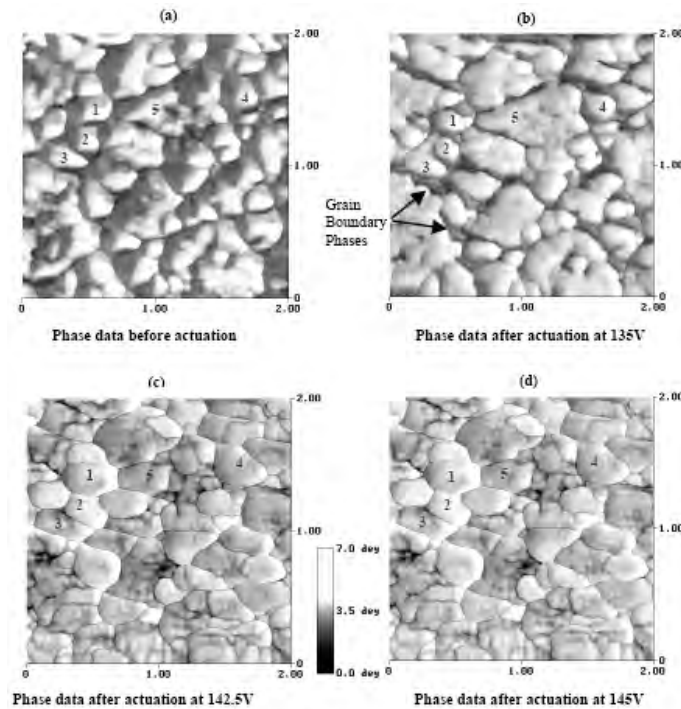
Figure 3.21: Phase-data-based AFM images showing surface evolution of the silicon MEMS sample under cyclic loading conditions. a) Before actuation and after actuation up to b) 135V, c) 142.5V and d) 145V [104]

The AFM examinations have shown the presence of some grain boundary phases, at the intermediate stages of actuation visible in Fig. 3.21b, Fig. 3.21c and Fig. 3.21d. They show clean boundaries after actuation with high voltages. A surface smoothing effect was observed especially at higher actuation voltages. The roughness of the specimen driven for $1.03 \cdot 10^{10}$ cycles with amplitude of 145V dropped down as much as of 30% of the initial RMS value and continued to drop until the specimen failed. It is hypothesized that crack nucleation occurred as a result of surface topology evolution in the SiO_2 surface layer.

In other work, Allameh et al. [113] investigated the evolution of the surface topology in notched polysilicon MEMS structure, under cyclic actuation at a

Figure 3.22: Schematic illustration of crack nucleation arising from possible stress-assisted dissolution of water [104]

relative humidity of 70%.

The AFM roughness investigation demonstrated the effect of stress on the evolution of the surface topology under cyclic loading. The topology evolution in the region of highest tensile stress, is thought to be associated with the roughening of the $S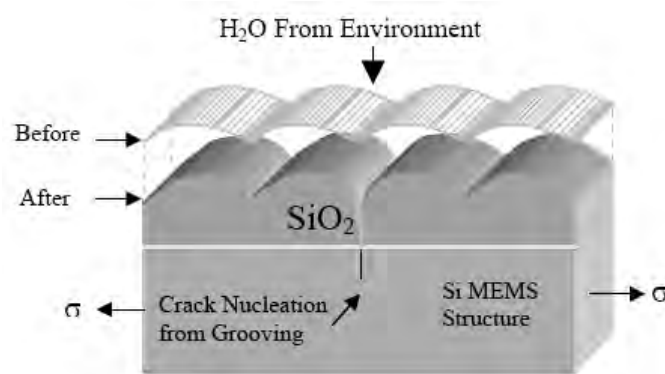iO_2$ films that is present on the polysilicon surface. Authors are of the opinion that the initially 2-10nm thick oxide layer might thicken due to autocatalytic oxidation, that could occur as a result of the re-oxidation of exposed fresh surfaces that are created due to fatigue damage and interactions with water molecules (Fig. 3.22). The results of investigations by Allameh et al. [114] show that the initial stages of fatigue are associated with stress-assisted surface topography evolution and the thickening of the SiO_2 layer present on the specimen surface.

The fatigue investigations by Bagdahn and Sharpe [98, 40, 99] have shown that the testing frequency does not influence the fatigue process. Morphology investigations using an AFM of cyclic loaded tensile specimens, revealed that the roughness in the neighborhood of fracture was higher than the roughness in the area that was exposed to a low stress. Authors reported a decrease of a mean tensile strength of about 1.10GPa to 0.75GPa after as many as 10^8 cycles in laboratory air. The results are consistent with previously mentioned results of Muhlstein and Allameh.

Kapels et al. [78] used in their fatigue investigation of polysilicon fatigue, a thermal actuator that permitted monotonic and tension-tension loading. In long term measurements with the frequency of 1Hz, authors observed a decrease in fracture strength of approximately 25% over 10^6 cycles. No fatigue mechanism has been discussed.

The research group from the Case Western Reserve University suggested that fatigue behavior is mostly influenced by the ratio of compressive to tensile stresses experienced during each cycle and that corrosive atmosphere can only accelerate the process in these conditions. Kahn et al. [105] studied fatigue behavior of

polysilicon with the use of the on-chip electrostatically driven actuator presented in Fig. 3.17. The movement of the actuator results in deflection of the test beam and a stress concentration at the notch of the specimen. Specimens were fabricated from 5.2μm thick boron doped LPCVD polysilicon film.

The fracture test was conducted by applying a DC voltage between the fixed and movable set of comb electrodes. The fracture strength was measured by increasing the DC voltage and optically measuring of the mechanical deflection with an accuracy $\pm 0.3\mu$m. The stress distribution in the specimen was modeled with the use of Finite Element Method. Similar devices of slightly different dimensions were also fabricated from non-doped polysilicon. To achieve sufficient conductivity to allow electrostatic actuation, the devices were sputter-coated with approximately 10nm of palladium. The electrostatic force was not sufficient to cause the fracture of non-doped specimens. The fracture strength was in this case measured by mechanically pushing the actuator with a probe.

To investigate the effect of humidity on fatigue behavior, resonance tests were performed in laboratory air and in a vacuum chamber, which was evacuated to a pressure of 8Pa. Authors observed that fatigue crack initiation and growth occurred in both environments, but the process was faster in air. In the vacuum, stress corrosion at the crack tip is expected to be less severe, but mechanical damage can occur during tensile-compression fatigue cycles [105]. The fracture surface revealed that the lower fatigue strength was accompanied by an increase in the size of the fracture-initiating flaw, which was interpreted as evidence of subcritical crack growth during cycling [116].

The XPS depth profiling confirmed that the surface of polysilicon test specimens of Kahn was covered with a native oxide with a thickness on the order of 2nm [117]. Authors examined the influence of the formation of thick surface layers by high temperature oxidation on fatigue behavior of polysilicon. Ten single-edge notched beam (Fig. 3.17) devices were loaded at 90% of the monotonic strength, by application of DC voltage and then mechanically blocked in this position. After 3000 hours storage in atmosphere of 90% relative humidity, none of the specimens failed. The results confirmed the absence of static fatigue in polysilicon specimens with thin native oxides [117]. Similar experiments carried out with specimens with thermally grown oxide, with thicknesses ranging from 45 to 140nm, indicated that a thermally grown thick surface oxide undergoes static fatigue [118].

Kahn et al. reported that the severity of the fatigue damage is strongly affected by the compressive stresses during fatigue loading [4]. Authors tested specimens by cyclic loading at a given mean stress, $\sigma_m = -2.2$GPa, and mechanic amplitude for 10 minutes (equivalent to approximately $6 \cdot 10^6$ cycles), the cyclic loading was then stopped, and the fracture static strength was measured [119]. This cyclic loading with small amplitude did not affect the bending strength, but cycling with large amplitude led to a decrease in bending strength (Fig. 3.23).

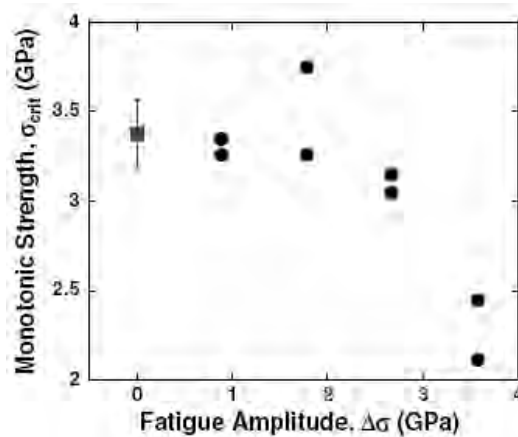Kahn et al. also conducted experiments with constant mechanical amplitude

Figure 3.23: Results from cyclic loading tests of undoped polysilicon. For all tests, the σ_m was -2.2 GPa. The monotonic bend strength is shown as the solid square with error bars equal to one standard deviation [119]

($\Delta\sigma$)of 2.0GPa and variable mean stress (Fig. 3.24a). Loading with small tensile or compressive mean stress did not affect the bend strength of the specimens. It was noted that in the experiments with the highest tensile mean stress (σ_m) of 2.0GPa, the maximum tensile stress at the notch during cycling exceeded the fracture strength of the specimen. It is believed that results indicate the existence of strengthening mechanisms in polycrystalline silicon. Summary of fatigue investigations by Kahn et al. is presented in Fig. 3.25.

(a)   (b)
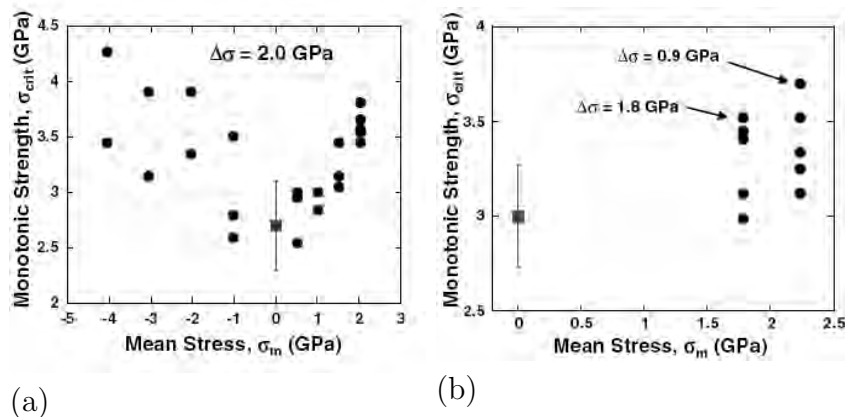
Figure 3.24: Results from cyclic loading, in each plot the monotonic strength is shown as the solid square. a) data for undoped polysilicon, $\Delta\sigma = 2.0$GPa, b) data for B-doped polysilicon, $\Delta\sigma = 1.8$GPa for specimens with $\sigma_m = 1.8$GPa and $\Delta\sigma = 0.9$GPa for specimens with $\sigma_m = 2.2$GPa [3]

Kahn et al. generally disagreed with the conclusions of Muhlstein at al. and in their work discussed three possible mechanisms that could control observed behavior - weakening and strengthening of polysilicon: microcracking, dislocation

Figure 3.25: The quantitative effect of $\Delta\sigma$ and σ_m on monotonic strength σ_{crit} [3]

activity and grain boundary plasticity [3].

There is no common, well accepted theory of polysilicon fatigue. Various researchers presenting their new results consequently support the ideas of 'stress corrosion cracking' or on contrary state that mechanical stresses rather then environmental interactions are the principle origin of polysilicon fatigue. The detailed discussion of postulated fatigue mechanisms as well as their consistency with measurement results achieved in this work will be the subject of detailed discussions in the last chapters of the thesis.

4

Experimental

4.1 Investigation on fracture strength

In order to investigate the dependency of the strength properties of polycrystalline silicon on a specimen's shape, size and type of loading, in the presence of the stress concentrations, the variety of bending and tensile specimens have been developed. The influences of side-surface quality as well as the film thickness on the strength of the material were the focus of the research. The following chapter describes measurement techniques used in the investigations.

4.1.1 'L'-shaped specimen

The test specimens consists of the 'L'-shaped test beam anchored to the silicon substrate at one end, and at the other end attached to the released pad with a ring of 300μm diameter (Fig. 4.1). Beams with similar 'L' -shapes are often used in the designs of real sensors, and so analysis of measurement results provides more information about possible fracture mechanisms in real sensors. In order to obtain various stress profiles in the samples (smaller/larger area under max. stress), specimens with two different anchor layouts were fabricated (notch and smooth).

The released pad and the ring were designed to enable the force to be applied in the direction parallel to the surface of the sample. The layout width of test beams varied between 3 and 5μm, and the radius at the mounting point between 2 and 4μm. The thickness of the specimens was 10μm. In the chip there were placed 6 specimens with three different widths. The overview of the specimen's geometric parameters is given in the Fig. 4.2.

The force was applied by displacing the movable ring with a pin, placed on a micro manipulator. All measurements were conducted under a light microscope, equipped with a CCD camera, allowing the archiving of the course of the test (Fig. 4.3). The highest deflection of the beam before failure was determined by means of standard graphics software by analyzing the record 'frame-by-frame' and
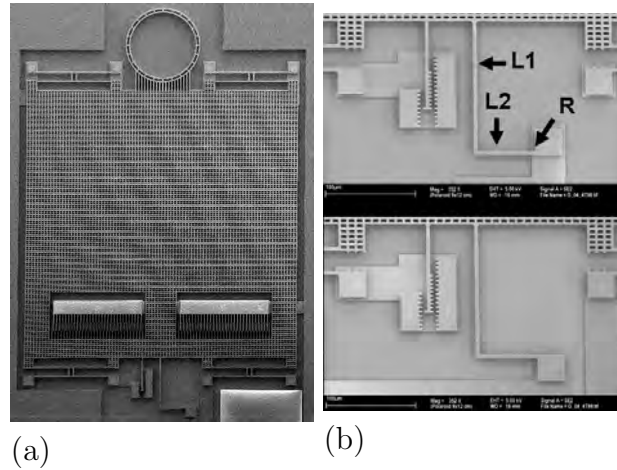
(a)   (b)

Figure 4.1: a) overview of the 'L'-shaped test specimen, b) detail view of functional parts of the specimen - notch (down) and smooth (up) anchor type 'L'-shaped test beam and nonius

Name of the structure	Width [μm] (x)	Radius [μm]	Length L1 [μm]	Name of the structure	Width [μm] (x)	Radius [μm]	Length L1 [μm]
L-06_x (notch)	3	3	58	L-09_x smooth	3	3	58
	4		67		4		67
	5		75		5		75
L-07_x (notch)	3	4	58	L-10_x smooth	3	4	58
	4		67		4		67
	5		75		5		75
L-08_x (notch)	3	5	58	L-11_x smooth	3	5	58
	4		67		4		67
	5		75		5		75

Figure 4.2: Geometric parameters of 10μm thick 'L'-shaped test specimens. The length 'L2' is equal to 150μm and constant for all specimens (see Fig. 4.1). Name of 'L'-shaped specimen consists of: a) letter 'L' b) type number: 6,7,8 -specimens with 'notch' anchor style, 9,10,11 - specimens with 'smooth' anchor style c) layout width of the 'L1' beam of the specimen (3,4,5μm)

reading out the position of the vernier scale, with a resolution of 0.5μm.

The stress field in the structure and correlation between the deflection and values of the first principal stress in the sample, were calculated with the use of FE model created with the FE analysis software package Ansys (Fig. 4.4). The geometric non-linearity has been considered in FE simulations.

The polycrystalline silicon was assumed to be ideally isotropic with a Young's modulus of 161MPa and a Poisson's ratio of 0.23. The simulations have been carried out with consideration to geometric non-linearity. The example of different anchor types with the simulated first principal stress distribution is presented in the Fig. 4.5.

The 'L'-shaped test specimens ('L-06' and 'L-09' - see Fig. 4.2) were also

(a)   (b)   (c)
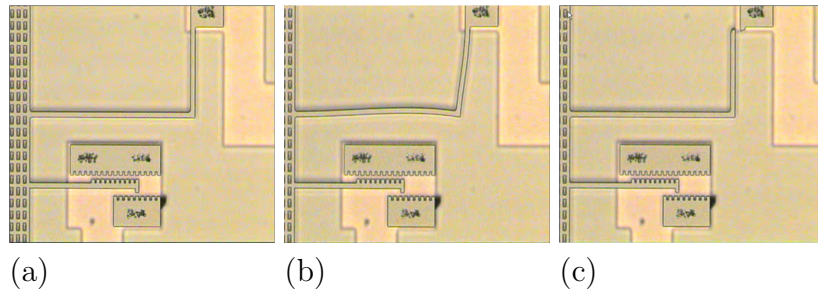
Figure 4.3: Analysis of the recording of fracture strength tests on 'L'-shaped specimen - a method of estimation of fracture deflection of a specimen, a) exposure of 'L' structure before the test, b) last 'frame' before the fracture, the deflection can be read out from the position of the nonius, c) fractured specimen after test
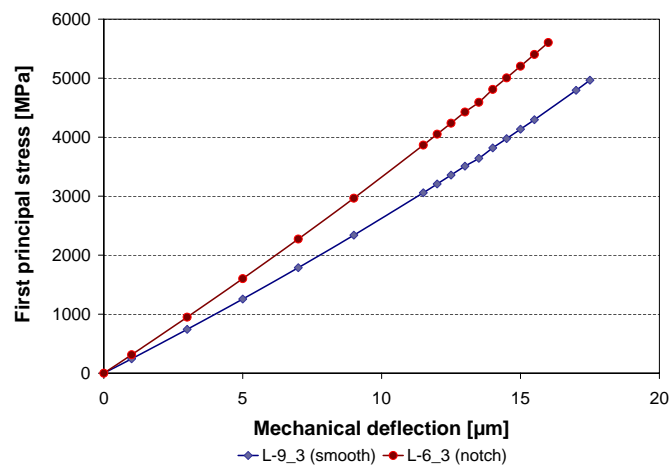
Figure 4.4: Correlation between the deflection and values of first principal stress in the sample on example of 3μm width L-structures with smooth and notch stress distribution and radius 3μm

(a)   (b)
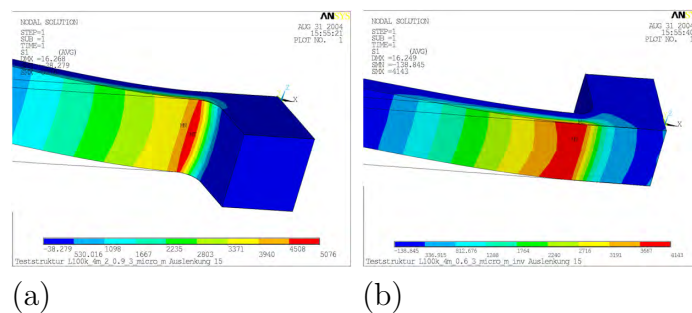
Figure 4.5: Anchor type variation of the 'L'-structure and the FEM simulated 1st principal stress distribution, a) smooth anchor type, b) notch anchor type

applied in the testing of strength properties of 20μm thick polysilicon films. The structures with a width of 3μm have been produced. Due to the smaller dimensions of the chip, only one specimen has been placed on a chip.

39

4.1.2 Straight tensile specimen

The overall shape of the developed tensile test specimen is shown in the SEM image (Fig. 4.6). One end of the sample is fixed to the silicon substrate, and the rest of the specimen is released by etching away the sacrificial layer underneath. The free end of the sample is connected to the release ring. The radius at the anchor, at the beginning and at the end of the beam is three times bigger than the width of the gage section of the specimen.
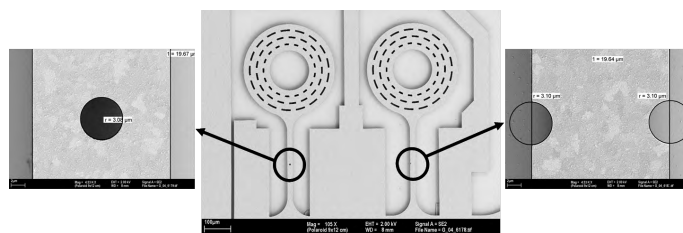
**Figure 4.6:** Scanning electron microscopy photographs of the tensile test specimens with stress concentration elements - width 20 μm, length 250μm

(a)   (b)
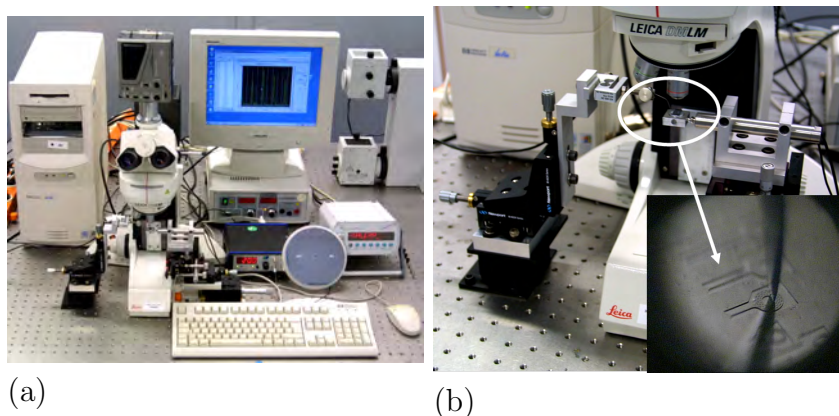
Figure 4.7: Test setup a) with inserted pin in the ring b) of the sample during tensile measurements

The straight tensile test specimens were 5, 20 and 50μm wide and 100, 250, 500, 750 and 1000μm long. The variations with a central hole (radius=3μm) and double half-circular notch (radius=3 μm) were 20μm wide and 250μm long. All tensile specimens were fabricated from 10μm thick polysilicon layers.

The test system used in the measurements is presented in Fig. 4.7. The entire system is installed on a table, eliminating the influence of external vibrations on the test course. The sample is placed on an aluminum holder connected to the horizontally placed piezo displacement unit. The steal pin is connected to a force sensor.

The displacement and the load cell are connected to the PC, controlling the course of the test. With the use of the optical microscope, observation and
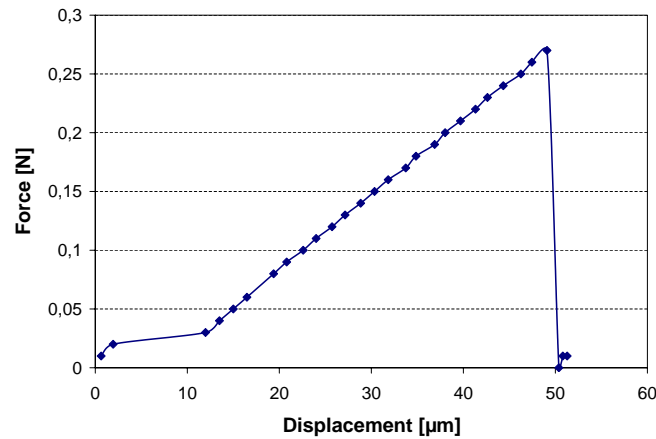
Figure 4.8: Typical force displacement plot of tensile test specimen

(a)   (b)
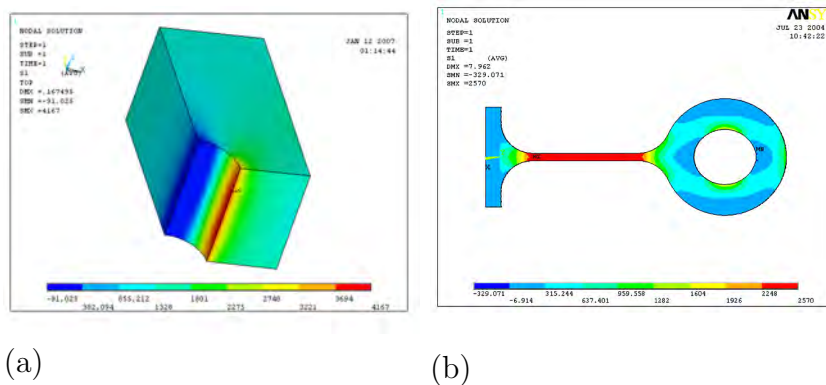
Figure 4.9: a) Fourth - FE- Model of the tensile test specimen with stress concentration (hole, notch) placed in the middle of the structure presenting the distribution of 1st principal stress, b) stress distribution in the straight tensile specimen

recording of the test procedure is possible. The alignments of the pin and the sample are realized using five and three axis stages. The position of the pin in the ring during the initial phase of the test is shown in the Fig. 4.7b.

The force is applied parallel to the surface of the chip. A typical force-displacement record is shown in Fig. 4.8.

The correlation between the tensile force and the stress in the specimen has been determined with the use of the analytical method and 3D Finite Element model (Fig. 4.9).

4.1.3 Three-point flexural specimen

The three-point bending test has been conducted on the straight gage specimen with dimensions specified in Table 2. The polysilicon beam is separated from the foundry die and manually placed on the support plate, fabricated with FIB on

the silicon wafer. The distance between the support points depends on the width of specimen tested. Experiments were conducted using an ultra-micro hardness tester Shimadzu DUH 202. The tester can be operated in the load range between 0.02mN and 2N and the displacement range between 20μm and 50μm. The specimens were loaded with a velocity of 0.5 mN/s. In order to derive the fracture strength from the test results, a Finite Element analysis was performed. The stress distribution in the specimens is presented in Fig. 4.11.

Thickness [μm]	Width [μm]	Distance of supporting points [μm]
10	20	240
	50	240
4	10	37

Figure 4.10: Dimensions of the three-point-bending specimens
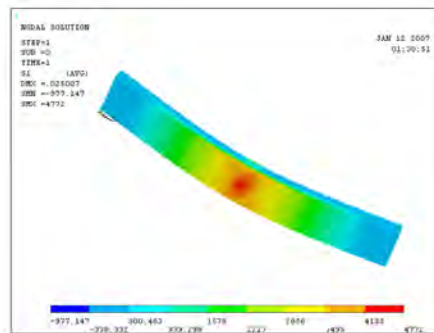
Figure 4.11: FEM simulated stress distribution in the bended specimen

4.1.4 Static fracture strength measurements on rotational oscillators

Rotational oscillators were designed in order to characterize the fatigue behavior of polysilicon. Specimens were fabricated from 10 and 20μm thick polysilicon layers. The detailed description of geometry can be found in the next paragraph. In order to measure fracture strength the specimens were pushed with a micromanipulator until fracture occurred, as presented in Fig. 4.12. The testing progress was recorded with a camera placed in the chamber of the FIB. Similarly like in case of 'L'-shaped specimens, the frame-by-frame analysis of the video was used to find out the highest deflection of the structure before fracture. The fracture deflection

was estimated with the help of simple geometry. The Finite Element analysis was used to establish dependency between deflection and stress in the structure (for details see Chapter 4.2.1.1).
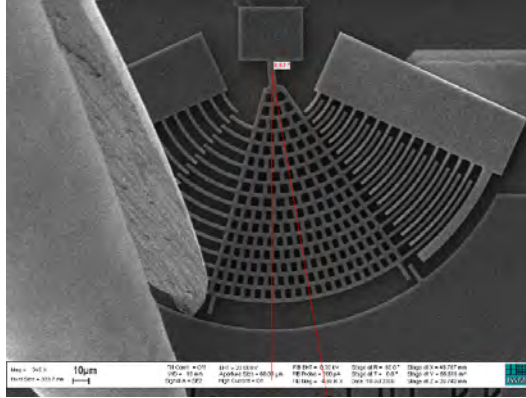
Figure 4.12: SEM micrograph of rotational oscillator under static fracture strength testing with the use of micromanipulator

4.2 Investigation of fatigue on polysilicon under a low-pressure atmosphere

To investigate the fatigue behavior of polysilicon under a low pressure atmosphere, test structures in the form of resonant oscillators were developed. In order to simulate fatigue processes in sensors, designed for 8000 hours of oscillation, with a resonant frequency of 15 kHz ($4.3 \cdot 10^{11}$ cycles) in the conceivable time of a few months (for each sample), the electrostatically driven specimens with a resonant frequency of approx 90 kHz were developed. The following chapters present the specimen's design, methodology of measurements as well as the experimental setup.

4.2.1 Test specimen for fatigue investigations

The rotational oscillator consists of one 19μm long and 5μm wide cantilever, fixed to the silicon die on one side and to a movable mass with 2x14 comb driving electrodes on the other side. The test specimen is presented in Fig. 4.13. The characteristic dimensions are listed in Table 3.

The structure is driven by electrostatic forces. Voltage is applied alternately to either side of the electrodes, oscillation results in a capacity change of the system. The specimens operate at low pressure, approx 1-2 mbar, enclosed in a protection cap bonded with a glass frit. The maximal mechanical deflection of the test specimen defined by mechanical stoppers amounts 11°. According to

(a)

(b)

(c)

Figure 4.13: Rotation oscillator for the investigation of fatigue in $10\mu m$ thick polysilicon, a) test specimen used for fatigue measurements, b) calibration sample with maximal mechanical deflection of 3°, c) detailed view of the beam

FEM simulations, a maximal deflection of the rotating mass of 11 degrees causes a tension of approximately 5.4GPa at the suspension of the sample.

The frequency of the specimens can be measured electrically with an accuracy of $\pm 0.01\%$ for caped chips or with laser vibrometry for specimens without a protection cap in a specially designed on-chip micro-vacuum chamber. The measured resonant frequency is approximately 90 kHz.

The specimens are fabricated in a standard Bosch foundry batch process. Due to the non-uniformity of the trench process across the wafer, the width of the polysilicon structure varies, causing the difference in resonant frequency between several structures with the same nominal layout dimensions. Another important parameter influencing the resonance frequency and the quality factor of oscillations is a gas pressure in the chip.

The out-of-plane deflection of the sample during cycling, measured with a laser vibrometry, is in the range of few nanometers. The change of stress distribution in the structure, due to a few nanometers out-of-plane deflection compared to the specimen thickness of $10\mu m$ or $20\mu m$ has been estimated with FE method and will be neglected in further analysis. A supply voltage of approximately 2V DC and 1.5V AC is required to set the sample in motion. The quality factor is approximately 9000. In the chip there are four specimens placed. Three are used for dynamic measurements and one for calibration. The description of the

Width of the test beam [μm]	5.0
Length of the test beam [μm]	19.0
Radius at the upper mounting point [μm]	2.2
Radius at the bottom mounting point [μm]	1.0
Opening radius of mass [deg.]	50
Number of electrodes on each side of a mass	14
Opening radius of comb electrodes [deg.]	27
Maximal deflection of test specimen [deg]	11
Maximal 1.st principal stress at the max. mechanical deflection [GPa]	Approx. 5.4
Maximal deflection of calibration specimen [deg]	3

Figure 4.14: Geometric parameters of the rotation oscillator (layout values)

calibration procedure will be presented in the next Chapter.

The rotation oscillator of the same geometry and planar layout dimensions has been fabricated in the 20μm thick polysilicon layer. Due to the limited size of chip available in this foundry run only two test specimens could be designed (Fig. 4.15).
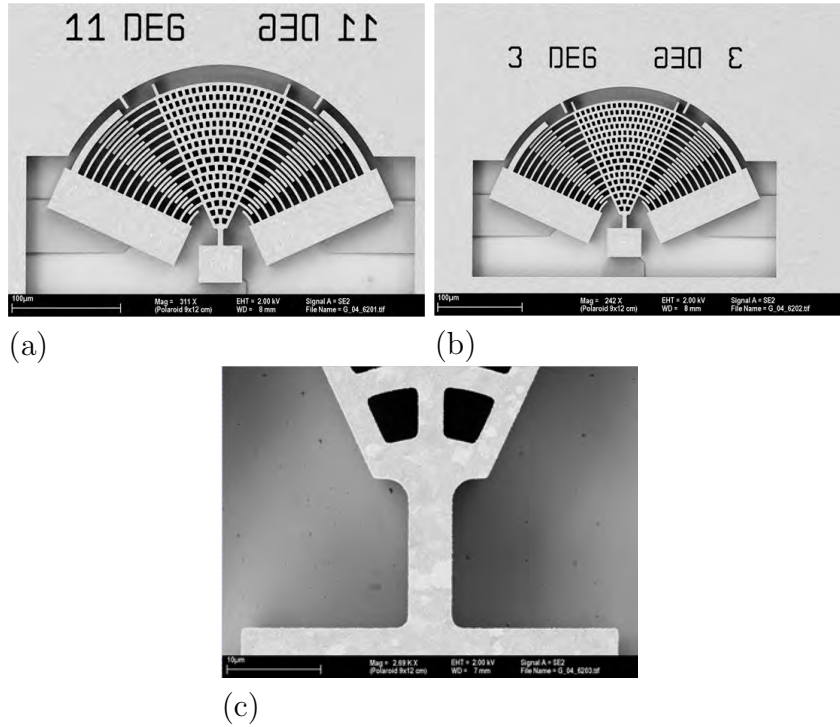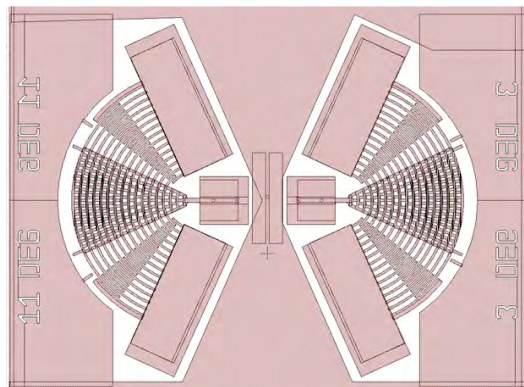

Figure 4.15: Rotation oscillator for the investigation of fatigue 20μm thick polysilicon. Left - test specimen used for fatigue measurements (max. deflection - 11°), Right - calibration sample (maximal mechanical deflection - 3°)

The Quality factor of the specimen is 18000, probably due to the lower pressure in the chip. The set of results measured for 20μm thick samples lays an average approximately 2000Hz higher than the values of 10μm thick specimens.
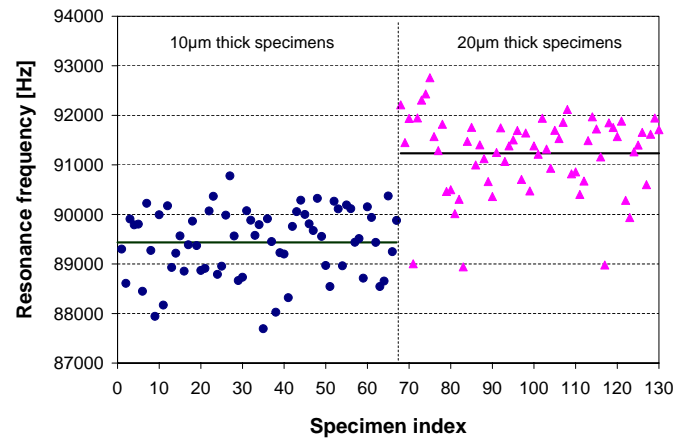
Figure 4.16: Set of data presenting results of frequency measurements, in an initial phase of the experiment, for all investigated rotation oscillators, fabricated from 10 and 20μm thick layers of polycrystalline silicon

Fig. 4.16 presents the set of all resonance frequencies of specimens in the initial phase of the experiment - just after calibration.

FEM modal and stress analysis

The stress distribution in the test beam and the resonant frequency of the oscillator were calculated with the help of 3D FE model. The model consists of 3-D, 20-node higher order solid elements having three degrees of freedom per node representing the test beam. While beam elements were used for the construction of the mass and electrodes. The geometry of the test beam is presented in Fig. 4.17. The polycrystalline silicon was idealized to be isotropic linear elastic, with a Poisson's ratio of 0.23 and a Young's modulus of 161GPa. Given values of Poisson's ratio and Young's modulus are standard values used at Bosch in a design procedure.

(a)   (b)
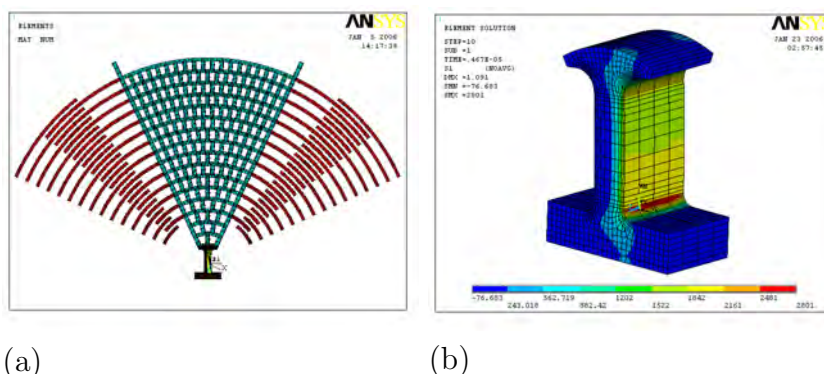
Figure 4.17: a) Overview of the model FE model of rotation oscillator, b) stress distribution in the beam of the oscillator

Stress in the tested beam and resonant frequency of the oscillator depend on the dimensions of a system. Fig. 4.18 and Fig. 4.19 present the dependency of resonant frequency of the specimen on the mean deviation of width from the layout value.
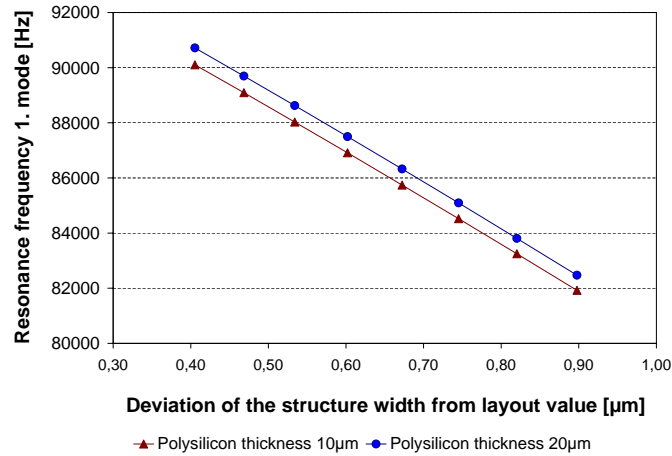
Figure 4.18: Correlation between the mean deviation of the structure width from the layout value and the 1st mode resonant frequency of the rotation oscillators, fabricated from 10μm and 20μm thin polysilicon layers
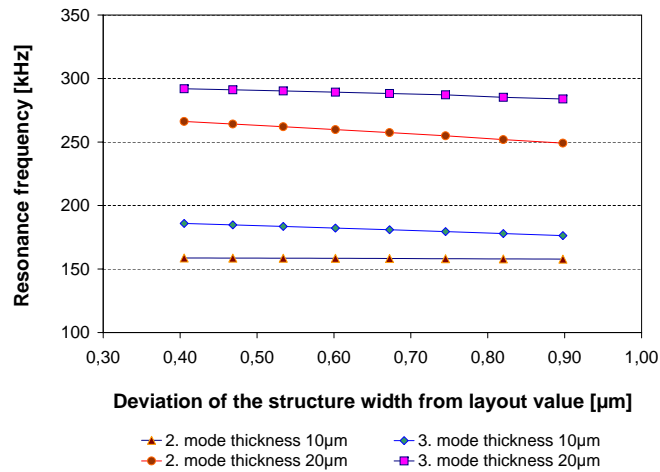
Figure 4.19: Correlation between the mean deviation of the structure width from the layout value and the 2nd and 3rd mode resonant frequency of the rotation oscillators fabricated from 10μm and 20μm thin polysilicon layers

The dependency of the first principal stress on the deflection, calculated for different mean deviations of the structure width from the layout value, is presented in Fig. 4.20. Based on the dimension measurements for every wafer, the appropriate calibration curve is calculated.

47
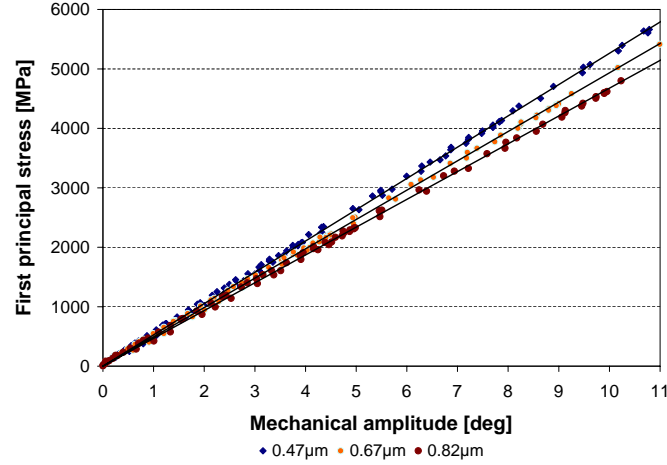
Figure 4.20: Dependency of the first principal stress of the 10μm thick rotation oscillator on the mechanical deflection of the specimen. Example curves are calculated for three typical values of deviation of the structure width from the layout value

4.2.2 Experimental setup

A voltage applied to the comb electrode in the specimen(Fig. 4.13) generates an electrostatic moment which is the driving force of the specimen movement.
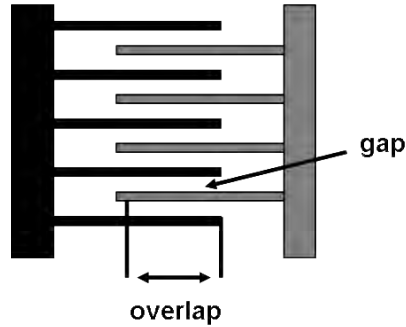
Figure 4.21: Schematic drawing of comb drive electrodes used for electrostatic actuation test specimens used in fatigue investigations

The energy stored in the capacitor of the ith finger of the comb drive is given by:

$$E_i = \frac{1}{2} \cdot q_i \cdot V \tag{4.1}$$

where q_i is the charge of the ith comb finger pair and V is voltage difference across the comb fingers separated from each other with the gap r_i. The force acting on the i_{th} comb finger is,

$$F_i = \frac{1}{r_i} \cdot \frac{dE_i}{d\Theta} \tag{4.2}$$

where the electrode is assumed to move in the Θ direction. Using the definition of capacitance

$$q_i = C_i \cdot V \tag{4.3}$$

the force acting on the i_{th} comb finger can be expressed as:

$$F_i = \frac{1}{2 \cdot r_i} \cdot V^2 \cdot \frac{dC_i}{d\Theta} \tag{4.4}$$

where $dC/d\Theta$ is the gradient of the total capacitance. Due to symmetrical layout of a specimen with two drive electrodes, we need to apply two sinusoidal voltages of the same amplitude and frequency but shifted in phase of 180°, and add to them a DC offset as

$$V_1 = V_{DC} + V_0 \cdot sin\left(\frac{\omega}{2} \cdot t\right) \tag{4.5}$$

$$V_2 = V_{DC} - V_0 \cdot sin\left(\frac{\omega}{2} \cdot t\right) \tag{4.6}$$

Without the DC offset both electrodes would attract the mass of the oscillator with the same force, thus not causing any movement.

The electrostatic moment on each drive electrode can be expressed as follows:

$$T_1 = \frac{1}{2} \cdot \frac{dC}{d\Theta} \cdot \left(V_{DC} + V_0 \cdot sin\left(\frac{\omega}{2} \cdot t\right)\right)^2 \tag{4.7}$$

which is equivalent to

$$T_1 = \frac{1}{2} \cdot \frac{dC}{d\Theta}\left[\left(V_{DC}^2 + \frac{1}{2} \cdot V_0^2\right) + 2 \cdot V_{DC} \cdot V_0 \cdot sin\left(\frac{\omega}{2} \cdot t\right) - \frac{1}{2} \cdot V_0^2 \cdot cos\left(\omega \cdot t\right)\right]$$
$$\tag{4.8}$$

and on the second drive electrode:

$$T_2 = \frac{1}{2} \cdot \frac{dC}{d\Theta}\left[\left(V_{DC}^2 + \frac{1}{2} \cdot V_0^2\right) - 2 \cdot V_{DC} \cdot V_0 \cdot sin\left(\frac{\omega}{2} \cdot t\right) - \frac{1}{2} \cdot V_0^2 \cdot cos\left(\omega \cdot t\right)\right]$$
$$\tag{4.9}$$

The total electrostatic moment is a difference of both

$$T_{tot} = T_1 - T_2 = \frac{1}{2} \cdot \frac{dC}{d\Theta} \cdot \left[2 \cdot V_{DC} \cdot V_0 \cdot sin\left(\frac{\omega}{2} \cdot t\right)\right] \tag{4.10}$$

A symmetric sinusoidal drive voltage at a frequency $\omega/2$, and with a DC offset, produces a periodic electrostatic force with the same frequency.

The total capacitance of the plate capacitor composed of the driving and sensing electrodes is constant for the constant mechanical amplitude. The middle sensing electrode divides the total capacitance into two ranges. Through the
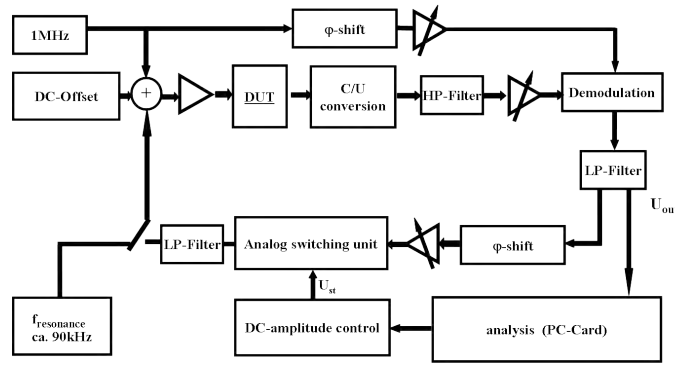
Figure 4.22: Schematic drawing of electrical circuit developed for fatigue investigation on polysilicon

oscillation of the sample the ratio of capacities related to the driving electrodes alternates.

To enable the measurements of the momentary capacitance a high-frequency (1MHz) carrier signal is added to the driving signal with a frequency of approximatelyimately 90kHz. The high-frequency sense signal in its side band frequencies (910 kHz and 1090 kHz) modulated around the HF carrier signal (1 MHz) contains information about the amplitude of the oscillations. It should be mentioned that the amplitude of the sense signal does not depend on the DC offset, although DC offset signal is necessary for electrostatic excitation.

The sense signal is the electrical current, that with the help of CU-transducer, amplifiers, filters and multipliers will be transformed into easy measurable AC voltage. The regulation/control of mechanical amplitude is realized with the external voltage. The specimens are driven in a closed loop (Fig. 4.22). In certain time intervals the frequency and the amplitude of the sample are measured and recorded. In case of deviation from the set value the mechanical amplitude can be automatically adjusted. The control unit allows parallel testing of up to 32 samples in resonance (closed loop) with a constant driving voltage. It is possible to perform long term experiments with good statistical basis. The setup consists of PC, multimeter, multiplexer, and two 19' racks each with 16 slots for the measurement cards (Fig. 4.23).

The power supply is situated on the top of each rack. The temperature in the device due to changing ventilation conditions depends on the number of installed cards and working cards. The temperature of measurement cards placed on the top close to the power supply is higher than those at the bottom of the setup. The difference can be up to 30°C, with maximum temperature of approximately 60°C.

In order to investigate the fatigue of polysilicon in higher temperatures a micro heater, fabricated with thick layer technology, and control circuit have been developed (Fig. 4.24). Although the heater with power of 4.6 W theoretically
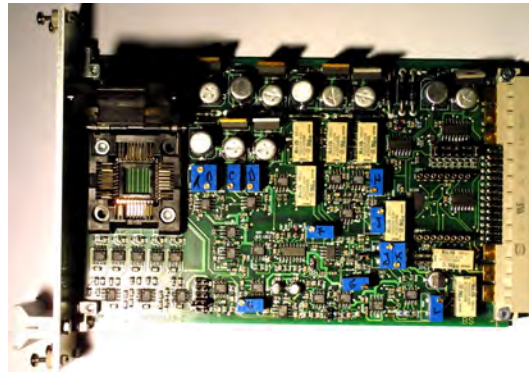
Figure 4.23: Electric circuit (measurement card) developed for measurements of fatigue behavior of polysilicon
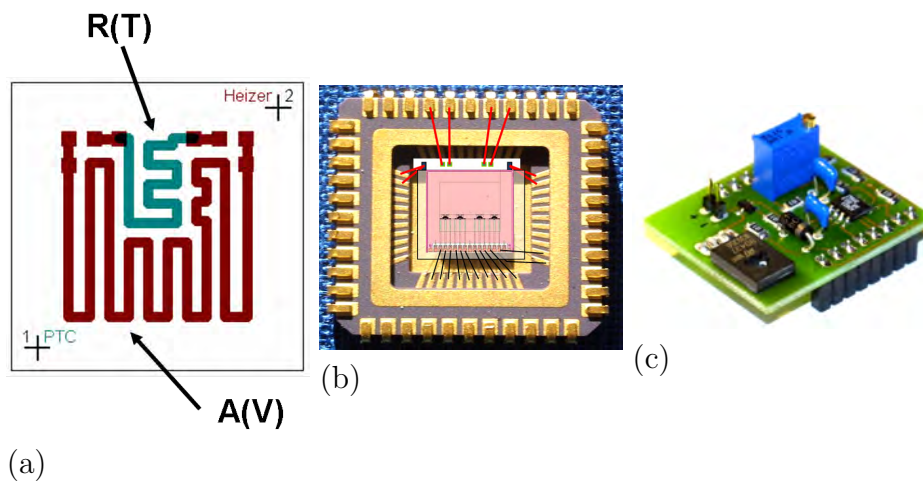
Figure 4.24: a) The schematic drawing of the micro-heater E(V) with the temperature dependent resistance R(T); b) Assembly of the heater placed between the silicon chip and ceramic substrate; c) electric circuit for temperature control

could bring the chip to the temperature of 150°C, due to the stability of the electronic components measurements in excess of 100°C become difficult. The heater is placed between the silicon chip and the ceramic substrate. The aluminum bonding provides connection with the power supply and the control circuit plugged into measurement card. The temperature can be controlled with an accuracy of 2°C.

The calibration curve for the silicon chip mounted on the heater is presented in the Fig. 4.25.
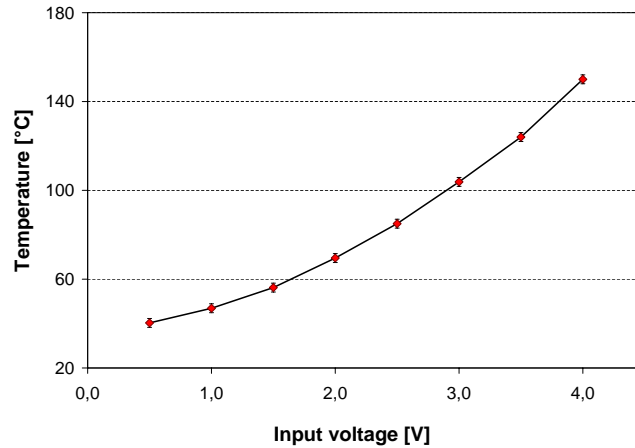
Figure 4.25: Calibration curve of the system heater-sensor

4.2.3 Calibration of fatigue test specimen

Calibration principles

A calibration procedure was developed with the use of a first version of the rotational oscillator.

In the chip four specimens were placed. Three with a maximum allowed mechanical amplitude of 14 degrees, and one sample used for calibration with a a mechanical stopper limiting the amplitude to 4 degrees. The design of both specimens is presented in Fig. 4.26.

(a) (b)
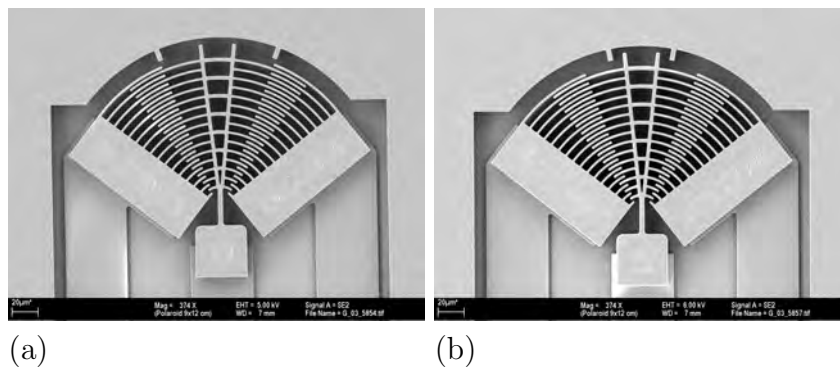
Figure 4.26: Polysilicon rotational oscillator used for development of the calibration procedure; a) specimen with mechanical stopper at deflection of 14deg; b) specimen with mechanical stopper at deflection of 4deg

The stress in the bending beam of the calibration specimen was lower than the fracture strength so that the specimen driven with maximum amplitude did not fracture.

To investigate the correlation between the driving voltages, output signal and mechanical amplitude, the setup shown in Fig. 4.27 was developed. The open chip

(without a silicon protection cap) with resonators was placed in a micro vacuum chamber under a light microscope, equipped with stroboscope light source. The specimen was driven with an electric signal. The electronic circuit was connected to the oscilloscope. The CCD camera placed on microscope controlled by Windows CVI software took photos of the oscillating structures at periodic time intervals. The analysis of the recorded exposures proceeded by Matlab script based on the principal of the correlation.
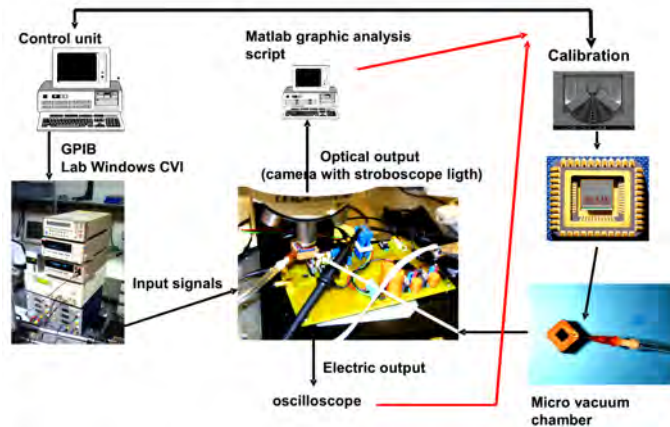
Figure 4.27: Measurement setup for the investigation of the correlation between driving voltage, mechanical deflection and output signal of the resonance specimens used for fatigue testing

The dependency of the optically measured amplitude of oscillations on driving voltage (U_{input}) is presented in Fig. 4.28.
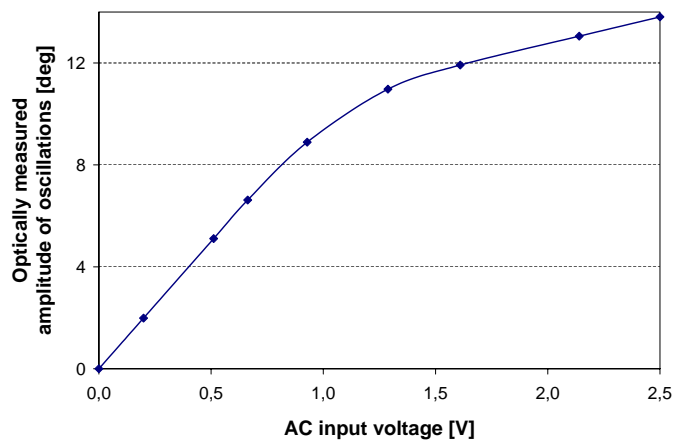
Figure 4.28: Schematic of dependency of mechanical amplitude of oscillations on driving voltage signal

The curve is linear until the amplitude of approximately 7 degrees. The nonlinearity for higher amplitudes is probably due to squeeze film damping in the

range of the electrodes. The dependency is strongly pressure dependent. It is valid for all samples in the chip (under the same conditions).

The dependency of sense signal (U_{output}) on the driving voltage shows nonlinearity, Fig. 4.29. The maximum deflection of the calibration specimens, 4 degrees, is situated on the linear range of the curve. The curve is pressure dependent. The same dependency for all samples in the chip (the same atmosphere) is the basis of the calibration procedure. The calibration method is based on the assumption that a deviation of the specimens dimensions from the layout value are the same for all samples in a chip.

(a)   (b)
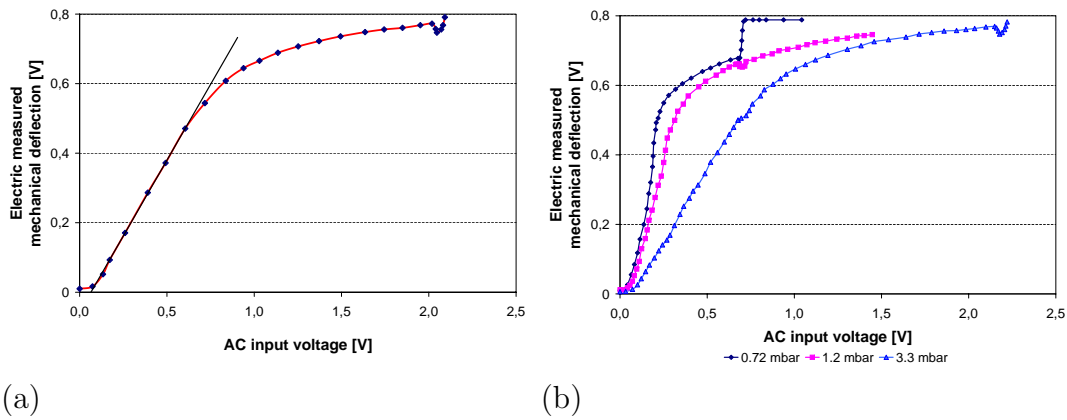
Figure 4.29: a) - Example dependency of mechanical deflection on the driving AC voltage. The dependency is linear for lower amplitudes of oscillations. The electrical offset depends on the settings of the electric circuit. b) - pressure dependency of the sensing signal - driving voltage correlation

The dependency is naturally pressure-dependent (Fig. 4.29). The curve is characteristic for a certain specimen. The value of a sense signal resulting from oscillation with certain amplitude depends on the individual settings of the electronic circuit e.g. amplifiers.

As expected, the correlation between the optically measured deflection and the electrical output signal is linear in the entire measured range. The electrical output signal is directly dependent on capacitance change, that resulting from the growth of the oscillation amplitude (Fig. 4.30).

The drawback of the first layout of the rotational oscillator used to set the calibration principle was that the specimen with a maximum amplitude of 14 degrees did not fracture and could not be used for fatigue investigations.

For fatigue testing new specimens with mechanical stopper at 3 degrees (calibration sample) and 11 degrees (test sample) were fabricated (Fig. 4.13).
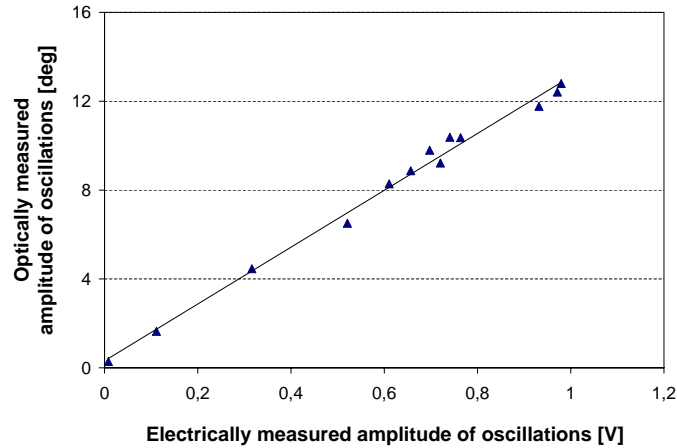
Figure 4.30: Correlation-line between the sense signal and the optically measured oscillation amplitude of the specimen

Calibration procedure

1. Using the calibration sample the $U_{input}3.0°$ resulting with the mechanical amplitude of 3.0° should be measured - once for chip. The specimen has a mechanical stopper at the deflection of 3.0° and cannot oscillate with higher amplitude (see Fig. 4.31a)

2. The new testing specimen placed in the same chip as the calibration sample should be powered with the AC voltage equal to $U_{input}3.0°$. The specimen oscillates with the mechanical amplitude of 3.0°

3. The sense signal $U_{output}3.0°$ should be noted

4. The AC driving voltage should be set to half of $U_{input}3.0°$. The test specimen oscillates with amplitude of 1.5°. The sense signal $U_{output}1.5°$ should be noted (see Fig. 4.31b)

5. The line resulting from measurements created by points $(U_{input}1.5°, U_{output}1.5°)$, $(U_{input}3.0°, U_{output}3.0°)$ describes the dependency deflection - sense signal for the test specimen

The same procedure can be applied for all testing specimens placed in the same chip as the calibration sample. The measurements of the calibration specimen are performed only once, independent on the number of test specimen in the chip. Knowing the calibration curve for specimen, we are able to find the value of the sensing signal for every mechanical deflection considered. The system calculates needed driving signal in order to support the oscillations with constant mechanical amplitude. The accuracy of the calibration method developed was also successfully tested with the use of the new generation of specimens used for fatigue testing.
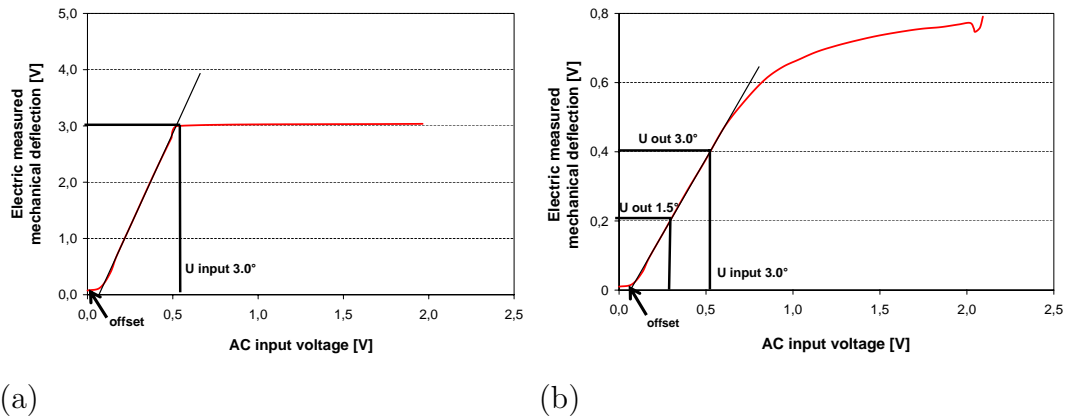
Figure 4.31: Calibration of the rotational oscillator - schematic illustration. a) - calibration specimen oscillating with maximum amplitude of 3.0 deg; b) - Definition of the calibration curve for a testing specimen

4.2.4   Ramp-up fracture strength measurements

Prior to an investigation of constant-stress amplitude fatigue, the static fracture strength of the specimen investigated must be known. It is well accepted that strength of the polysilicon component depends on its geometry and stress distribution in the structure [120, 121]. In order to estimate the ultimate strength of the samples, the mechanical oscillation amplitude of the oscillating sample is gradually increased until fracture occurs (Fig. 4.32); the test procedure takes approximately 60 sec. The testing time has been chosen as the best compromise between requirements of best possible resolution (input voltage step size) and the lowest number of cycles during quasi static testing.
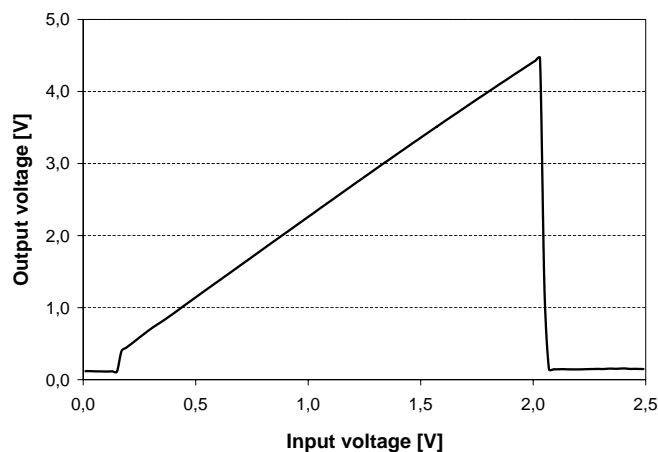
Figure 4.32: Ramp-up testing of fracture strength. Amplitude of oscillations is proportional to the input voltage

Using the results of the calibration specimen measurements and the above curve it is possible calculate the mechanical deflection of the sample in the moment of fracture. Using the calibration curve, the value of the first principal stress in the beam can be calculated. The test procedure is repeated for approximately 20 specimens. The results are analyzed with the Weibull distribution.

4.2.5   High-cycle fatigue measurements

The fatigue investigations are the end-of-life tests conducted with constant amplitude.

4.3   Methods of material and fracture analysis

A variety of instrumental methods has been used in the material investigations and fractography. The basis equipment used in testing was the optical microscope (Fa. Leica). Due to limitations of optical microscopes in the ability to resolve fine details (400-800nm), by properties of light and the refractive materials used to manufacture lenses for applications requiring high magnification and resolution, the Scanning Microscope was used. The spatial resolution of the SEM depends on the size of the electron spot, which in turn depends on the magnetic electron-optical system which produces the scanning beam. The resolution is also limited by the size of the interaction volume, or the extent of material which interacts with the electron beam. Depending on the instrument, the resolution can fall somewhere between less then 1 nm and 20 nm. The Scanning Electron Microscope was equipped with a secondary electron detector and allowed surface element analysis with energy dispersive X-ray spectroscopy. The roughness of polysilicon surfaces was measured with Laser Scanning Microscopy and Atomic Force Microscopy. In a laser scanning confocal microscope, a laser beam is focused by an objective lens into a small focal volume within a fluorescent specimen. The fluorescent light is recollected by the objective lens and transformed into electrical current. Similarly like in SEM, the beam is scanned across the sample. Due to the vertical movement of the specimen the quasi three-dimensional pictures of the surface structure can be achieved.

However, the lateral resolution obtained by scanning with an atomic tip over a conducting surface and measurement of a discrete tunnel current (AFM) is approximately 2nm the ease of specimen preparation for LSM measurements makes it a method of first choice.

The Focus Ion Beam based high accelerated gallium ions beam is in principle similar to SEM. The device was used for preparation of samples for Transmission Electron Microscopy. Required thickness of specimens analyzed by TEM does not exceed 100nm, the information about the features on the scale of 0.1 nm can be obtained. Crystal orientation was measured with Electron Backscatter Diffraction

(EBSD). Due to the diffraction of beam electrons on single lattice atoms, in the resulting image every band refers to a lattice plane. The orientation of the single crystal can be recognized from the pattern. In every single atomic layer a part of the beam is reflected (diffracted) following Braggs law. The knowledge of incoming wavelength of the beam offers a way to calculate the lattice plane that reflected the beam. Today the Kikuchi patterns are received with an SEM equipped with an EBSP-detector. The electron beam strobes the 70° from horizontal inclined specimen dot by dot. For every point the indexing process recognizes the single bands and uses their configuration to get the crystal lattice orientation [122].

5

Results

5.1 Investigation on fracture strength

5.1.1 Fracture strength of 'L'-shaped tensile specimens

Fig. 5.1 presents Weibull strength distributions for specimens with width 3μm, and radius in the mounting point 2μm. The specimen with a notch anchor type is characterized by higher strength than with smooth anchor type of the same dimensions. A large scatter of experimental values is observable. The maximum strength values are almost twice as high as the minimum fracture strength measured with the use of identical specimen. Testing of at least 20 specimens of the same type gives a relatively good statistical basis for the strength analysis.

In order to investigate the variations in the fabrication process, the strength measurements on two charges of polysilicon specimens processed with the same set of nominal process parameters were taken. The following figures present results of measurements for two charges (2004, 2005) of specimens with smooth anchor type L-09_3, L-09_4, L-09_5 and two charges (2004, 2005) of specimens with notch anchor type L-06_3, L-06_4, L-06_5. The parameters of Weibull distributions calculated based on all results from botch charges are also presented in the Fig. 5.2. The number of samples tested from each series varies in the range 20-30.

The results for specimens from both charges show a clear similarity, taking into account the 90% confidence intervals. The summary of mean fracture strengths for all 'L'-shaped specimens is presented in the Fig. 5.3. All structures with notch anchor type show higher values of fracture strength, in average of approximately 18%.

The notched and smooth specimens with the mounting radius of 4μm show the smallest difference in fracture strength. The difference in fracture strength between specimens L-08_3 and L-11_3 lies in the range of measurement error. The strengths of samples with radius 3μm (L-07 and L-10) and width of 5μm, differ the most of up to 30%. The resolution of deflection measurements is 0.5μm which is approximately 3-4% of the total deflection. The error bars presented on the plots
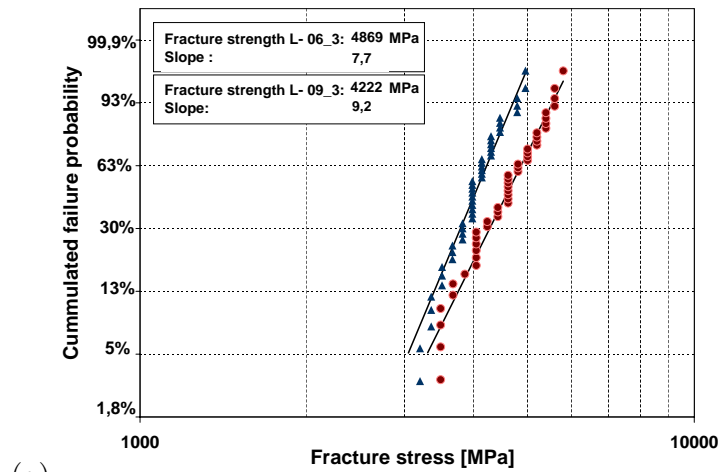
(a)
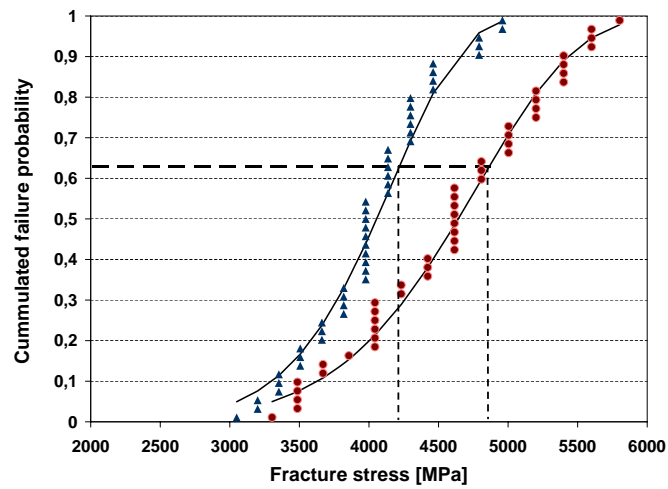
(b)

Figure 5.1: Weibull distribution for 3μm width 'L'-shaped test specimens with notch and smooth anchor type (L-06_3 and L-09_3, see Fig. 4.2)

(a)

(b)
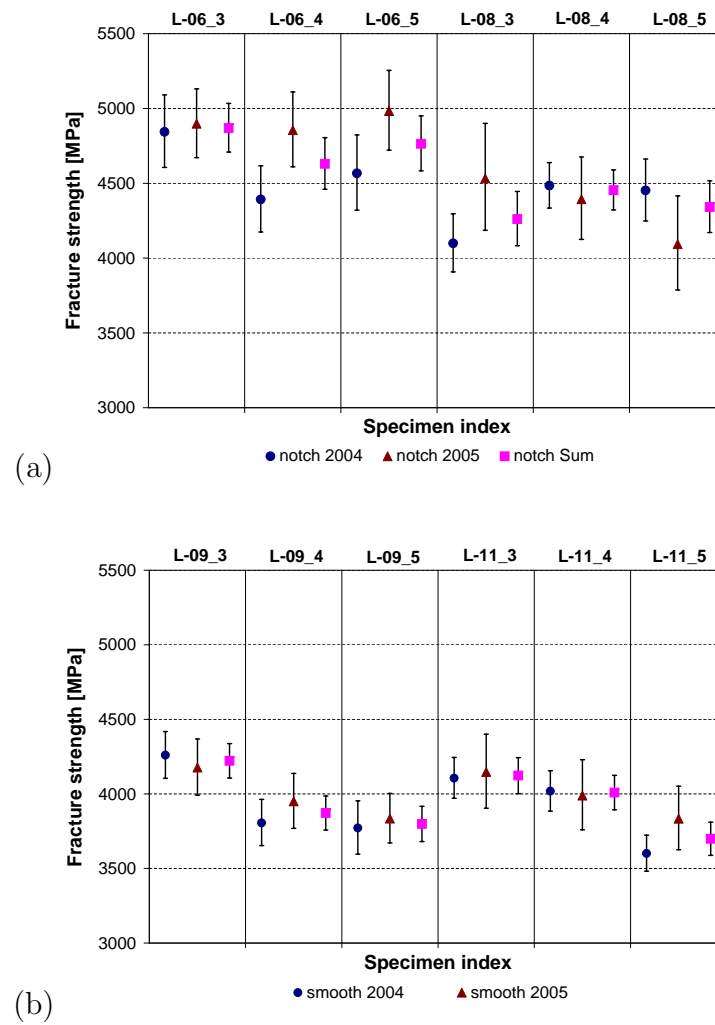
Figure 5.2: Estimation of strength variability of specimens stemmed from wafers fabricated out of 10μm polysilicon in standard foundry process with identical nominal conditions. a) 'L'-shaped specimens with notch anchor type, charges 2004 and 2005, b) 'L'-shaped specimens with smooth anchor type, charges 2004, 2005
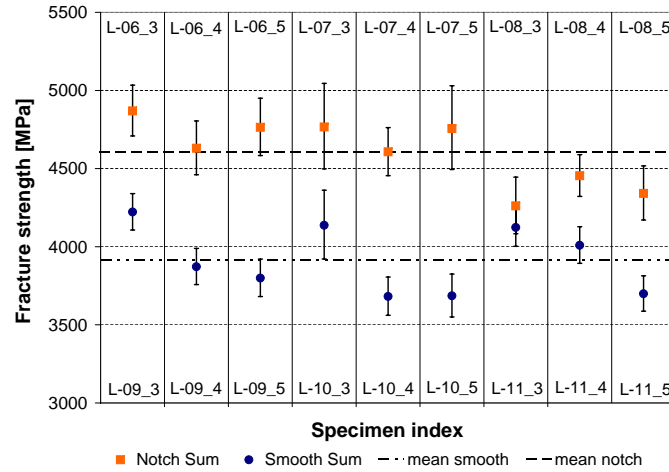
Figure 5.3: Summary of mean fracture strength on the 10μm thick polysilicon test specimens L_06-11 with layout widths of 3, 4, 5 μm

represent 90% confidence intervals, calculated based on the Weibull distribution. The variation of Weibull 'm' parameter representing a defect distribution in the material under investigation is presented in Fig. 5.4.
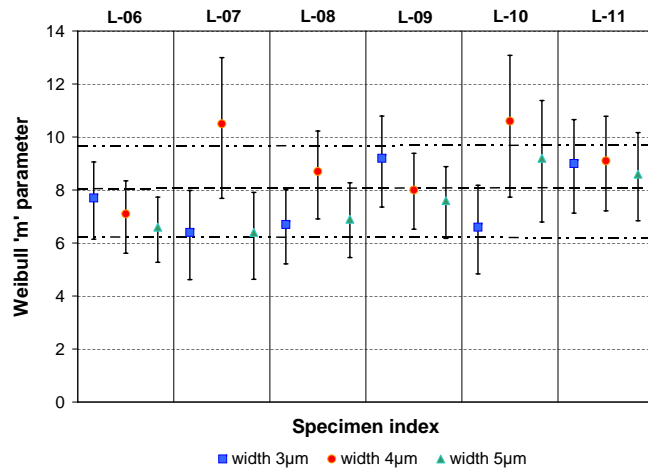
Figure 5.4: Weibull 'm' parameter for all tested 'L'-shaped tensile 10μm thick specimens

As already mentioned in Chapter 4, Experimental, the fracture stress of the 'L'-shaped specimens, if nothing else is mentioned, has been calculated with the help of the correlation between the measured mechanical deflection and the first principal stress, simulated with the FE package Ansys.

Due to the relative wide defect size distribution, some structures fracture in the regions where the stress values are considerably smaller than maximum (Fig. 5.5a). In order to characterize the real fracture stress, a path consisting of nodes has been created on the side wall of the FE model of specimens considered (Fig. 5.5b). The resulting distribution of stress along the structure length, enables

calculation of the fracture stress for each position of fracture origin.

(b)

(a)
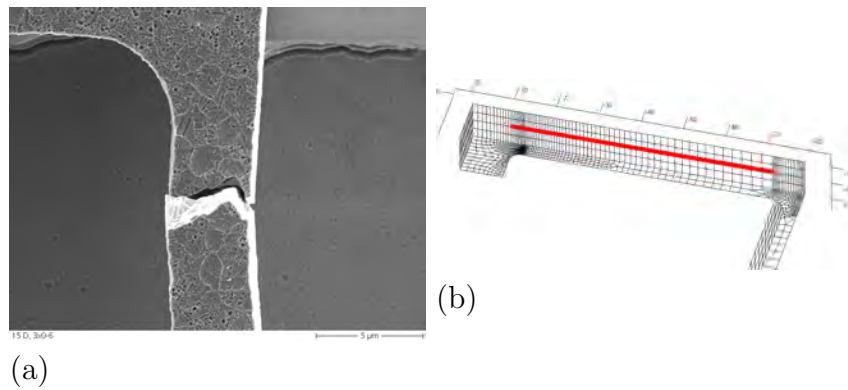
Figure 5.5: a) 'L' shaped tensile test specimen fractured outside from the area of the highest values of first principal stress, b) Detail of FE model of 'L' structure with smooth anchor type. Node path is placed on the side of the structure in the middle of its thickness
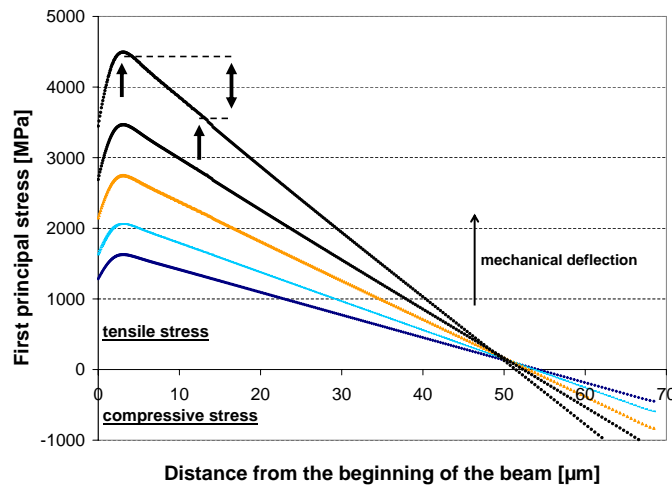
Figure 5.6: Schematic view of a stress distribution along the path length for different mechanical deflections of the specimen. Arrows present example uncertainty of fracture stress estimation resulting from the fracture origin placed outside of region with maximum stress

The position of a fracture origin was identified with the use of light microscopy for all specimens from the charge of year 2005. The 'real' fracture stress was read out from the adequate path curve calculated with FEM for the fracture deflection of the considered sample (Fig. 5.6). The resulting comparison between results calculated according to maximum first principal stress and 'real' values is presented in Fig. 5.7.

Results of investigations on specimens fabricated in special conditions are summarized in Fig. 5.8. No influence of the temperature treatment simulating the glass frit bonding process on the strength properties of the material is observable
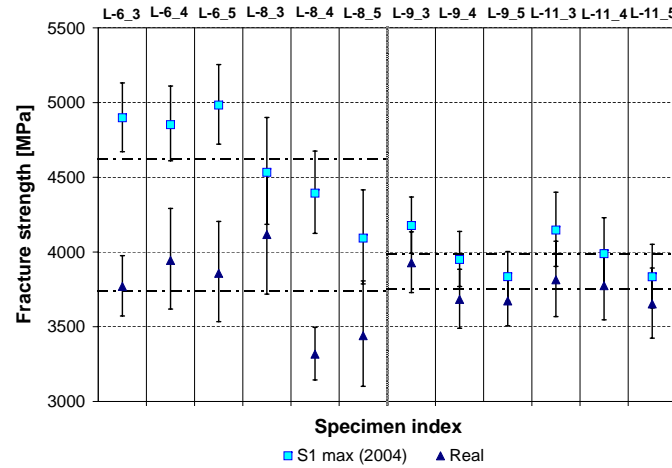
Figure 5.7: The difference between the fracture strength (S1 max)calculated based on first principal stress and the 'real' stress values for specimens with notch anchor type
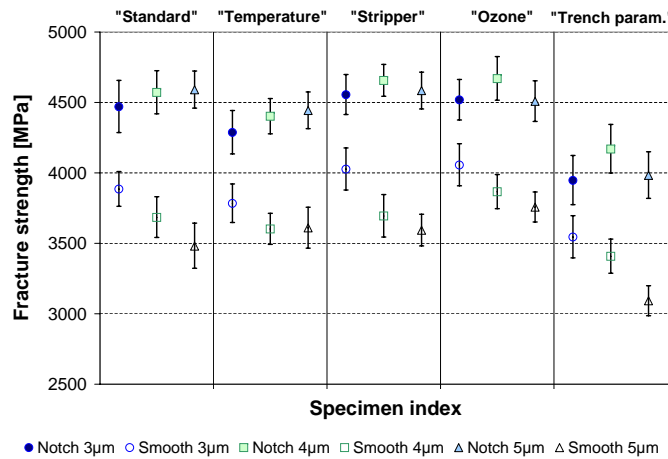
Figure 5.8: Variation of processing conditions - influence on the strength of the polysilicon

('Temp'). Longer stripping time might have modified the side surface of the specimen but its influence on fracture strength was not observed ('Stripper'). Oxidation of the surface in the ozone process after the etching of the sacrificial layer, seems to have a positive influence on the stability of the polysilicon during tensile testing ('Ozone'). Clear influence of different trench conditions can be seen on the example of data measured for 'Trench param' specimens. Results for 'Standard' specimens fabricated in standard conditions are given as a reference.

The characteristic tendency can be seen for specimens with smooth anchor type presented in Fig. 5.8. The fracture strength is decreasing with the increase of the width of the tested beam, this behavior is independent from the processing conditions during a specimen's fabrication.

The comparison between fracture strength of 'L'-shaped specimens fabricated
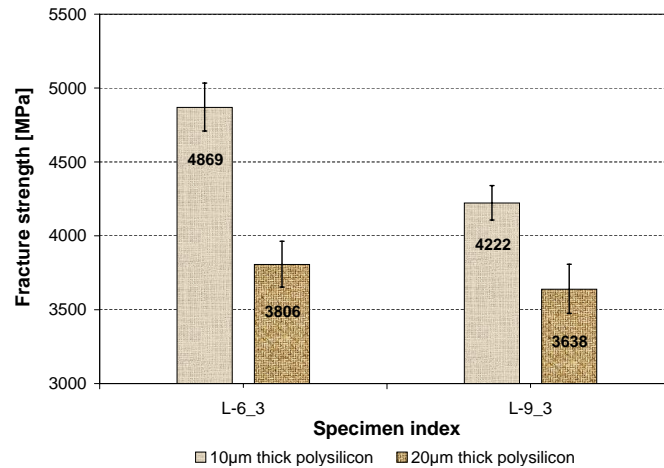
Figure 5.9: Fracture strength of 'L' shaped test specimens fabricated from 10 and 20μm thick polysilicon layers

from 10 and 20μm thick polysilicon films is presented in Fig. 5.9. The noticeably higher strength of the specimens with thickness of 10μm is observable. The difference between strength of notch and smooth anchored samples is higher for specimens fabricated from 10μm polysilicon, than for specimens fabricated from polysilicon layers of double thickness. It should be noted that the plastic package with structures L-9_3 did fall down from the height of approximately 50cm before test. The visual inspection show that 4 out of 28 specimen were damaged.

5.1.2 Fracture strength of straight tensile specimens

Fig. 5.10 presents the comparison between fracture strength of straight tensile test specimens. The lowest strength of 2154MPa was measured on the 250μm long structure with a width of 5μm. Both curves presented on the right side of the plot present results of 20μm width and 250μm long structures with stress concentration elements, double half-circular notch and a central hole respectively.

As already introduced in Chapter Experimental, the strength measurements were also conducted on 5μm width straight tensile specimens, without stress concentration elements and with lengths ranging from 100 up to 1000μm. The obtained results reveal, opposite to what was expected, the tendency of increasing strength with a specimen's length. This oserved issue indicates problems with the adjustment of the samples in the testing setup (Fig. 5.11). The problem is addressed in the Discussion part of the thesis.
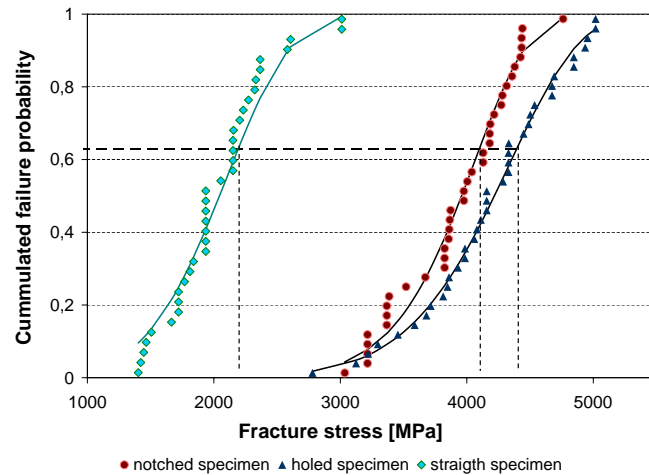
Figure 5.10: Influence of the width and stress concentration elements (notch, hole) on the fracture strength of straight tensile specimens
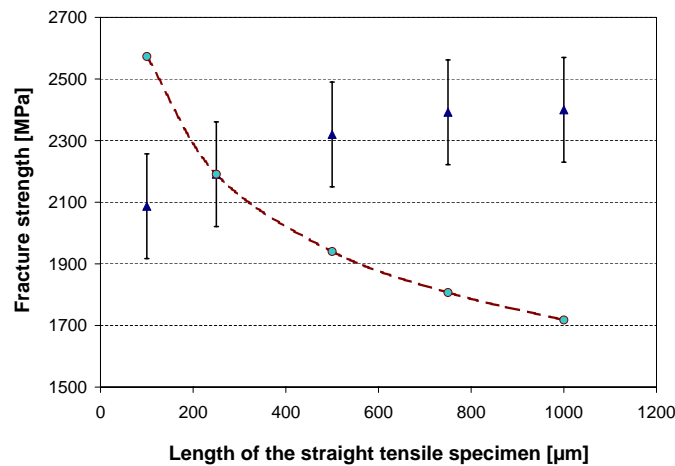
Figure 5.11: Influence of the length of the straight tensile specimen on the fracture strength - experimental results as well as expected tendency based on Weibull weakest link theory (line)

5.1.3 Fracture strength of three-point-flexural specimens

The three-point-bending experiments were conducted on flexural specimens with widths of 50, 20 and thickness of 10μm. Specimens with 4μm width and thickness of 10μm were rotated 90°before being placed on the supporting points, where the force was applied to the sidewall. Resulting thickness of the sample was 4μm and a width of 10μm (specimen '10/4'). The results are summarized in the Fig. 5.12.

In order to investigate the influence of the side-wall roughness, generated in a trench etching step, on the fracture strength of polysilicon MEMS, two series of 4μm width flexural specimens were fabricated in 10μm polysilicon. The force was applied to the trenched side-wall of the specimen, in a similar manner to the above discussed specimen '10/4'. The results indicate that the fracture strength
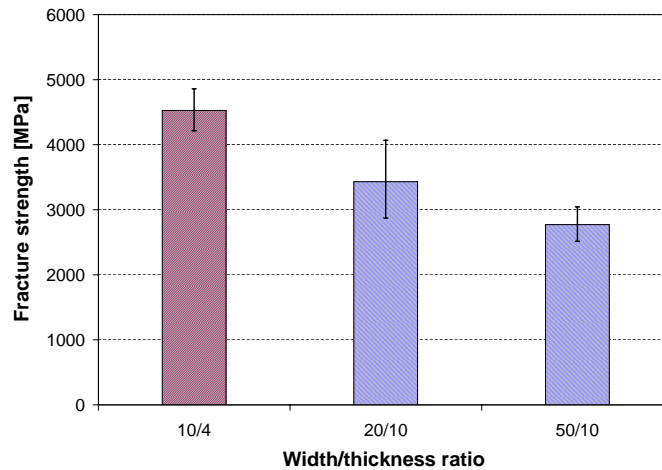
Figure 5.12: Fracture strength of flexural specimens in dependency on specimen's size
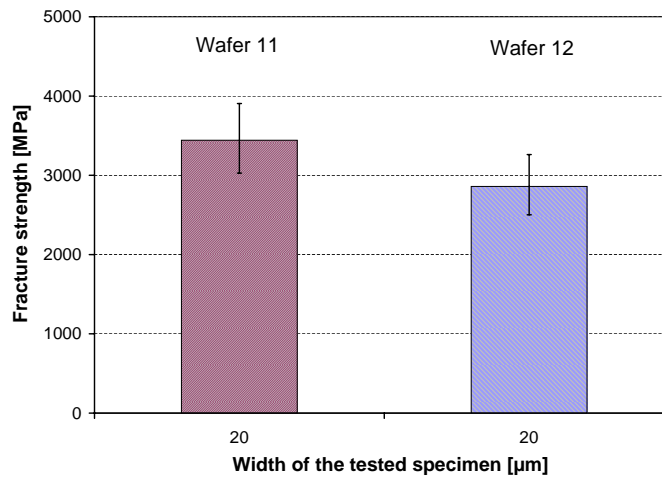
Figure 5.13: Influence of the roughness of the loaded side-wall on strength properties of the flexural specimen

is inversely proportional to the roughness of the loaded surface (Fig. 5.13).

5.1.4 Fracture strength of rotation oscillators

Prior to an investigation of the constant-stress fatigue amplitude of polycrystalline silicon, the static strength limits of the specimens are to be determined. In this work the 10μm and 20μm thick polysilicon layers are the focus of investigation.

The fracture strength of the rotation oscillators has been measured by pushing the structure with a needle until fracture, as presented in the Fig. 4.12.

Fracture strength of 10μm thick rotational oscillator is 7% higher than 20μm thick specimens of the same layout planar dimensions and amounts to 5124MPa.
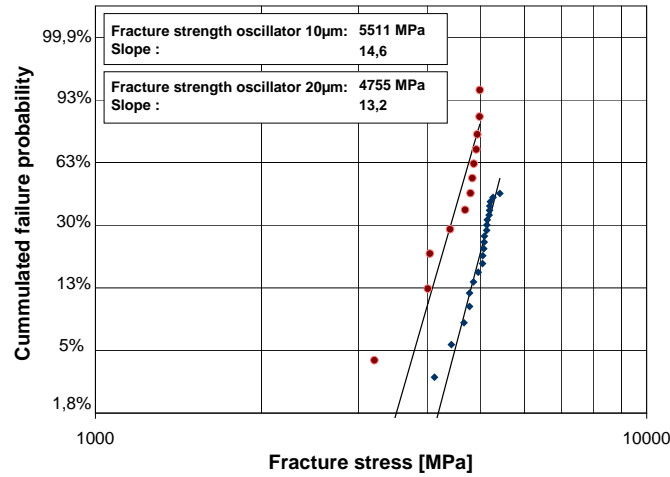
Figure 5.14: Weibull distribution of static measured fracture strength of rotational oscillators fabricated from 10 and 20μm thick polysilicon layers

5.2 Fatigue of polysilicon

5.2.1 Ramp-up strength measurements of rotational oscillators

The first curve on the left in Fig. 5.15 presents typical characteristics of the calibration specimen. The mechanical stopper limits deflection to 3 degrees, which results in a constant capacity and output signal. Sample 1 and 2 show the typical progression of ramp-up measurement of fracture deflection that is proportional to fracture strength. Details of the calibration procedure can be found in the Chapter Experimental.
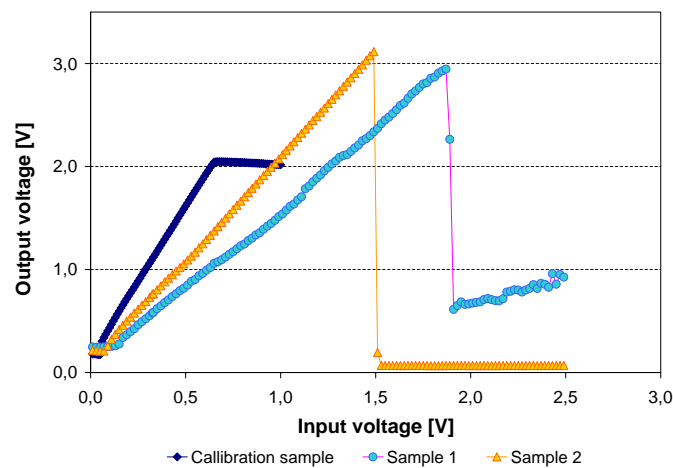
Figure 5.15: Correlation between the input driving voltage and output electric signal proportional to the mechanical deflection of oscillators tested

The measured fracture strength in ramp-up tests of rotation oscillators, fabricated from 10μm thick polysilicon, is approximately 45% higher than the strength

of the oscillator produced from the polysilicon layer of double the thickness (Fig. 5.16). All layout dimensions of specimens with the exception of thickness are identical for the specimens.
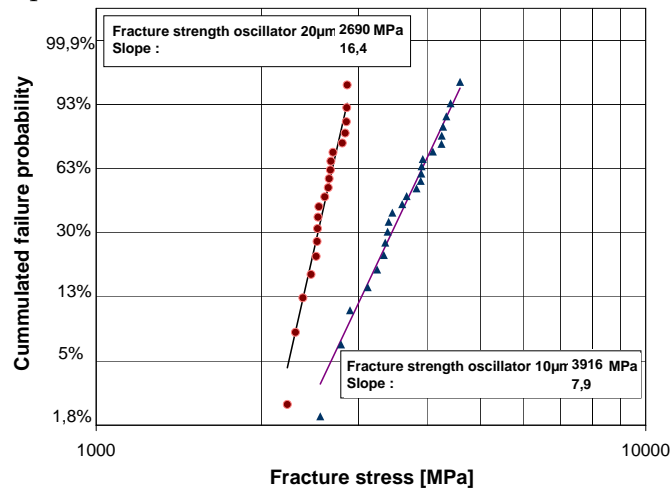
Figure 5.16: Fracture strength Weibull distribution of the rotational oscillators fabricated from 10 and 20μm thick polysilicon layers measured in a ramp-up test

5.2.2   High-cycle measurements

The fatigue investigations were conducted in a low pressure atmosphere where the chip was closed with a glass frit bonded protection cap. The testing facility allows high-cycle testing of polysilicon with constant amplitude. The control unit records the history of all input signals (AC, DC voltage) as well as the parameters describing reaction of the system - amplitude and resonant frequency during the testing.

The history of the amplitude presented in Fig. 5.17 has been recorded for a 20μm thick rotation oscillator. The deviation of the amplitude from the set value of 4.9° as a function of time can be seen in the figure. The internal time of the measurement system is continuously measured from the very first experiment performed, which helps in organization of data recorded during experiments.

The mean amplitude corresponds to the set value and remains constant during the whole testing period, which was in excess of a few months. The detected deviation from the expected value results in automatic correction of an input voltage in order to stabilize the amplitude on a set level. The amplitude can be controlled with an accuracy of approximately ±0.3deg.

The frequency of all tested specimens is measured at the beginning of the experiment and is monitored during the whole duration of test. The end-of-life, high-cycle, investigations were accomplished in the range of temperatures approximately 30-60°C dependent on the position of the measurement card (sample) in the device and the number of other devices tested in parallel. The temperature in
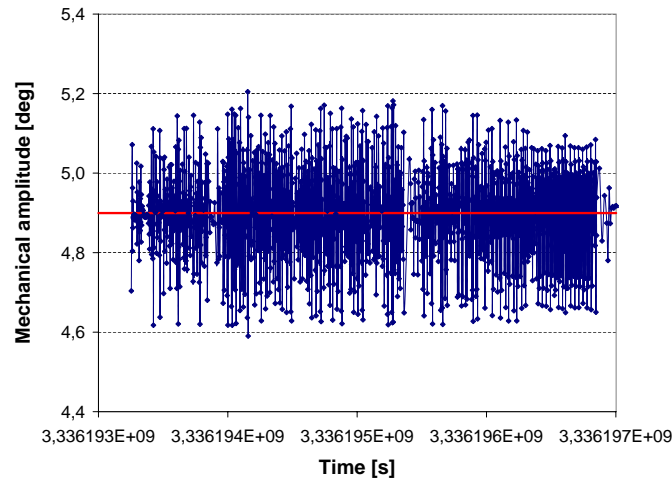
Figure 5.17: History of mechanical amplitude of the rotation oscillator as a function of testing time on a 20μm thick polysilicon oscillator. System time is calculated from the first fatigue test performed with the setup

the testing device varied due to variable heat emission and ventilation conditions subject to number and state (on/off) of other measurement cards.

The number of cycles before failure were analysed with the Weibull distribution. Example results for 10μm thick rotation oscillator are shown in the Fig. 5.18.

The lifetime data resulting from measurements are characterized by an enormous scatter of up to eleven orders of magnitude. Some of the specimens fractured in the first 60 seconds of testing, before the first amplitude/frequency measurement occurred. For those specimens the number of cycles before the fracture is not known and difficult to estimate. Further analyses are based on the worst-case assumption that the oscillators failed during the first cycle. Naturally, the number of the specimens fractured just at the beginning of the test is proportional to the mechanical amplitude of oscillations (Fig. 5.18). Specimens marked with arrows fractured due to electric problems with the testing setup, that resulted with a sudden increase in amplitude. Also in this case, the worst-case assumption has been accepted. For the calculation of the characteristic number of cycles, the number of cycles in the moment of failure has been taken.

The characteristic number of cycles resulting from the fitting of data to the Weibull distribution with the use of the maximum likelihood method informs about the lifetime of 63% of the population.

The summary of the fatigue investigations for 10μm and 20μm thick polysilicon layers is presented in the Fig. 5.19.

The 90% confidence intervals calculated with Weibull distribution for characteristic numbers of cycles, are presented in the form of vertical error bars. Uncertainty of the mechanical stress caused by the variation of mechanical amplitude about the set value is shown as horizontal error bars. The 10μm thick polysil-
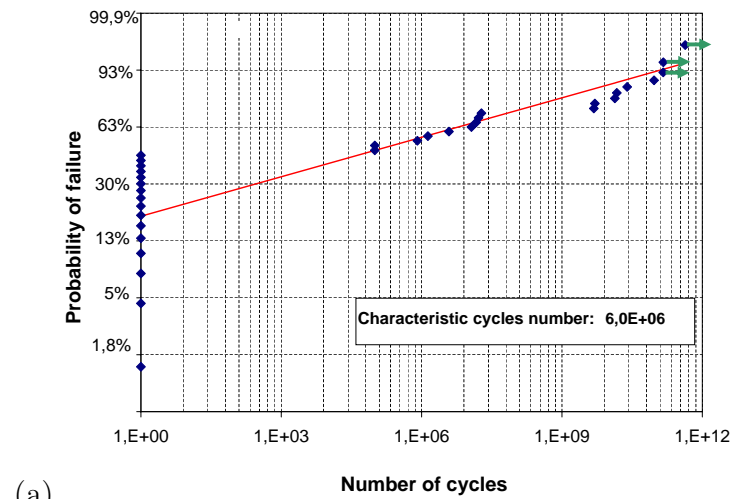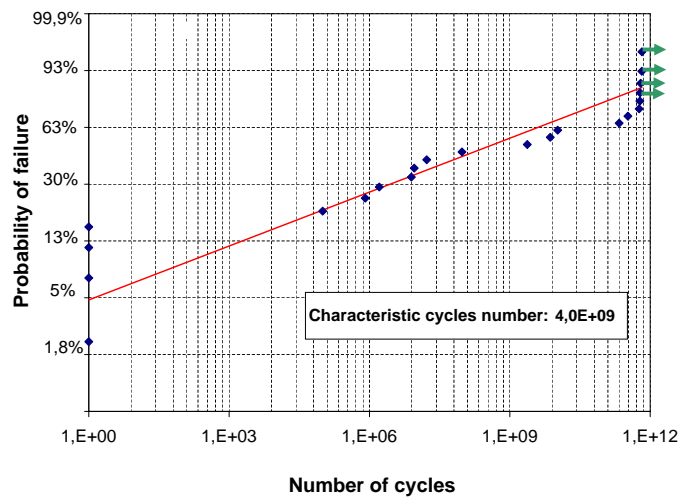
Figure 5.18: Weibull lifetime distribution of 10μm thick rotation oscillator driven with constant amplitude of a) 3570 MPa and b) 3370 MPa
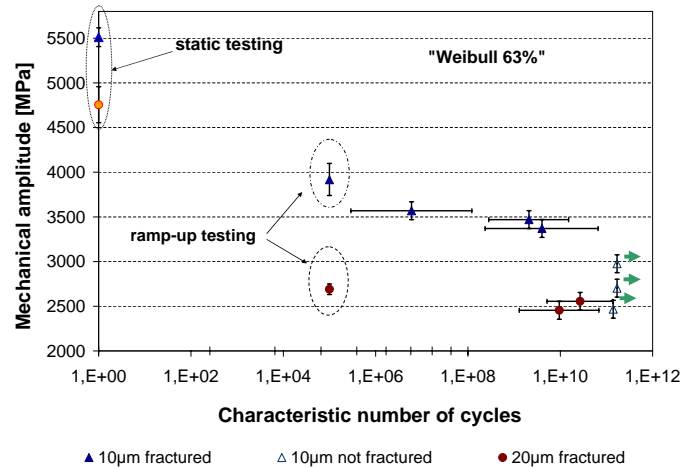
Figure 5.19: Summary of fatigue investigations conducted on 10μm and 20μm thick polysilicon films in a low pressure atmosphere. Dependency between the mechanic load and characteristic number of cycles calculated based on Weibull distribution is presented for a failure rate of 63%

icon films (triangle markers) undergo faster decrease of the specimen's strength during high cycle mechanical loading. Measurements on a total of 30 oscillators fabricated from 10μm polysilicon layers and driven with constant mechanic amplitude lower than 3000MPa (not filled triangles), do not give any signs of fatigue behavior up to and exceeding $2 \cdot 10^{11}$ cycles.

The evolution of the resonant frequency was saved and analyzed for all measured samples through the entire testing period. In the first moments of operation, measurements have been taken as often as possible in order to minimize loss of information in the case of fracture. The example history of the resonant frequency during the test is presented in Fig. 5.20.

Development of the resonant frequency of specimen '4222' is similar to the behavior of specimen '4226' that had been operated in parallel to the same test device (Fig. 5.21).

Similarity of frequency run for both specimens over a longer test period is very characteristic. Changes of the resonant frequencies of both specimens take place in the same time. The frequency drop of the specimen '4226' placed in the rack closer to the heat emitting power supply is higher than for '4222', which may suggest an important influence of temperature on measured frequency.

The influence of the state of the testing device on resonant frequency of specimen '4222' was investigated in detail (Fig. 5.22).

Resonant frequency of the specimen '4222' drops down within the first 40 minutes and achieves 91350Hz. No other changes in the testing device were performed in this time. After 40 minutes of operation with specimen '4222', operation the specimen '4220' placed in neighboring slot 29' failed resulting in the switching off of it's power supply. No changes in the device took place after the test card

(a)   (b)
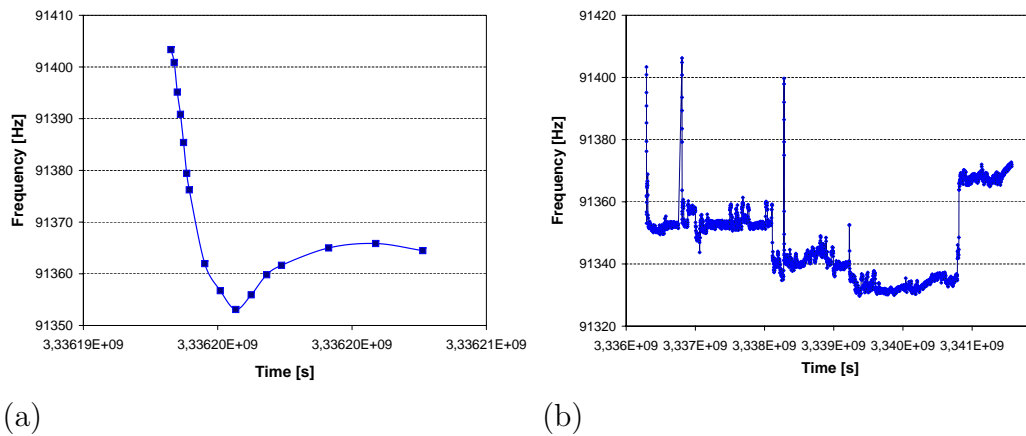
Figure 5.20: History of the resonant frequency of 20μm thick rotational oscillator during high-cycle fatigue investigation, a) change of the frequency during the first 40 minutes of experiment, b) resonant frequency development through the lifetime of the specimen '4222'
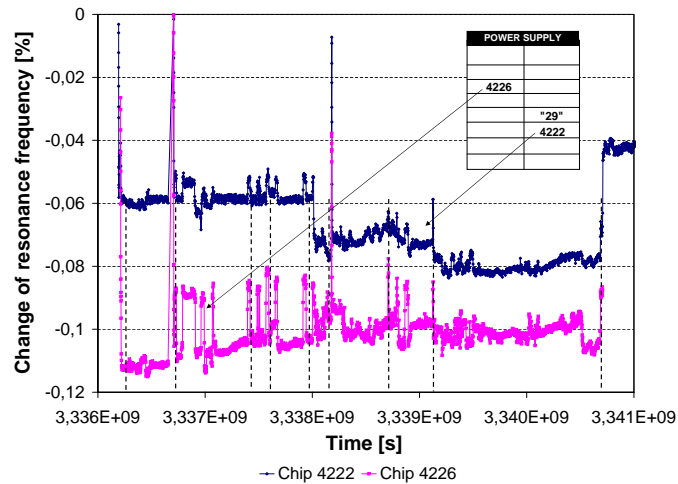
Figure 5.21: Resonant frequency of the rotational oscillators '4222' and '4226' operated in parallel in the same test device

from 'slot 29' was removed. Stabilization of temperature in the testing device resulted in stabilization of the frequency of specimen '4222'. After the test card with a new specimen '4225' was introduced to 'slot 29', the test run was started. In parallel, specimen '4226' was started. Due to the presence of two powered electronic circuits, the temperature in the rack rose, which resulted in a drop of the resonant frequency of specimen '4222'.

In order to investigate the influence of the temperature changes on the resonant frequency of the rotation oscillator driven with the constant amplitude, its temperature was controlled by the micro heater installed directly under the chip. Investigations covered a range of temperatures from the room temperature to approximately 60°C.
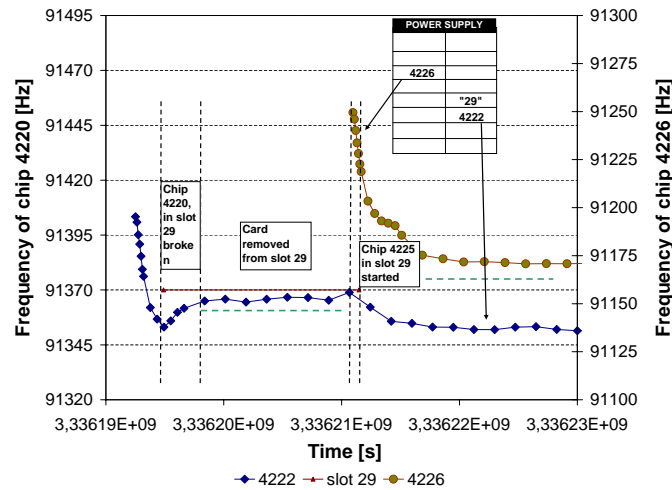
Figure 5.22: Change of the resonant frequency of rotational oscillator '4222' in dependency of current state of the testing device
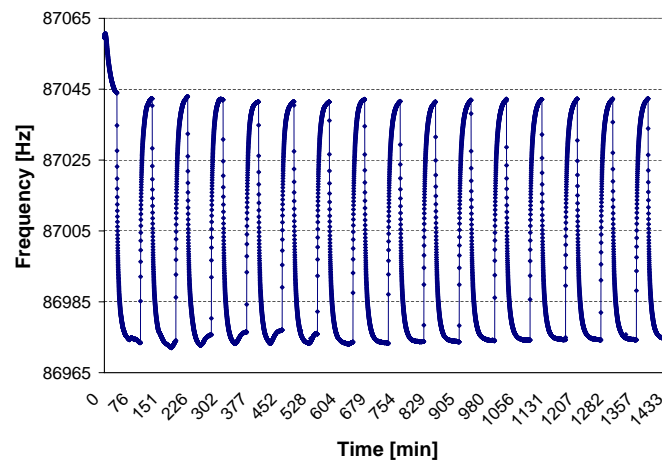
Figure 5.23: Change of the resonant frequency caused by the 24h of cyclic temperature variation

Before the calibration a specimen in room temperature is plugged to the electronic testing circuit and heats up to approximately 30°C, due to being surrounded with warm powered electronic components. After calibration, the measurement card is installed in the testing device. Temperature in the test device depends on the number and position as well as the state (turned on/turned off) of the remaining cards. During the first 40 minutes the temperature of the specimen changes to achieve thermal balance with the testing device. In the next step, the specimen experiences the cyclic change of temperature, controlled by the micro-heater, consisting of 60 minutes of heating up with constant power and then 30 minutes cooling down by reducing the heater power to zero. The resulting frequency record is presented in Fig. 5.23. A clear dependency between the temperature and resonant frequency is observable.

5.2.3 High frequency cyclic loading - influence on the fracture strength

The decrease of the polysilicon strength after high-cycle loading has already been shown in the Fig. 5.19. The question about influence of the short time cyclic loading on the strength properties of the material is addressed in the following chapter. The series of at least 13 specimens were set in motion in resonance for a period of 24h, 48h or a few weeks with mechanical amplitude (load) of 1.2, 2.4, 4.8, 5.3 and 6.0 degrees which corresponds to approximately 670, 1250, 2400, 2650 and 3000 MPa. Every series of the specimens after a specified time of oscillation were stopped and removed from the test device in order to cool down to the room temperature. Afterwards the fracture strength of each sample was measured according to the ramp-up procedure presented in Chapter Experimental. The characteristic fracture strengths depends on the number of cycles for a specimen performed prior to ramp-up testing. The measurements results are presented in Fig. 5.24.

(a) (b)
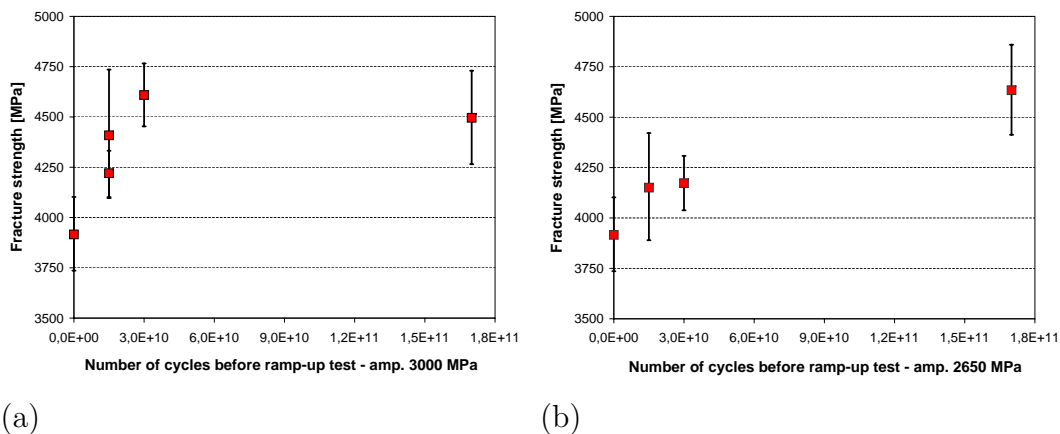
Figure 5.24: Residual fracture strength of 10μm rotation oscillators subjected to high frequency cyclic loading with the amplitudes a) 3000 MPa and b) 2650 MPa prior the ramp-up strength measurement

Clear influence of the time of cyclic loading (number of cycles) on the fracture strength of 10μm thick rotation specimen can be seen. The increase in strength of approximately 18% has been noted for specimens driven with an amplitude of 6.0 deg. already after $3 \cdot 10^{10}$ (48h) cycles. Specimens driven with amplitude of 5.3 deg. achieved a similar increase after as much as $1.7 \cdot 10^{11}$ cycles. A correlation between the amplitude of oscillation and increase of the fracture strength can be seen in the Fig. 5.25.
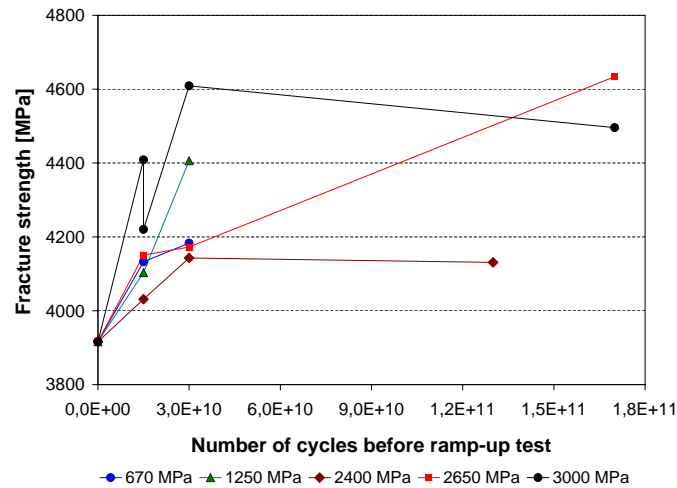
Figure 5.25: Ramp-up fracture strength of 10μm rotation oscillators resulting from the high-frequency mechanic loading with amplitude in the range of 670 - 3000 MPa

5.3 Fracture analysis

The fracture analysis has been performed on selected specimens of each type. Static failure modes were characterized based on fracture surfaces of 'L'-shaped, tensile and 3-pont-bending specimens. For the rotation oscillators used in fatigue investigations, the fracture analysis was performed on specimens after quasi static fracture testing and after high-cycle measurements, in order to characterize the changes in the material.

Results of a fracture analysis on the 'L'-shaped test specimens are presented in Fig. 5.26. The observed fracture origin is located in most cases on or close to the side wall defined with the trench process. The fracture surface presented in the Fig. 5.26a) indicates a crack origin in the region of maximum tensile stress (right side of the picture) close to the right upper edge of the specimen. Characteristic smooth crystal walls, ranging approximately half of the film thickness visible on the micrograph, indicate the fracture along the crystals during the beginning phase of fracture progress. A very interesting region of material structure is visible in the bottom half of specimen's thickness near the sidewall. The size distribution of crystals seems to be influenced by the micromachining process defining the geometry of the specimen. The change of crack's expansion direction is another characteristic features. Fig. 5.26b) shows the specimen where the fracture origin was placed in the region of upper right corner. The crack expansion in the first 20% of specimen's width left traces in the form of a few crystal terraces through the whole thickness of the sample. As the microstructure changes, i.e. the presence of big elliptic crystals with the height of up to 2.5μm or small almost round crystals placed in the neighbourhood of long columnar grains, the fracture surface becomes rough exhibiting high complexity. The characteristic thin film is visible on the right side of the micrograph (on the picture white) in Fig. 5.26b). Fig.

5.26c) - pictures a common case of fracture with delamination visible on a sidewall affected by a maximum tensile stress. Fig. 5.26d) presents a rare example where the fracture origin is placed directly on the upper edge. Fig. 5.26e) shows a fracture that probably originated from the trench process residues placed on the upper (transparent) edge of the specimens. On the fracture surface presented in (Fig. 5.26f) there are small voids of diameter approximately 100-200nm visible.
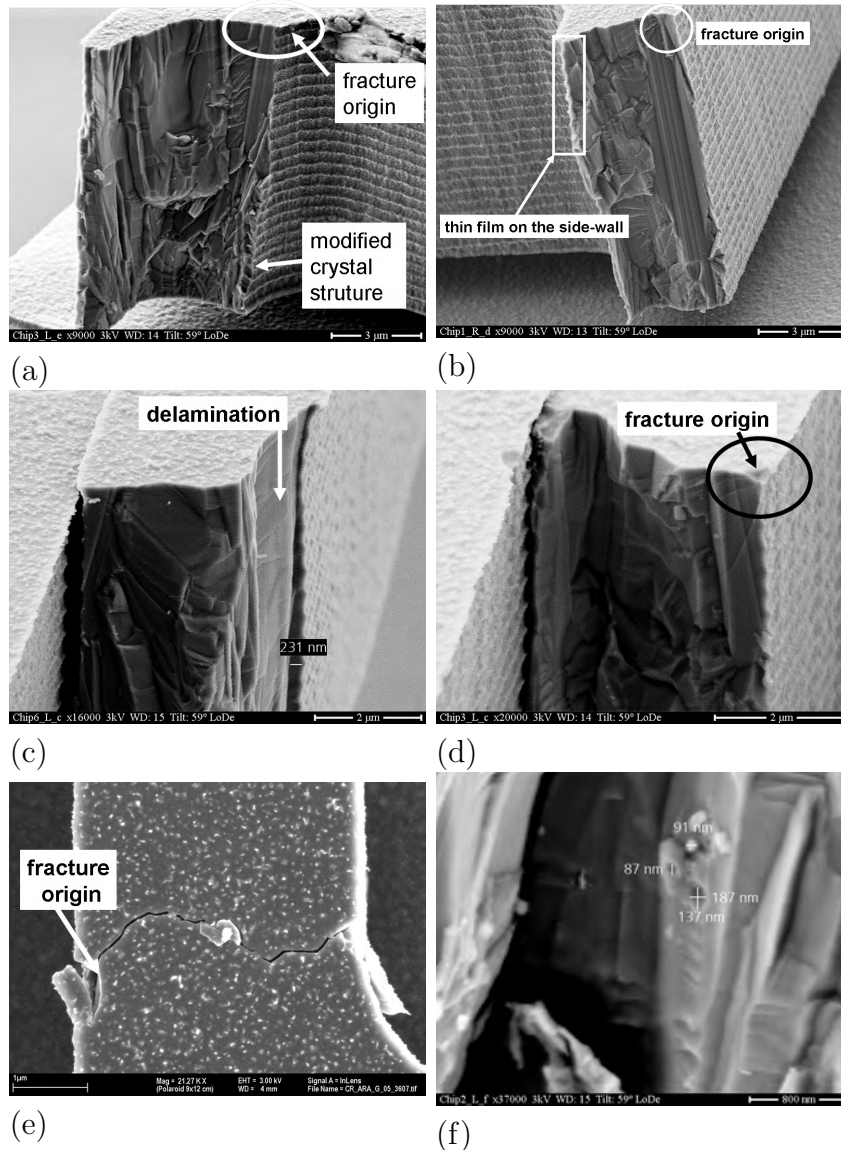
Figure 5.26: SEM micrograph - typical look of fractured 'L'-shaped specimens

The Laser Scanning Microscopy was used to measure the roughness of sidewalls of fractured 10μm thick 'L'-shaped specimens. After fracture the beam was separated from the anchor with FIB and placed on its side-wall under the microscope. The roughness has been measured on the bottom, middle and upper part of the side-wall. Measurement positions on the specimens are presented

in Fig. 5.27. The results of average roughness measured on 20 specimens are presented in Fig. 5.28.
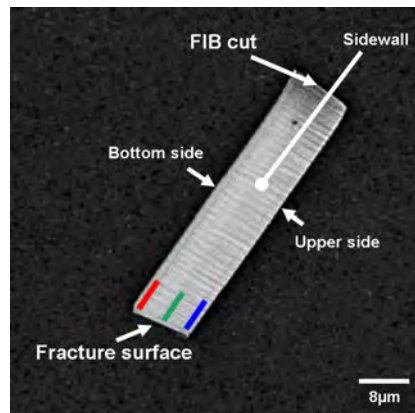
Figure 5.27: Polysilicon beam under the Laser Scanning Microscope and schematic representation of measured regions
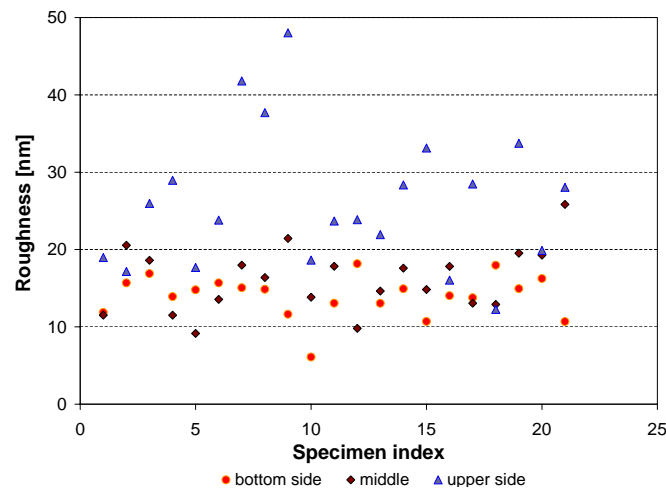
Figure 5.28: Roughness of polysilicon side-wall of 'L'-shaped test specimens, defined during trench process, measured with LSM on three different positions

A tendency that the average roughness on the upper region of the side-wall is higher than on the bottom region can be seen. In the Fig. 5.29 the correlation between fracture stress of the 'L'-shaped test specimens and average roughness measured on the bottom, middle and upper region of side-wall can be seen. The straight line in the figure shows a light trend of decreasing fracture stress with increasing roughness of upper-regions of the side-walls.

Fig. 5.30 presents the fracture surface of the tensile test specimen with an axially placed hole - stress concentration element. The magnification of the area indicates the fracture origin to be placed just under the sidewall surface. The silicon sidewall seems to be covered with a very thin layer, with the thickness of
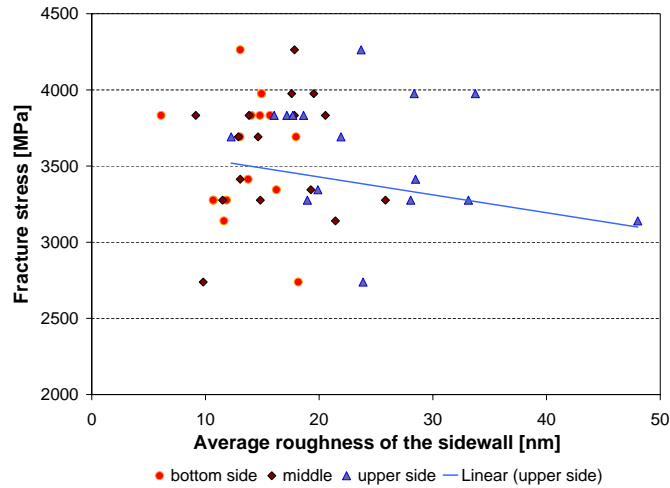
Figure 5.29: Correlation between fracture stress of the 'L'-shaped test specimens and average roughness measured on the bottom, middle and upper region of side-wall

few tens of manometers. The interface between the polysilicon and the side layer is visible on the micrograph just under the fracture origin.
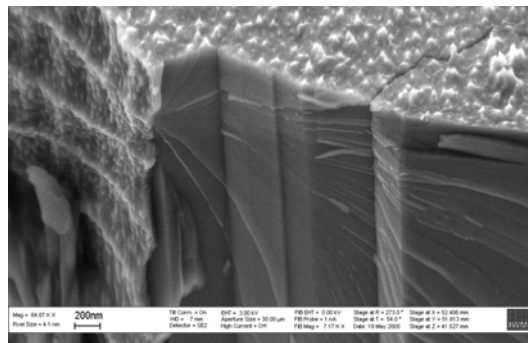
Figure 5.30: SEM micrograph of notched tensile specimen after fracture. Crack origin is placed under the side-wall layer created in trench process

The fracture surface of specimens tested in 3-point-bending presented in the Fig. 5.31 seems to be extremely similar to this presented in Fig. 5.30 where the crack origin was presumably placed in the interface between the polycrystalline silicon and a momentarily not closely defined 'side layer'.

The micrograph Fig. 5.31 also seems to confirm the existence of the side layer with the different contrast visible on all sides of the specimen.

All above mentioned features were also observable for 20μm thick 'L'-shaped specimens, typical examples are presented in the Fig. 5.32. The rare crack branching in 10μm thick 'L'-shaped specimens became typical qualities of 20μm thick structures of the same geometry.

The residues after trenching process can also be seen on the surface of vertical side walls and structure edges in some cases even before fracture (Fig. 5.33a).
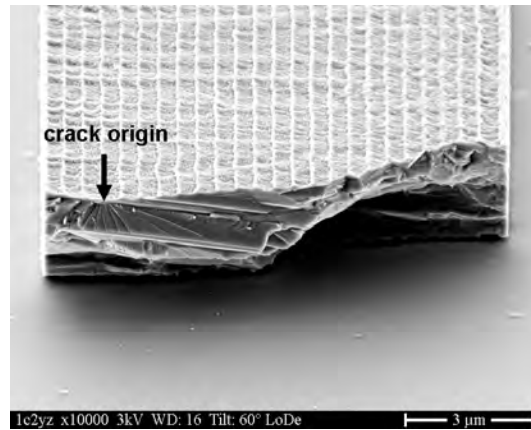
Figure 5.31: SEM micrograph - typical look of fractured three point bending specimen. Crack origin is placed under the side-wall layer created in trench process

(a)   (b)
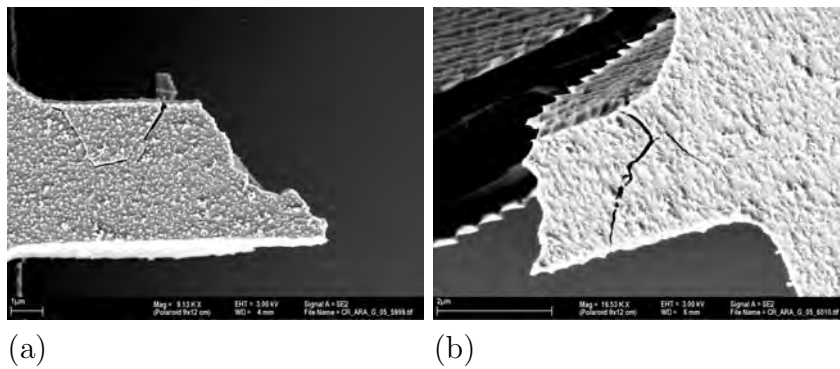
Figure 5.32: Crack branching in the 20μm thick polysilicon films

Similar observations can be made while analyzing the fracture of rotational oscillators independently on the material thickness (Fig. 5.33b).

(a)   (b)
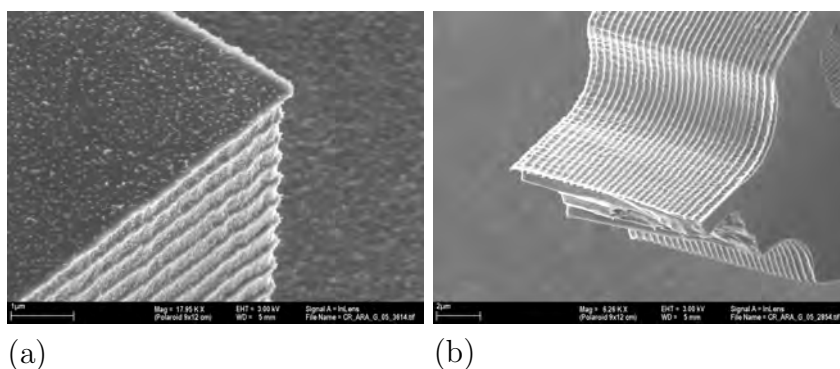
Figure 5.33: a) View of trenched side surface of the polysilicon specimen covered with a thin layer, b) fracture surface with a visible thin layer separated from the polysilicon

In order to verify the observations of the 'side-layer' on the surface of the polysilicon specimen, the polysilicon etching test was performed. The side layer

was expected to differ with the structure and/or composition from the silicon. The gradual etching of silicon with gas-phase SF_6, starting from specimen's surface was conducted. The results of the investigations are presented in the Fig. 5.34.

(a)   (b)

(c)
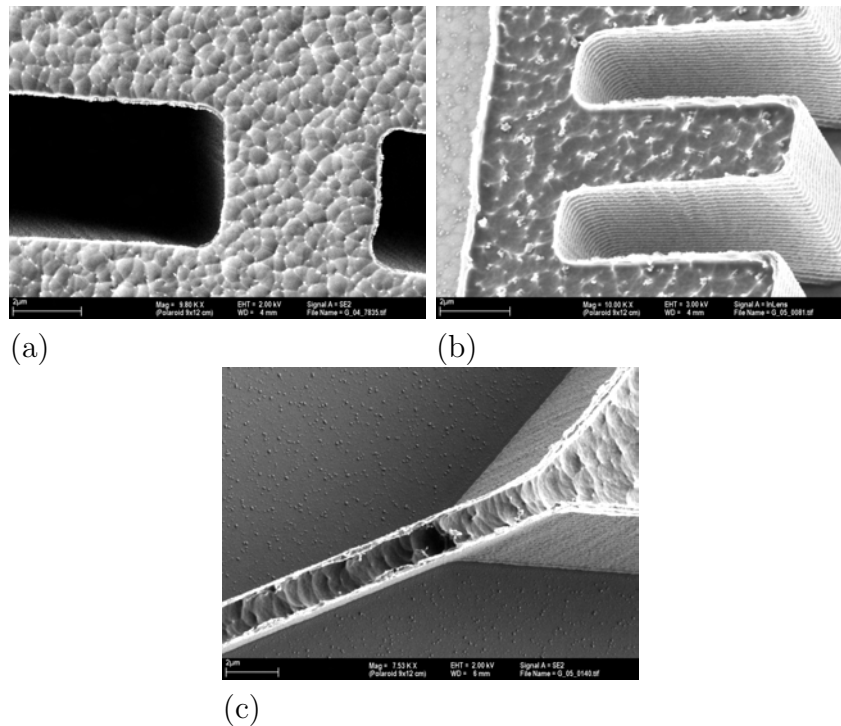
Figure 5.34: SEM images presenting progress of gradual etching of polysilicon with SF_6. a) 2μm removed, b) 4μm removed, c) 7μm removed. 'Side-layer' covering the sidewalls of the polysilicon specimens visible

The results of etching investigations show that the etch process residues present on the vertical surfaces have different structure and chemical composition than polysilicon. Results of EDX investigations are presented in Fig. 5.35.

The investigations show presence of carbon, oxygen and fluorine in the 'side-layer'.

(a)

(b)
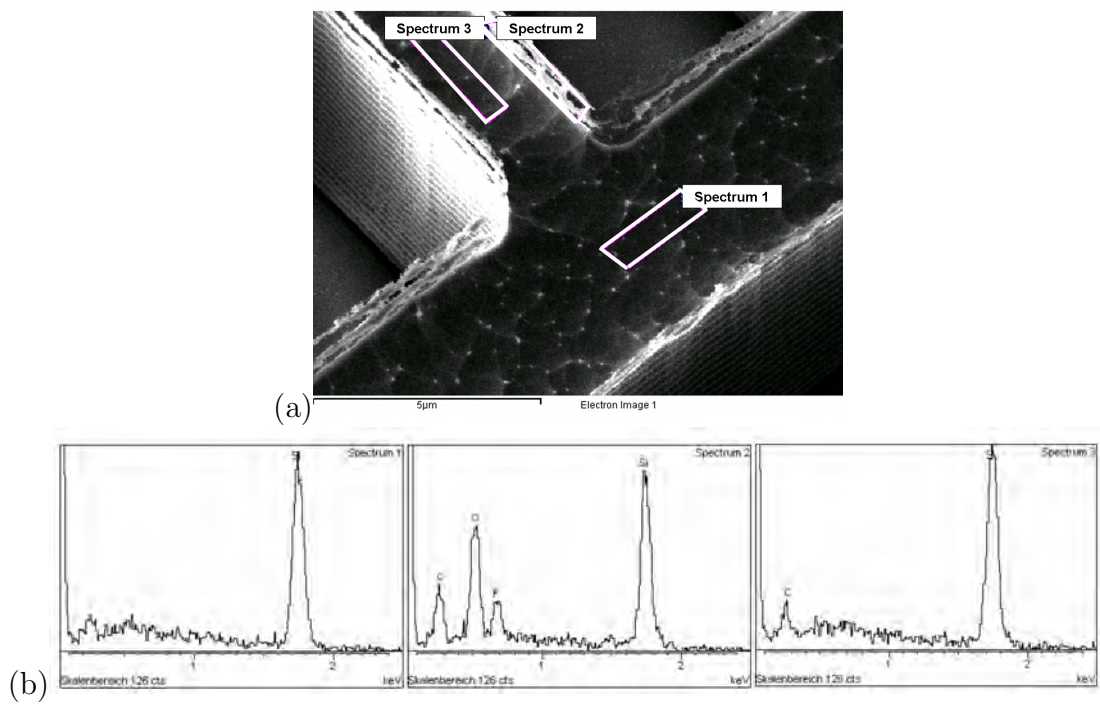
Figure 5.35: EDX investigation of chemical composition of etch residues, a) position of spectra analyzed, b) resulting spectra

6

Discussion

6.1 Fracture strength in polycrystalline silicon

A strong influence of size on the fracture strength of specimens has been broadly discussed in the literature [67, 68, 69, 87, 89, 90, 80, 53, 71, 72, 92, 43]. Specimens of different microstructure, thickness and geometry were tested with various methods. Results indicated the existence of a size effect in polycrystalline silicon. The tendency of decreasing fracture strength with increasing specimen size has been captured by Bagdahn [93, 40] in the Fig. 3.11 presented in the Chapter Fundamentals of the thesis.

Results of initial fracture strength measurements (Fig. 5.1) on 'L'-shaped specimens performed for this thesis have already shown the influence of the specimen's geometry on the strength properties of polysilicon components. The fracture strength of 'L'-structures with notch anchor type was 15% higher than the strength of specimens with the smooth anchor type and the same dimensions.

The scatter of values measured for a series of identical structures is considerable. Maximum values are typically two fold higher than minimum. High scatter of fracture strength is a typical property of brittle materials [11].

The area under the maximum stress of a 'L'-shaped specimens with smooth anchor type, appears to be bigger than in case of the specimen with notch anchor type. The FE simulations with stress distributions of both specimens are presented in Fig. 4.5. In order to conduct a precise comparison of strength and size of the different specimens the procedure for effective size estimation needs to be formalized.

In order to support general conclusions about an influence of a geometry and size on fracture strength of a certain material, the repeatability of the fabrication process has been verified and deviation of strength due to processing variation was investigated.
A comparison of the fracture strength of polysilicon measured on 'L'-shaped specimens fabricated with the same layout and with nominally identical process con-

ditions in two charges (2004, 2005) produced in year 2004 and 2005, respectively, is presented in Fig. 5.2.

The results show a very good repeatability of fracture strength in the charges tested, especially in the case of specimens with a smooth anchor type independent from their dimensions. Error bars in the figure represent 90% confidence intervals.

An analysis of dependency of V_{eff} and A_{eff} on lateral dimensions (Fig. 6.1)of the specimens confirms that slight, non significant differences between strengths of specimens L-6_4, and L-8_5 from different charges may not be due to higher sensitivity of certain designs to minor differences in dimensions, caused by variations in the trench process. The typical width deviation from the layout dimension, marked in the Fig. 6.1 with a vertical line, amounts to -0.48μm.

The resulting changes of A_{eff} and V_{eff}, in the range of few percents, would be rather small compared to 90% confidence interval error bars. The predicted difference of fracture strength between the two specimens with different effective volume/effective surface can be calculated using Eq.3.12.

The results for specimens L-06_3, L-08_4, L-09_3 and L-09_4 support this conclusions. Although the values of V_{eff} and A_{eff} differ in dependency on the structures width, no changes of fracture strength between specimens from both charges are observed.

Experimental results for the same kind of specimens originated from both charges (2004, 2005) have been pooled together and analyzed with a Weibull distribution. The pooled values are used in the following sections of the thesis.

The tendency that 'L'-structures with notch anchor type have higher fracture strength (Fig. 5.1) than specimens with smooth anchor type is also visible on the diagram in Fig. 5.3, which is presenting results of strength investigations for all types of 'L'-shaped specimens fabricated. In average the difference amounts to 18%.

In the case of specimens L-8_3 and L-11_3 (notch/smooth, other dimensions identical) the difference is very small. The opposite situation can be seen when comparing strengths of specimens L-7_5 and L-10_5. The difference between fracture strength of different specimens can be explained by the comparison of their V_{eff} and A_{eff}. The correlation between the effective size of the specimens and their fracture strength is presented in the Fig. 6.2.

The effective volume, V_{eff}, and the effective total surface, A_{eff}, have been calculated with the program STAU, by analysis of the spatial stress distribution given by the FEM simulations of stress distribution. The Weibull shape parameter was accepted to be 7.9.

Under the assumption of a constant defect distribution in the material the probability of the presence of a critical defect in the specimen increases with its size. Well known in literature as the 'size effect' [50,82,93]. It is clearly visible on this example.

The dependency between a specimen's size (V_{eff}, A_{eff}) and its fracture

(a)

(b)
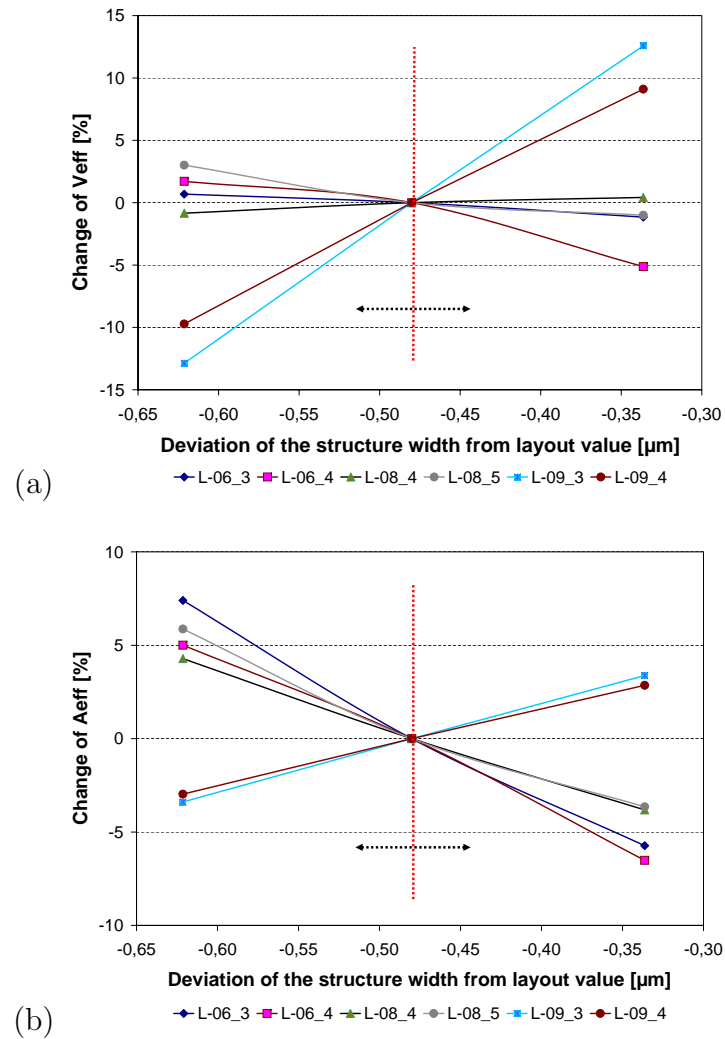
Figure 6.1: Sensitivity of the A_{eff} and V_{eff} of specimen on change of lateral dimensions (deviation of the width form a layout dimension)of the structure on example of 'L'-shaped specimens with notch and smooth anchor type
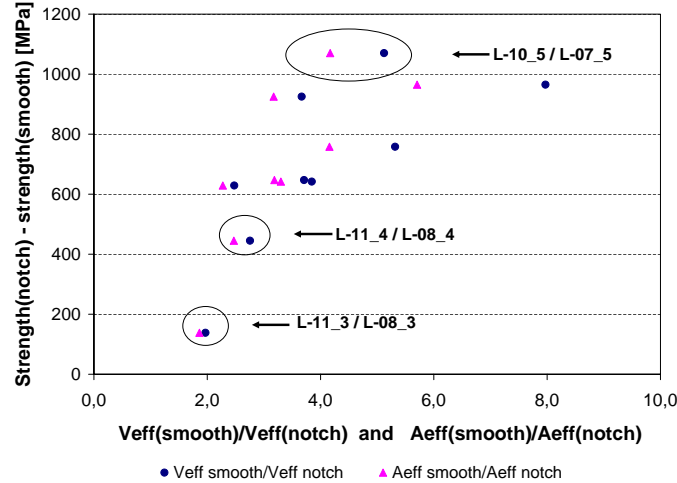
Figure 6.2: Difference between fracture stress of 'L'-shaped specimens with notch and smooth anchor type of the same dimensions in correlation with effective specimen's size ratio (V_{eff}, A_{eff})

strength is also clearly visible in Fig. 5.12, which is presenting results of 3-point-bending testing. Similarly, as in the case of 'L'-shaped specimens, the structures with the biggest effective volume and surface, (50μm width, 10μm thickness) are characterized with the lowest fracture strength and the specimens (4μm thick, 10μm width) with the smallest effective volume and effective surface show highest values of fracture strength. The specimens were processed in the same conditions and originate from the same wafer.

Influence of stress concentration elements e.g. notches, and the influence of holes on fracture strength of tensile specimens has been often discussed in the literature [123, 124, 44, 43, 92].

Results of the measurements performed on tensile test specimens with stress concentration elements are summarized in Fig. 5.10. The results achieved within this work are consistent with effects described in literature. A straight tensile specimen with width of 5μm and length of 250μm shows much lower fracture strength, than 20μm width tensile specimen of the same length with a circular notch or a central hole of radius of 3μm. Due to the stress concentration elements integrated in the structure the stress distribution undergoes substantial changes, and the effective volume or surface decrease distinctly.

Many authors investigated the size effect in polysilicon based on straight tensile specimens. The tendency in decrease of the fracture strength with increasing specimen's size was also observed [123, 124, 44, 43].

Measurements on straight tensile specimens with width of 5μm and various lengths in the range from 100 to 1000μm were expected to confirm a tendency of decrease of fracture strength with increasing size of the specimen. The experiment acted opposite to what was expected indicating a slight growth of fracture strength with increasing size of the specimen (Fig. 5.11). The application of Weibull theory

and prediction of strength of tensile specimens, seen in the Fig. 5.11, by comparing dimensions is possible only under the assumption that all specimens have uniform stress distribution in the whole gage section during test(Fig. 4.9).

The discrepancy between observed and expected behavior is explained with incorrect alignment of the structure and the loading tip. The incorrect loading direction results in essential changes of stress distribution due to parasitic bending moments. The explanation can be supported with results of the fracture analysis presented in Fig. 6.3.
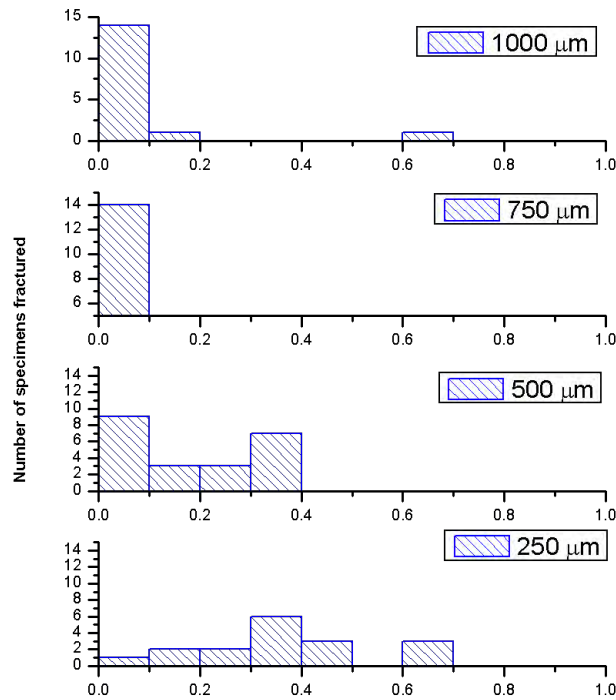
Figure 6.3: Distribution of fracture positions in straight tensile specimens with length from 250 to 1000μm and a constant width of 5μm

In the case of ideal tensile loading the random distribution of fracture positions would be expected. Nevertheless the specimens fail within the first 50-100μm measured from the anchor of the beam, independently on the total length of the beam. Fracture positions for tensile specimens with different lengths, except the 250μm long specimen, indicate on rather non uniform stress distribution in the beams. The incorrect force adjustment resulting in in-plane as well as out-of-plane parasitic bending moments in the structure, might result in similar fracture behavior.

The importance of the correct adjustment of the straight tensile specimen has been often discussed in literature [67, 70, 78, 84, 52, 76]. Very often measurements on tensile specimens are performed with a special micromanipulator, of high stiff-

ness, in the chamber of the Scanning Electron Microscope [67] . The alignment of the specimens can then be more precisely controlled.

Measurement setup used in this work seems not to allow sufficient alignment control of fragile 5μm width tensile specimens. The achieved results of the measurements of 5μm wide tensile specimens seem not to be reliable and their exact values will not be compared with any other results in further analysis, eventhough the fracture strength of approximately 2GPa is consistent with the size effect predictions based on strength and size of 'L'-shaped specimens.

According to Weibull theory, the fracture strength of 20μm polysilicon 'L'-shaped specimens is expected to be lower in comparison to 10μm layers. The results of measurements on 20μm thick 'L'-shaped specimens are shown in Fig. 5.9. Fracture strength of the thicker layers is of 14-21% lower in comparison to the 10μm thick specimens.

Sample	Samples tested	Characteristic strength σ [MPa]	Weibull coefficient m [-]	V_{eff} (μm³)	σ_{0V} (MPa $\times \mu$m$^{3/m}$)	A_{eff} (μm²)	σ_{0A} (MPa $\times \mu$m$^{2/m}$)
Tensile holed specimen	38	4398 (4257 - 4541)	8.8 (6.9 - 10.5)	0.74	4234	6.79	5605
Tensile notched specimen	38	4102 (3990 - 4216)	10.3 (8.1 - 12.4)	1.16	4180	8.36	5367
L-Structure 6_3 (10μm)	46	4869 (4709 - 5034)	7.7 (6.1 - 9.1)	0.089	3583	2.74	5532
L-Structure 6_4 (10μm)	44	4630 (4460 – 4805)	7.1 (5.6 – 8.3)	0.12	3542	2.89	5295
L-Structure 6_5 (10μm)	47	4764 (4583 - 4950)	6.6 (5.3 – 7.7)	0.14	3708	2.88	5446
L-Structure 9_3 (10μm)	47	4222 (4107 – 4340)	9.2 (7.4 – 10.8)	0.33	3668	8.73	5554
L-Structure 9_4 (10μm)	52	3872 (3758 – 3989)	8.0 (6.5 – 9.4)	0.64	3658	12.0	5303
L-Structure 9_5 (10μm)	51	3799 (3681 – 3921)	7.6 (6.2 – 8.9)	1.10	3846	16.4	5414
Three point bending specimen	21	4527 (4215-4860)	5.6 (3.9-7.0)	0.33	4027	7.22	5814
L-Structure 6_3 (20μm)	29	3806 (3654-3963)	8.1 (6.1-10.0)	0.17	3686	5.19	5683
L-Structure 9_3 (20μm)	24	3638 (3475-3807)	8.1 (5.8-10.0)	0.68	3463	17.67	5233

Figure 6.4: Weibull parameter for strength, Weibull coefficient, effective volumes/ areas and scale parameters calculated for the parameter value m= 7.9

Results of the measurements presented in this thesis reveal a dependency of fracture strength on a specimen's effective surface or volume. According to Eq. 3.13, a theoretical dependency can be presented to be linear with a slope σ_{V0} or σ_{A0} being a constant for the material under investigation.

In Fig.6.5 the characteristic fracture strength of all specimens tested, excluding the straight tensile specimen, has been plotted against effective surface/effective volume, calculated with STAU for 'm' value of 7.9. The strength
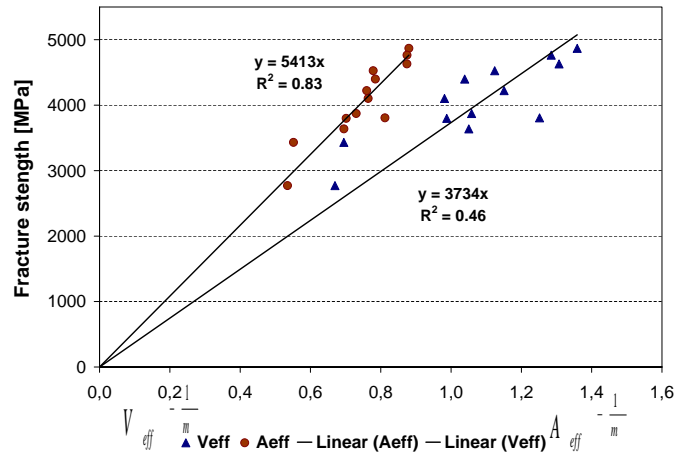
Figure 6.5: Linear dependency of Weibull fracture strength on specimen's effective surface/volume (see Eq. 3.13). Effective surface (A_{eff}) and effective volume (V_{eff}) have been calculated for m=7.9
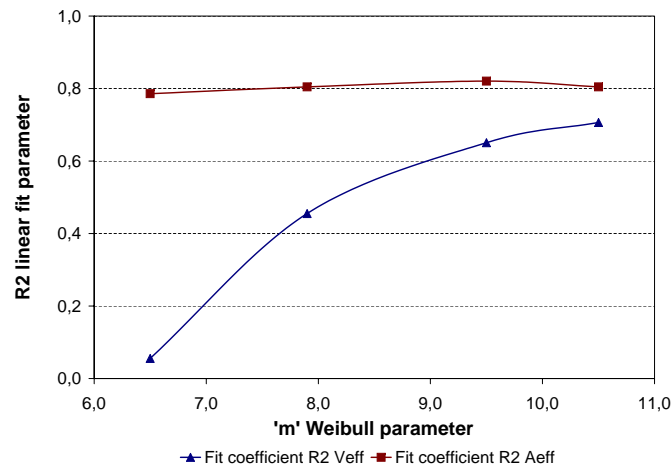
Figure 6.6: Goodness of correlation between fracture strength and effective surface/volume calculated with assumption of different value of Weibull 'm' parameter

of specimens seems to be better correlated with an effective surface than with an effective volume. The fit coefficient of determination, R^2, calculated for m=7.9 is 0.83 and 0.46 for effective surface and volume, respectively.

The fracture strength of specimens tested shows significantly better correlation with effective surface calculated for a wide range of 'm' values - Fig. 6.6.

6.1.1 Application of statistic methods based on the size effect in strength prediction

The mechanical properties of polycrystalline materials are strictly related to the structure and chemical/phase composition of the material. In addition, the shape

and size of the specimen strongly influence the strength properties, making the comparison of the results obtained for different test specimens difficult. Taking into account the difference in size and geometry, and size effect, one can predict the fracture strength of different specimens using the statistical method based on the weakest-link theory described in the Chapter Fundamentals.

In order to evaluate the applicability of the presented method for prediction of fracture strength of polysilicon components, the calculations have been performed for a representative group of specimens chosen out of all the specimens tested (see Table 1).

The effective volume and analogous effective surface, described by Eq. 3.9, depend on the Weibull parameter 'm', which describes the flaw distribution characteristic for the material.

Fig. 6.7 presents example values of V_{eff} and A_{eff} calculated for one of 'L' shaped test specimen and the different 'm' values. The fit line between points serves for convenient approximate interpolation between points calculated and is not based on any physical model.

(a)   (b)
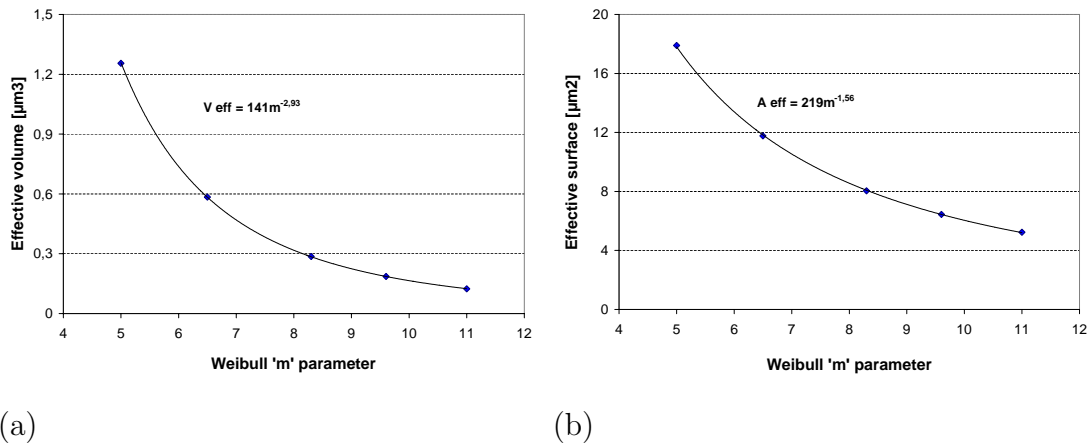
Figure 6.7: Dependency of V_{eff} and A_{eff} on the Weibull 'm' parameter; Example calculated for a 3μm wide 'L' structure. The best power fit is also presented on the plot

The accuracy of the strength prediction depends on the precision of the strength measurements of the basis geometry, the 'm' parameter taken for calculation, and the mechanical fracture criteria accepted for the statistical analysis.

Prior to predicting the fracture strength of a novel design, one needs to perform preliminary strength measurements on some other specimen build from the same material, with the same defect types and distribution.

As a basis for the first example prediction the specimen L-9_5 (smooth, 5μm width) (Fig. 6.4) has been chosen. Based on the data for the basis structure and V_{eff}, A_{eff} of other specimens, using Eq. 3.12 the predicted characteristic fracture strength of all other geometries have been calculated.

In order to estimate an accuracy of the method, predicted values have been compared with characteristic fracture strengths resulting from the experiments.

It should be noted that the characteristic fracture strengths of the basis specimen, as well as of the predicted sample, are described by the Weibull distribution with an error of approximately $\pm 3\%$. An error of the prediction, is calculated based on the error of the fracture strength measurements presented as 90% confidence intervals calculated for the Weibull strength distribution of the sample being the basis for the prediction and error of the 'm' parameter estimation assumed to be 2 (typical value of 90% confidence intervals for estimation of Weibull 'm').

The measured strength value for a predicted specimen also has an error expressed with confidence intervals. The accuracy of the prediction is calculated as a deviation of predicted values from measured values, expressed in percent. The error bars of the prediction are calculated as a difference between the lower error bar of the measured strength for a predicted specimen and the upper error bar of the predicted value. In a similar manner the upper error bar is calculated as a difference between the upper error bar of the measured specimen and the lowest predicted value (predicted value minus uncertainty of the prediction). Results of those calculations are expressed in percent. The basis for the calculation of percent is always the corresponding measured value of the predicted specimen. Presented average errors are equal to the mean value of all error intervals presented on the plot, for the plus and minus, respectively.

The accuracy of the predictions, based on effective surface and effective volume, are -0.8% and -4.6% respectively. The difference between positive and negative mean error of the prediction based on V_{eff} is bigger than for A_{eff} and reaches 24%, see Fig. 6.8 .

A similar procedure has been repeated 11 times, every time a different sample was taken as a basis for the strength prediction of all other structures. The fracture strengths of all other samples have been predicted for each investigated structure that was taken as a basis. The results are presented in Fig. 6.9 . Every point on the plot represents the average accuracy of the prediction of all samples based on certain geometry, with related average error values.

The average accuracy of strength prediction based on Aeff for the given set of specimens is approximately -0.3% (+9.8%, -10.7%), average accuracy of prediction based on effective volume is approximately -0.9 (+13.4%, -14.5%).

Similar procedure has been applied for Weibull 'm' values in the range from 6 to 11. The errors of the prediction have been estimated, and are presented in Fig. 6.10. The average accumulated accuracy for predictions based on surface and volume flaws show similar values in the range of 0-2%. The dependency of the error value on the 'm' parameter is observable. The dependency is much stronger for the calculations based on the assumption that volume flaws are responsible for the fracture under given stress conditions.

(a)

(b)
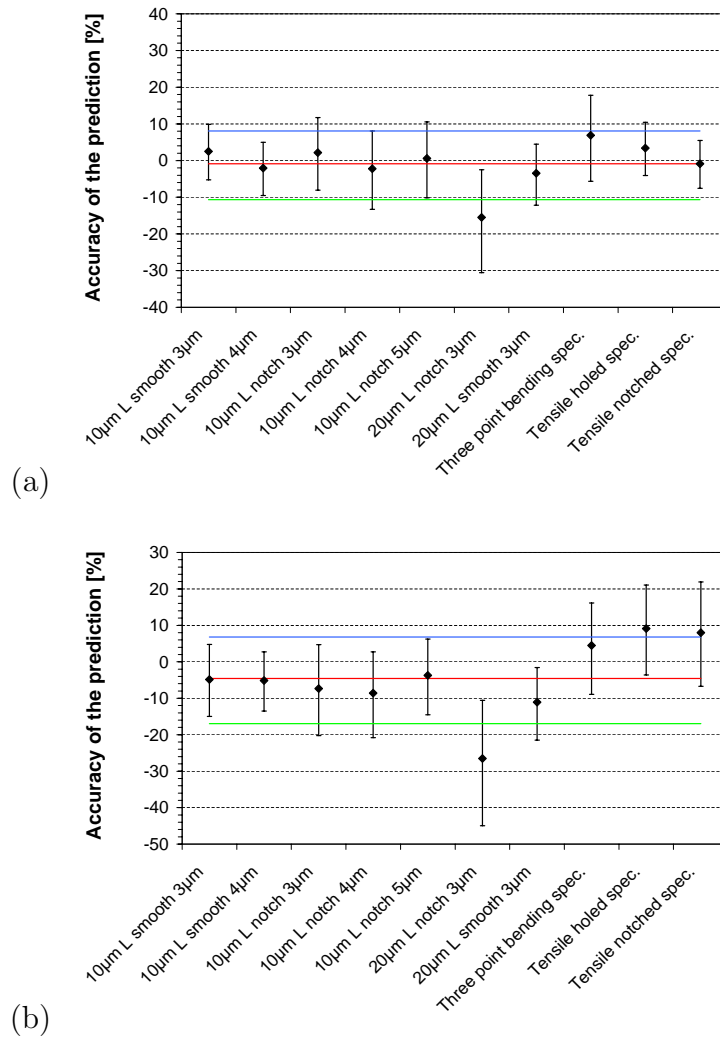
Figure 6.8: Prediction of the characteristic fracture strength based on the results for the 'L'-Structure (smooth 5μm); a) prediction based on effective surface b) prediction based on effective volume

(a)

(b)
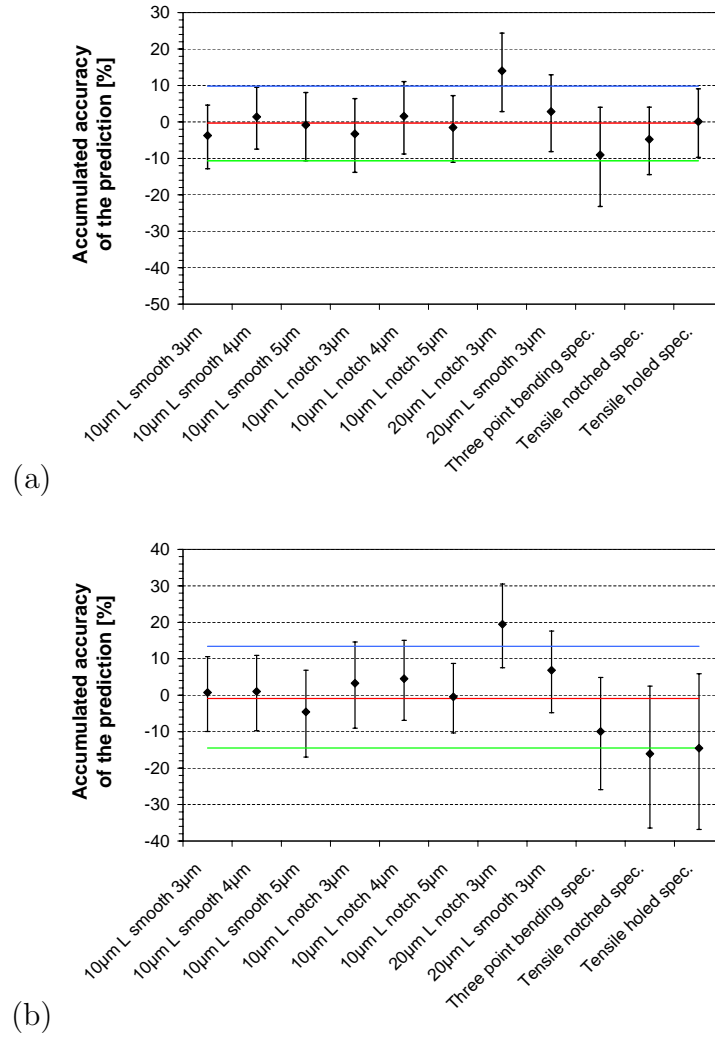
Figure 6.9: Accumulated accuracy of the prediction of the characteristic fracture strength based on effective surface for all results performed using the Richard Fracture Criterion; a) prediction based on effective surface b)prediction based on effective volume
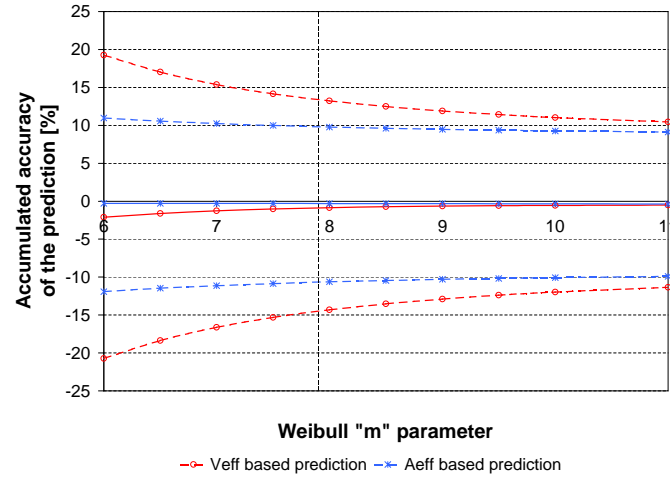
Figure 6.10: Accumulated accuracy of the prediction of the characteristic fracture strength based on effective surface and effective volume for all results performed using the Richard Fracture Criterion in dependency of Weibull 'm' value

Data presented in the Fig. 6.10 is consistent with the results presented in the Fig. 6.6.

Correlation between fracture strength and effective surface is much better than correlation between fracture strength and effective volume in the whole range of 'm' investigated. The mean accuracy of the prediction depends on the set of specimens investigated. Also values of mean positive and negative errors can not be used as absolute values characterizing the prediction method. The deviation of some certain specimens may be due to measurement error of the reference strength value and differences in defect distributions between the predicted and a prediction base specimen.

The accuracy of the prediction of the fracture strength presented in the Fig. 6.9, for 20μm thick, 3μm wide, 'L'-shaped specimens with smooth anchor type, was very good (range of a few percent) and similarly for most of 10μm thick specimens. Unexpected deviation was observed in the case of the 'L'-shaped specimen of the same dimensions with notch anchor type. The deviation of predicted value of approximately 20% from measured fracture strength, indicates that specimens seem to be unusually weak. The observation is consistent with the results of comparison of 'L'-shaped specimens of the same planar dimensions and different thicknesses presented in the Fig. 5.9. Both chip designs were placed on the same wafer in a random way, that excludes the selective negative influence of process parameters on the fracture strength. Probable explanation could be slight mechanical damage of the specimens during handling, described in section 5.1.1.

Nevertheless the use of statistical methods offers a time efficient method of strength estimation, with a relatively good accuracy of a few percent. Comparison of accuracies of prediction performed with the assumption that critical defects are placed on the surface of the specimens (prediction based on effective surface)

or in the volume of the specimen (effective volume) might help in identification of critical defect types responsible for the fracture. Implementation of statistical methods based on size effect in the process of development, optimization or reliability analysis of functional structures fabricated from brittle materials may shorten development time by reducing prototyping expenses and contributing to a better quality of the final product.

6.1.2 Critical defects in polysilicon - comment on fracture mechanism

There are various defect types in polycrystalline materials that may be responsible for the fracture. Many authors have led detailed discussions whether surface or volume defects are responsible for fracture. Different numerical simulations and fractography methods have been used in order to clarify this interesting issue [70, 50, 80, 28].

Based on statistical analysis and weakest link theory, similar to Tsuchiya and Bagdahn [92, 70, 89], the author of this work observed a much better correlation between fracture strength and the effective surface of the specimens. However it cannot be excluded that volume voids, in some cases, play the role of the weakest-link.

All single fracture stress values, for all specimens tested, with the exception of straight tensile test specimens without stress concentration elements, were normalized with effective surface/effective volume and then analysed with a Weibull distribution. Fig. 6.11 shows that all points cannot be fit with one straight line. In total, the measurement results for more than 850 specimens of different size and geometry are presented in the Fig. 6.11.

A similar tendency was already observed in Fig. 5.1 where few lowest fracture stress values deviated from the fit line representing the Weibull distribution.

Results presented in Fig. 6.11 may be described as the sum of two distributions with different Weibull scale parameters. This indicates on the existence of two types of defects responsible for fracture [125]. Slope of the curve suggests that smaller defects are more widely distributed than bigger defects, leading to fracture under relatively low stress values. It should be mentioned that even the lowest stress values measured are far above the highest mechanical stress to be expected in serial Bosch MEMS applications.

In order to understand the influence of surface quality on the fracture strength of the specimens, and evaluate the severity of surface defects, a series of tests on 10μm thick 'L'-shaped specimens with modified side surface were conducted. The deposition conditions influencing volume defects were kept constant within the process tolerance. A summary of results is presented in Fig. 5.8.

The results for specimens fabricated with different trench process parameters show the influence of side wall roughness on the fracture strength of specimens.
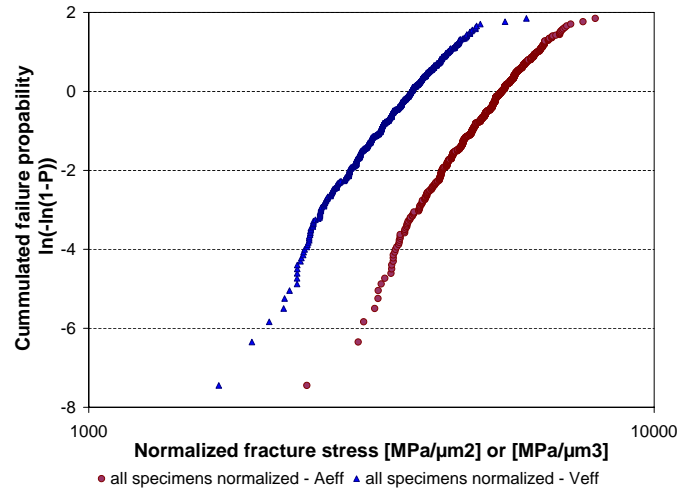
Figure 6.11: Values of fracture stress for all tested specimens with the exception of straight tensile test specimens without stress concentration elements normalized with effective surface/volume

Typically the side walls of $10\mu m$ thick polysilicon layers are structured in approximately 28 etching - passivation cycles ('Standard'). Structures of the same thickness fabricated in modified conditions 'Trench param.' were trenched in 20 cycles which, under isotropic etching conditions, which result with deeper etching graves and higher roughness. The fracture strength of all specimens fabricated in these conditions is substantially lower than of a reference wafer fabricated with the standard process conditions ('Standard').

Consistent observations were made for $10\mu m$, 3-point-bending specimens, fabricated with different trench programs resulting in different surface roughness of the loaded area - Fig. 5.13. Specimens with higher roughness had lower fracture strength than specimens with a lower roughness.

Results of roughness measurements on trenched side walls of epitaxial polysilicon with columnar grain structure, depend strongly on the measurement position - Fig. 5.28. For specimens trenched in standard conditions the lowest roughness (approximately 14nm) is measured close to the bottom of the specimens where the smallest crystals in the structure can be found. The highest values (approximately 26nm) are usually measured close to the upper edge of the specimen. Also, the standard deviation calculated for roughness values measured close to the upper side is significantly higher than for measurements performed close to bottom side of the specimens. The inhomogeneity of the crystal structure on the side wall can be seen in Fig. 6.12.

For twenty selected 'L'-shaped specimens, the fracture strength has been correlated with the mean side wall roughness. Fig. 5.29 shows a light tendency indicating lower strength values for specimens with higher roughness. The presented correlation, consistent with literature, confirms the conclusions from statistical strength prediction, that the weakest link defects responsible for fracture can be

(a)   (b)
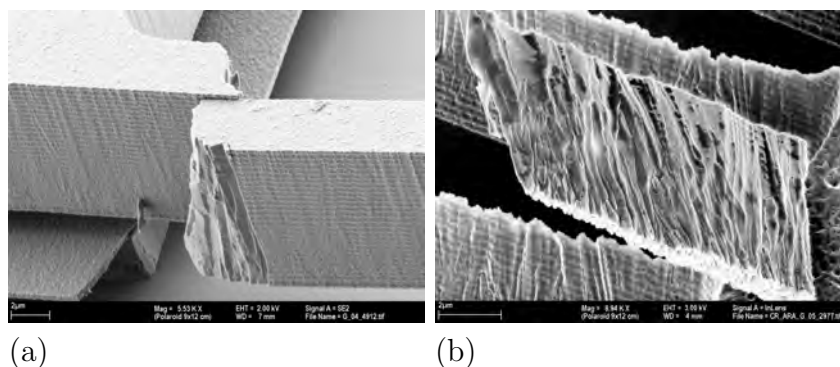
Figure 6.12: Inhomogeneity of the crystal structure of the side wall on example of 10μm thick 'L'-shaped specimen fabricated using standard trench process; a) side wall surface of as fabricated specimen b) specimen after 10s SECCO etching performed in order to decorate crystal structure

found on the surface of the specimen.

It has to be taken into account that measurement of the mean roughness does not picture the size of the biggest 'weakest-link' defects, but the mean value integrated over the scan length. The achieved correlation should be treated qualitatively. Direct calculation of the fracture stress using Grififth's equation Eq. 3.6 for a given critical defect size equal to the value of mean roughness, would certainly lead to an overestimation. In the area of uniformities (Fig. 6.12) there is locally stress greater than expected that could activate smaller voids and to cause fracture.

Yi et al. compared fracture strength of polysilicon structures fabricated using different etching chemistries. It has been concluded that not only the depth of surface defects (roughness), but also the shape of flaws is an important parameter influencing the strength of the material [126].

Light oxidation of the polysilicon side walls performed after etching seems to have a positive influence on the fracture strength of the material (Fig. 5.8, 'Ozone'). The change is probably due to a slight change of surface topography, leading to smoothing of predefined flaws present on the surface.

The improvement of fracture strength is mostly observed in the case of smooth 'L'-shaped specimens with high A_{eff}, which is consistent with the assumption that the change of the surface morphology was the reason for higher fracture strength of the specimens.

Longer oxygen plasma striping typically used to remove unwanted residues would also be expected to influence the topography of the side walls. Results of strength measurements on specimens ('Stripper') fabricated with extended stripping time are not significantly different than the reference. Lack of a significant difference is probably caused by too small changes in the topography of the surface resulting from too short time/power of the surface modification.

The confirmed lack of significant influence of temperature accompanying the

glass frit bonding process on fracture strength ('Temperature'), allows comparison of results of measurements conducted on both specimens open and closed with a protection cap.

An overview of observed fracture modes are presented in the Chapter Fracture analysis. In the most of cases the fracture origins seem to be placed on the side surface or edge of the specimen; in many cases just under the surface of the material. (Fig. 5.26, Fig. 5.30, Fig. 5.31.

Micrographs Fig. 5.26e, Fig. 5.30 and Fig. 5.33 indicate the existence of an autonomous structure covering the side walls of the polysilicon. Chemical analysis revealed the presence of chemical elements like carbon, oxygen and fluorine in the side layer, which were unaffected after SF_6 etching of the test specimens (Fig. 5.35). A plausible source of the carbon and fluorine can be the C_4F_8 polymer used for passivation of the side walls during the trench process. Oxygen could be introduced by the oxygen plasma stripping step applied in order to remove resist residues from the polysilicon surface. Introduction of fluorine with the etching medium SF_6 that could false the conclusions seems to be improbable because of lack of fluorine residues on the silicon surface in the middle of the specimen exposed to the SF_6 and high concentration in the 'side-layer' material. Presence of organic residues joined with external layers of polysilicon, creating a two-material interface ('composite'), may have an important influence on the fracture mechanism. The structurally weakest-links existing in the interface would have been difficult to detect by analysis of the surface of the material. The micrograph Fig. 5.26c could be a consistent example with the hypothesis proposed. The delamination visible could be the result of fracture propagation in the interface between the silicon volume structure and a side-wall layer. The surface of the silicon after the fracture is reasonably smooth, which can be an indication on delaminated layer compact structure and a relatively weak connection with the bulk.

Although the deposition of layers with different thicknesses was conducted in the same conditions, there are some structural differences between both materials. Since the crystals in 20μm thick polysilicon layers grow also in a columnar way, the longer deposition time results in a larger average size of the crystals and a lower share of the grain boundaries in the volume of the material. The fractography shows that an intergranular fracture accompanied with a crack branching was characteristic for 20μm thick polysilicon layers Fig. 5.32.

Longer and more intensive trench process was used for structuring of vertical walls of the 20μm thick polysilicon specimens. The roughness and a side-surface composition may also vary and influence the strength properties in the manner described above. The results of prediction for 20μm thick 'L'-shaped specimens with smooth anchor type, indicate on a similar defect distribution as in the case of 10μm thick specimens.

Based on fracture stress values, it is possible to calculate the critical size of the defect that caused the fracture. The conversion of measured fracture deflec-

tion/force into fracture stress was made using the first principal stress, calculated with FEM for a certain fracture deflection. As shown in Fig. 5.5 the specimens fracture is not always in the position with the highest first principal stress, but always in the place of a defect of critical size.

From the designers point of view, the maximum principal stress is a very important criterion, but in order to estimate the 'real' defect size the 'real' stress values at the fracture position, if possible to measure, should be taken into account.

Fig. 5.7 presents the comparison between the Weibull fracture strength calculated based on the first principal stress and the 'real' stress values.

As expected (constant defect distribution in the material) there is no significant difference between 'L'-shaped test specimens with a different anchor type. Both methods give similar results in the case of 'L'-shaped specimens with smooth anchor types where the stress is widely distributed on the surface of the specimen. Obviously the probability of coincidence of high stress value and the presence of the biggest flaws (severe defects) is much higher than in the case of 'L'-shaped specimens with high stress gradients (notch anchor). The stress distributions in both specimens are presented in Fig. 4.5.

Fig. 6.13 summarizes the defect size distribution for all 10μm thick specimens tested, as well as separately for 'L'-shaped specimens (Charge 2005). Fracture stress for series 'all 10μm thick specimens' as well as 'L-structures S1 - max' was calculated taking into account maximum principle stress in the specimen, calculated for the fracture deflection. For comparison, the 'real' fracture stress values for 'L'-shaped specimens (Charge 2005) have been presented. Critical defect size was calculated for $K_{Ic} = 0.85 MPa \cdot \sqrt{m}$.
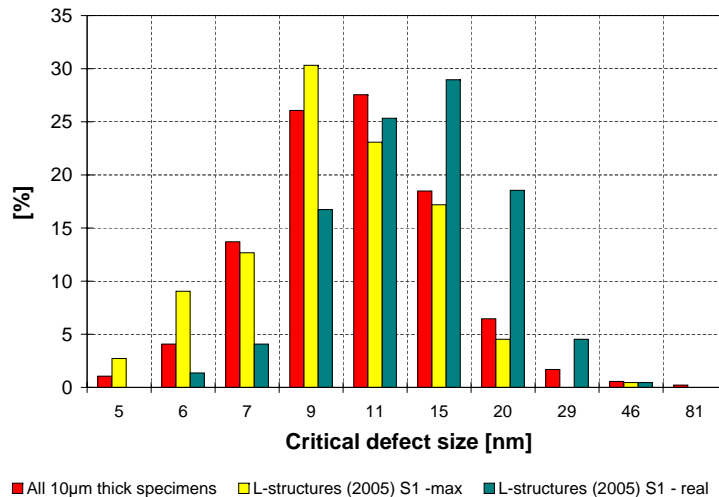
Figure 6.13: Histogram - critical defect size of 'L'-shaped specimens (Charge 2005). Fracture Defect size calculated based on maximum principal stress in the structure (S1 - max) and at the real position of fracture (S1 - real)

The biggest defects present in the material are approximately 80nm although the fracture of most of the specimens is caused by a defect of up to 15-20nm. This can be correlated with the roughness of the side walls. A light shift toward the higher size of defects is observable when the real fracture stress is concerned. The overall characteristic does not undergo substantial changes.

The fractographic analysis provided many arguments indicating surface originated fracture in polysilicon specimens. Additionally the author has presented an important influence of roughness, as well as the modification of the polysilicon side-layer in the trench process on the fracture strength of the components.

The interface between the volume of the material and the 'bulk', has been identified to be apart of surface defects created in the fabrication process a possible weakest-link in the material.

6.2 Fatigue and strengthening of polycrystalline silicon

Cyclic fatigue is the most commonly encountered mode of failure in structural materials occurring, in both ductile and brittle solids [127]. Silicon is a 'fully' brittle material at a room temperature. We thus would not expect silicon to display any time dependent cracking when subjected to monotonic or cyclic loading conditions. Experimental results, however, have shown otherwise [9].

The fatigue of silicon was first demonstrated in 1992 by Connally and Brown [95]. This surprising discovery led to many intensive investigations. Various fatigue mechanisms have been proposed [116,128]. The most important known from literature can be divided in two basic groups concerning a basic principle.

- **Environmentally induced crack growth in silicon oxide layers present on the surface of polysilicon**. A reaction layer mechanism of polysilicon fatigue proposed by Muhlstein et al. [107] involves sequential mechanically-induced oxidation and environmentally-induced cracking of the oxide layer on the silicon surface under cyclic loading. As reported by Pierron the reaction layer fatigue mechanism can be also applied to single crystal silicon [9].

- **Subcritical crack growth in polycrystalline silicon**. This mechanism, proposed by Kahn et al., states that a likely origin of the microcracks that undergo subcritical crack growth are the asperities on the notch surfaces, which can come into contact during the compressive cycles and which then act as wedges to create areas of local tension [119]. The crack growth rate was reported to be independent from environmental effects. The authors also explained a strengthening of silicon as a result of intrinsic compressive stresses caused in the compressive phases of loading.

The results achieved in this work will be compared with data reported in literature. The applicability of basic assumptions of existing fatigue mechanisms to Bosch polysilicon will be 'step-by-step' discussed in the following paragraphs(Fig. 6.14).

Reaction layer mechanism by Muhlstein	Subcritical crack growth mechanism by Kahn
•Change of resonance frequency of specimen resulting from environmental crack growth in thick oxide layers	•Subcritical crack growth under compressive stress.
•Formation of very thick (up to 100nm) oxide layers on silicon surface. Stress induced and chemical oxidation	•Strengthening caused by plastic deformation in material created under compressive stress

Figure 6.14: Basic ideas of reaction layer and subcritical crack growth mechanisms

Change of resonant frequency as a measure of crack growth

Muhlstein et al. and Van Arsdell et al. correlated a shift in resonant frequency of a rotation oscillator tested with changes in the silicon oxide thickness on the surface of the specimen and crack growth. The precise estimation of crack growth rates has been proposed [103, 107, 45].

The drop in resonant frequency was also observed in high-frequency fatigue investigations performed in this work. The drop in resonant frequency of the example specimen '4222' (Fig. 5.20 a)) within the first 40 minutes of operation (approximately 10^6 cycles), at a first glance seems to be consistent with observations reported by Muhlstein [45]. On the contrary the development of resonant frequency through the lifetime of specimen shown in Fig. 5.20 b) may not be explained by any theory based on crack growth.

Experimental observation (Fig. 5.22) suggested a significant influence of the temperature on the resonance frequency of rotational oscillators. In order to verify the hypothesis, an experiment under controlled temperature with the use of the micro-heater (Fig. 4.24) was conducted . Variation of the resonant frequency of the specimen that underwent cyclic temperature changes with an amplitude of 30°C (Fig. 5.23) are consistent with the experimental results.

Decrease of the resonant frequency of 40-60Hz at the beginning of the test, before the thermal balance in the system chip-device was achieved, can be explained by the temperature change of the Young's modulus of polysilicon. Known from the literature temperature dependency of the Young's modulus is presented in Fig. 6.15.

Adequate modal FE simulations were performed in order to estimate the frequency shift due to Young's modulus changes under a given range of temperature. Simulation results presented in Fig. 6.16 are consistent with experimental results and confirm that the observed changes in resonant frequency might have been caused by changes in the Young's modulus of polysilicon. The change of specimen's dimensions due to temperature change in the range of 20-60°C are not significant and have been neglected in the simulations.
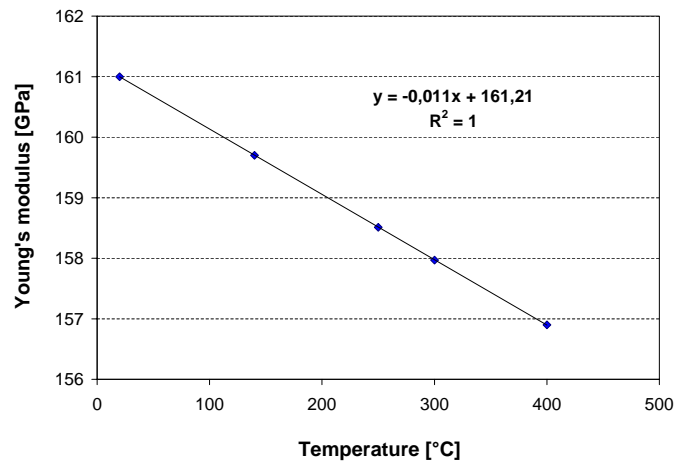
Figure 6.15: The temperature dependency of the Young's modulus of polysilicon
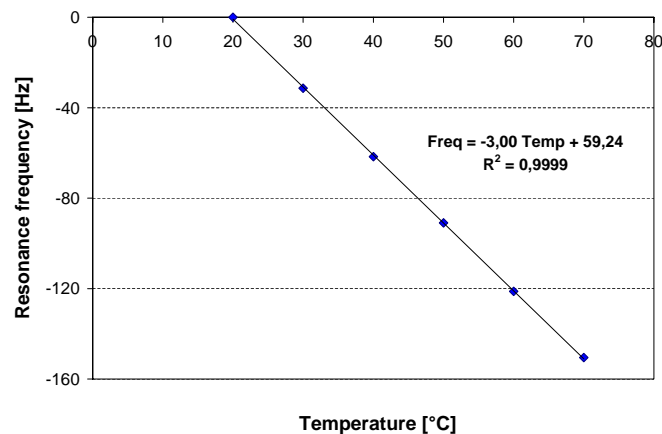
Figure 6.16: Temperature dependency of the resonant frequency of the rotational oscillator, resulting from changes in Young's modulus due to the temperature

Experiments in which Muhlstein [107] observed a frequency shift correlated with a crack growth have been conducted in a well defined atmosphere with temperatures controlled with an accuracy of ±0.1°C.

The test device used in this work allows parallel high-cycle testing of up to 16 specimens in one 19" rack. Due to frequent changes of number, position and

state (off/on) of measurement cards, the measurements have been conducted with variable temperature in the range of 30-60°C.

Even if Bosch polysilicon has similar fatigue characteristics to that analyzed by Muhlstein, the decrease of the resonant frequency resulting from crack growth would not have been clearly observed with the use of the testing system applied. This is due to the dominant influence of temperature on the resonant frequency.

In order to be able to observe a decrease of the resonant frequency due to crack growth, as proposed by Muhlstein, an experiment in which the specimen is oscillating in a resonance under controlled temperature cycles for the period of up to 72 hours was performed. That kind of experiment could help to separate the measurement 'noise' caused by the temperature deviation and the steady decrease of the resonance frequency due to crack growth in the specimen.

Fig. 5.23 presents the frequency development over the first 24 hours of oscillations. Experimental results did not show any significant decrease of the mean frequency over $2.3 \cdot 10^{10}$ cycles. This observation is inconsistent with the model reported by Muhlstein.

It can be concluded that a change of the resonant frequency of the rotational oscillators, observed in this work, cannot be analyzed as an indicator of crack growth.

Creation of a thick oxide layer and its environmental cracking

Polysilicon investigated by Muhlstein was covered by an oxide layer of thickness up to 100nm, which is invariably much more than usual thickness of native oxide. HVTEM measurements have revealed up to a three fold increase in oxide thickness at the root of the notch of the rotational oscillator. Also, a cracking of thick oxide resulting from cyclic mechanical loading was observed [107].

It has been lately proven that the thick oxide layers described by Muhlstein and Pierron are formed in manufacturing due to galvanic effect between between n+ type silicon and the pad's material, gold [129, 130, 131]. Such an oxidation mechanism can be excluded in standard Bosch fabrication processes.

Due to the lack of a notch in the structure investigated in this thesis, precise measurements of the oxide thickness change, due to oscillations at the well defined area of maximum stress are much more complex than in the case described by Muhlstein. Thickening of the oxide in the most stressed areas of the specimen even after 10^{12} cycles has not been observed. Unfortunately the presence of the silicon cap makes observation of material changes, e.g. cracking, caused by mechanical loading not possible. The state after the test may be only compared with typical properties of a new specimen.

Although high cycle measurements of rotational oscillators performed in this work have been conducted in low pressure atmosphere (2mbar) the presence of residue oxygen and water can not be excluded. In order to investigate the influence

of chemical silicon oxidation in the chip on the strength measured with the ramp-up test, 32 new specimens were conditioned at 150°C for 750h before the test. The chemical oxidation in the hot oven is significantly faster than at temperature below 60°C during the short time of the test. No influence of chemical oxidation of the material surface with corrosive residues present in the chip on the fracture strength as well as on Weibull 'm' parameter has been observed. The specimens were covered with the oxide thickness close to the maximum that can be achieved by thermal oxidation in the atmosphere of the package in maximum temperature of a typical MEMS application in automotive industry.

It is important to note that the details of processing can have a profound impact on the composition and structure of the surface of micromachined components. Given the critical role of surface in the damage accumulation process, the intricate coupling of environment, stress, and degradation may be altered by seemingly minor changes to processing or handling conditions [9]. It has been demonstrated by Pierron et al. that deposition of organic surface films on specimens could suppress the fatigue process, probably due to affecting the ability of water and oxygen to participate in the fatigue process. Consequently, modifications to the trenching process, that alters the surface structure of the material and can leave polytetrafluoroethylene (PTFE)-like passivation on the surface, could lead to significant variations in fatigue resistance [110].

The organic residues after the passivation process are also present on the side walls of Bosch test specimens, and may suppress possible oxidation of the surface. The micrograph of side wall surface is presented in Fig. 6.17.
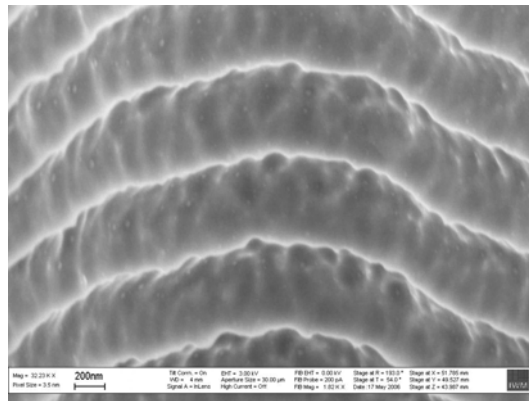
Figure 6.17: Scanning Electron micrograph of sidewall of resonant oscillator used in fatigue testing at Bosch. Side walls are covered by organic residues after passivation in the trenching process

Fig. 6.18 presents a failure map for a silicon thin film, with an oxide surface layer of thickness h, as proposed by Pierron [132]. Pierron et al. claim that a 15nm thick oxide layer can already activate reaction layer fatigue mechanisms for a polycrystalline silicon thin film under a stress of approximately 5GPa. The
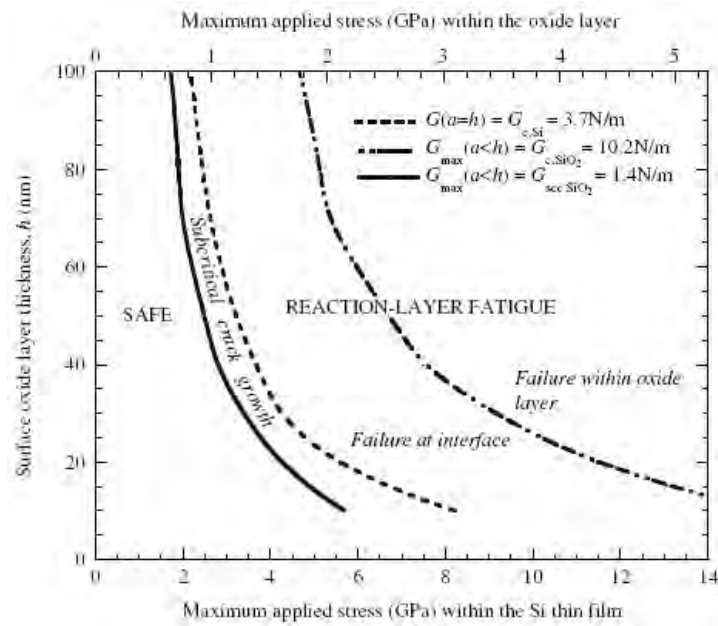
Figure 6.18: Failure map for a silicon thin film with an oxide surface layer of thickness h [132]

thickness of **native** silicon oxide layers of Bosch polysilicon is not sufficient for a crack to achieve its critical size under a stress as low as 3.5GPa (Fig. 6.21).

Kahn et al. [117] have also shown that polysilicon devices with thick (thermally grown) oxides of 45nm are susceptible to delayed failure when subjected to monotonic tensile loads in humid air, presumably due to stress corrosion on the surface oxide. Identical devices with thin native oxides of 2nm do not undergo delayed failure [116].

Native oxide layer thicker than a few nanometers have never been observed on the surface of the specimens investigated. Due to the low oxide thickness on the surface of Bosch polysilicon, the basic condition for a reaction layer fatigue mechanism by Muhlstein is not fulfilled.

Subcritical crack growth under compressive stress and strengthening in polysilicon

Testing of rotation oscillators fabricated from Bosch polysilicon revealed a decrease of mechanical strength under high frequency cyclic loading under a low pressure of 2 mbar. The results of fatigue investigations of rotational oscillators fabricated from layers with thickness of 10 and 20μm are presented in Fig. 5.19.

A considerable difference between static measured fracture strength of specimens and the results of the ramp-up test is visible for both polysilicon layers (Fig. 5.19).

The lower fracture strength of the ramp-up test compared to static measure-

ments would be expected even in the case of a lack of fatigue behavior under cyclic loading. During monotonic strength testing only one side of the oscillator beam is exposed to high tensile stress. Alternate loading of both sides of the oscillator beam during the ramp-up test extends the population of material flaws under stress (effective area, effective volume) and should theoretically lead to a decrease in fracture strength. A decrease of fracture strength resulting from doubling of effective area/volume should be approximately 10%. For both, 10 and 20μm thick polysilicon layers, the decrease is significantly higher, which could be explained with fatigue under cyclic loading.

Investigations by Kahn et al. on 5.7μm thick LPCVD polysilicon, reported a decrease of the fracture strength in cyclic loading stress, with finite mean stress σ_m and ramped amplitude $\Delta\sigma$ Fig. 6.19 [119].
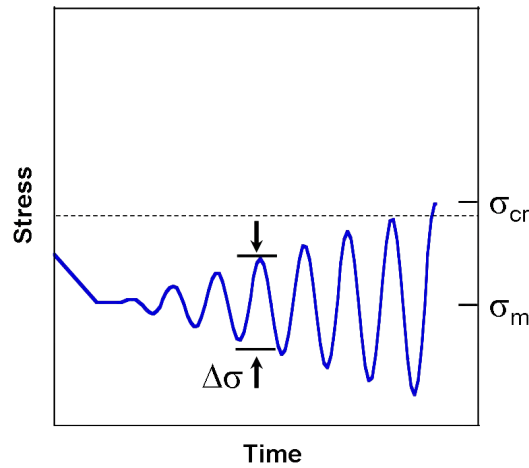
Figure 6.19: Schematic representation of stress seen in cyclic loading test by Kahn [119] with finite mean stress σ_m and ramped amplitude, $\Delta\sigma$

The test by Kahn was performed in a similar manner to the ramp-up test in this work and lasted approximately 1 minute. The specimens fabricated from B-doped and undoped polysilicon oscillated with resonant frequency of 10 kHz. Results are presented in Fig. 6.20. Results for $\sigma_m = 0$ can be directly compared to the results of the ramp-up test performed in this work.

Kahn et al. observed a decrease of the fracture strength of up to 25% after approximately 1 minute of oscillations with an increasing mechanical amplitude. Measurements performed in air (10^5Pa) and vacuum (10 Pa) had shown an identical tendency, indicating that the fatigue mechanism is not dependent on atmospheric influences e.g. humidity or the presence of other reagents supporting corrosion of the silicon surface [3]. Kahn postulated that the decrease of strength with increasing number of cycles can be explained by the influence of the compressive stress on the material.

Under the assumption that the length of a surface crack is more than three
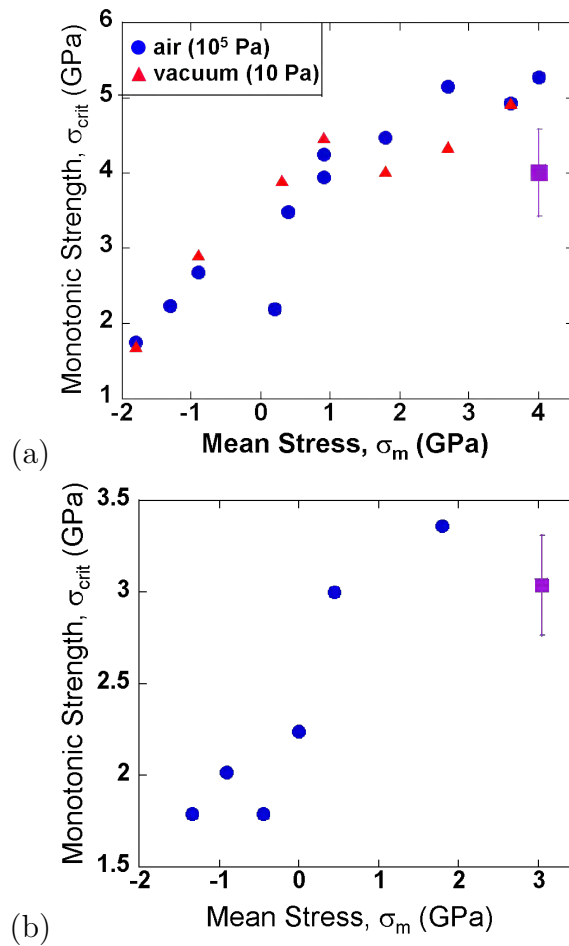
Figure 6.20: Results of increasing fatigue test of polysilicon in air (circles) and in vacuum (triangles). a) Data for Pd-coated undoped polysilicon; b) data for B-doped polysilicon with no Pd. In each plot the monotonic strength, taken from specimens that saw no cycling, is shown as the solid square; the square marks the average strength, and the error bars represent one standard deviation [3]

times the depth of the flaw, the critical defect size may be estimated using the Eq. 3.6 [9]:

$$a = \left(\frac{K_I}{1.12\sigma\sqrt{\pi}} \right)^2$$
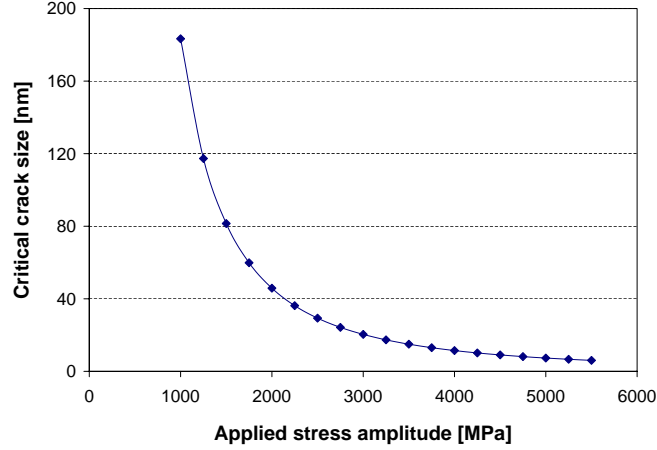
Figure 6.21: Critical defects size as a function of applied stress amplitude. Calculation based on assumption $K_{Ic} = 0.85 MPa\sqrt{m}$

The dependency between fracture strength and critical defect size calculated for $K_{Ic} = 0.85 MPa\sqrt{m}$ is presented in Fig. 6.21.

For 20μm thick specimens the average critical defect size measured in a monotonic test was 9nm (range 7-18nm). The average defect size measured in a ramp-up test was 27nm (range 22-37nm). The significant growth of the defect size within the less that one minute of the ramp-up testing was observed. The 20μm thick specimens failed after as many as 10^{10} cycles under a mechanical stress of 2500 MPa. This suggests the presence defects of 30nm size in all specimens.

The average defect's critical size, for 10μm thick polysilicon, calculated based on the results of monotonic strength testing, was 7nm (range 5-8nm). Average critical defect size estimated based on the results of ramp-up testing was 14nm (range 9-28). Crack growth rate in 20μm thick polysilicon seems to be two-fold higher in comparison to 10μm thick layers.

Specimens fabricated out of 10μm thick Bosch polysilicon have shown fatigue fracture under cyclic load of 3500 MPa. Defects of approximately 15nm in size did lead the specimens to fracture.

Critical defect size in 10μm thick polysilicon measured in ramp-up testing of 25 specimens, was in the range of 9-28nm. It could explain sudden failures of certain specimens at the beginning of high-cycle testing with a constant amplitude of 3500 MPa.

None of the 45 specimens driven with a mechanical amplitude of under 3000 MPa failed within $1.6 \cdot 10^{11}$ cycles. This suggests that no defects above 20nm

size were present in the specimen's area of maximum mechanical stress. This surprising result seems not to be consistent with results of ramp-up testing, that proved the presence of defects of 22 - 28nm size that should cause a catastrophic fracture under a mechanic load as low as 2560 MPa. This result indicates the existence of a strengthening mechanism in the material.

The fracture strength of 45 10μm thick polysilicon specimens that did not fracture within $1.6 \cdot 10^{11}$ cycles were measured with the use of the ramp-up test as describe in Chapter 5.2.1.3. Measurements shown that the residual strength of the specimens after more than 10^{11} cycles is higher than that of new specimens measured with the same method. Similar measurements have been performed for various mechanical amplitudes in the range of 660 - 3000 MPa. All results are presented in Fig. 5.25.

The strengthening of up to 20% of ramp-up fracture strength has been measured. Significant influence of the number of cycles on strengthening rate has been observed. Reports of Kahn et al. who also observed strengthening of polycrystalline silicon can be found in literature [119]. Kahn proposed a mechanism assuming grain boundary plasticity and explained the strengthening as a result of local residual compressive stress [3].

In order to verify the applicability of the strengthening theory of Kahn, the presence of intrinsic compressive stress in the most loaded 'side-layer' of the specimens was investigated.

The influence of cyclic loading on intrinsic stress in the 'side-layer' was evaluated by the slow gradual FIB removal of the side-wall on one side of oscillator's beam structure and observation of the seismic mass movement (Fig. 6.22). The principle of the investigation is schematically presented in Fig. 6.23.

If there is any residual compressive stress available in the beam, removal of only one side of the side-layer should result in movement of the seismic mass driven by unbalanced compressive stress. The correlation between the residual width of the beam and movement of the seismic mass would differ for new specimens and those with a history of cyclic loading.

Comparison of the seismic mass movements of both investigated specimens (new specimen and the specimen with a history of cycling loading) does not show any significant change of intrinsic stress in the side-wall layer as a result of the cyclic loading (Fig. 6.24). Compressive stresses in the range of 700MPa would be expected to cause a significant movement of the seismic mass.

The presented experimental results show that the strengthening observed in Bosch polysilicon can not be explained, as proposed by Kahn, with residual compressive stress resulting from grain boundary plasticity.
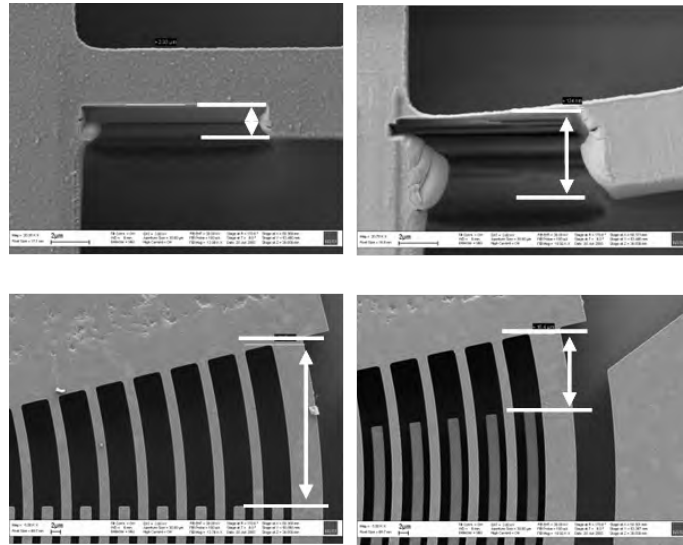
Figure 6.22: Estimation of compressive stress in the side-layer of the rotational oscillator. Gradual FIB thinning of material results in the movement of the seismic mass driven by not balanced set of forces. Upper micrographs present the rest width of the beam tested, resulting position change of the seismic mass can be seen on the down micrographs
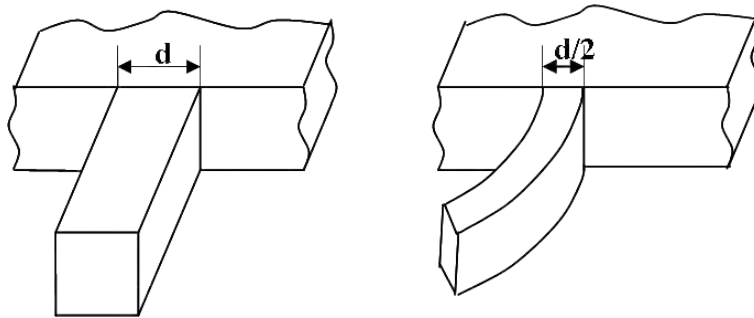
Figure 6.23: Schematic of of compressive stress estimation in the side-layer of the rotational oscillator. Gradual FIB thinning of material results in the movement of the seismic mass driven by not balanced set of forces

Fatigue mechanism of Bosch polysilicon

Previously the applicability of basic ideas of known fatigue mechanisms to experimental results with Bosch polysilicon was discussed.

An observed decrease of strength of Bosch polysilicon under mechanical loading with amplitudes higher than 3000MPa for 10μm and 2500MPa for 20μm thick specimens in the low pressure atmosphere (2mbar) may not be explained by cracking of the thick oxide layers on the silicon surface.

Additionally the shift in the resonance frequency measured with testing setup used in this investigations cannot be correlated with crack growth as proposed by Muhlstein [9]. This is consistent with the opinion of Pierron et al. [132] who
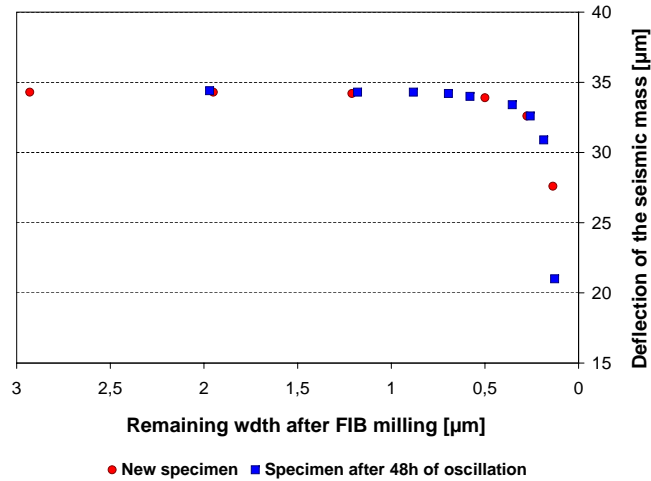
Figure 6.24: Investigation on influence of a cyclic load on the compressive stress in the side-wall layer of a rotational oscillator. Results for a new samples have been compared with results for specimen after 48h oscillations with amplitude of 3500MPa

reported the applicability of the reaction layer mechanism for significantly higher oxide thickness than was measured on specimens tested in this work.

Bagdahn et al. reported [128] that the fatigue lifetime depends only on the number of cycles, not on the total time of the frequency of the test. This basically excludes chemical process such as oxidation as a explanation for the material changes.

The fatigue and strengthening mechanism by Kahn et al. that assumes the existence of residual compressive stress in the beam, also cannot explain the behavior of Bosch polysilicon. Investigations show a lack of compressive stresses in the beam that could be responsible for the strengthening of up to 700MPa.

The observations by Kahn and the results presented in this thesis show significant strength degradation within the first minute of the test or comparable results for specimens tested in a vacuum and laboratory conditions (Fig. 6.20) that are in contrary to mechanism proposed by Muhlstein. The strengthening during the ramp-up test cannot be explained with the reaction layer mechanism.

Similarly, like Pierron proposed in his work [9] judging by the appearance of the fracture surfaces of Bosch specimens, author doubts that microcracking could be the cause of strength degradation as proposed by Kahn [3].

The ramp-up test performed in this work has shown faster decrease of fracture strength for 20μm thick specimens. Similar decrease for both layers (10μm, 20μm) would be expected if we apply the model reported by Bagdahn [128].

Concerning the fatigue mechanism of polysilicon, there is no agreement in literature yet.

Observations of strengthening of up to 20% of fracture strenght, no degradation up to 10^{11} for mechanical amplitudes up to 3000MPa for 10μm thick Bosch polysilicon as well as differences between fatigue behavior of 10μm and 20μm thick

Bosch specimens, cannot be directly explained with any of known mechanisms.

Structural differences such as double thickness result in different average crystal size, lower share of grain boundaries, different texture as well as differences resulting from trenching process such as different roughness of the side walls, could be responsible for different flaw distributions in the volume as well as on the surface in the 10μm and 20μm thick polysilicon layers. A different stress distribution in the grain boundaries and triple points resulting from different elastic behavior of and size of grains, could be responsible for different defect growth.

The investigations of polysilicon under cyclic loading reveal two competing processes influencing the fracture strength of the material. The behavior of polysilicon, observed in experiment, is a sum of influences from processes of strengthening and fatigue. The share of single influences depends on the loading characteristics and should be seen as an 'chemical-like' equilibrium.

The schematics of the mechanism proposed is presented in Fig. 6.25.

As a result of investigations, on the process of fatigue and strengthening, following boundary conditions for both processes have been observed.
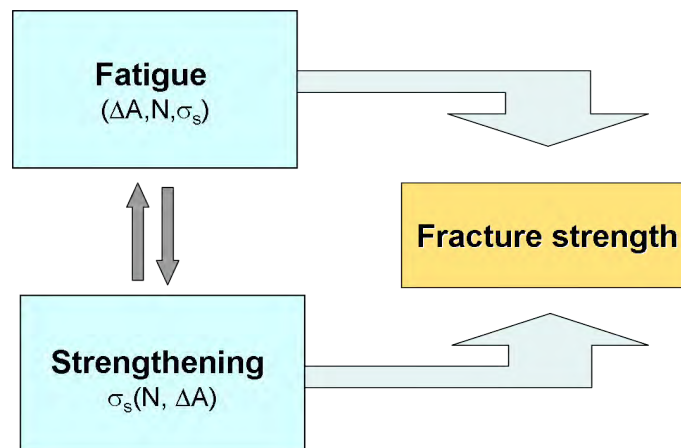
Figure 6.25: Equilibrium between fatigue and strengthening process in polysilicon under cycling loading

A decrease of the fracture strength (fatigue) depends on a number of cycles 'N' and a mechanical amplitude $\Delta\sigma$. A decrease of the fracture strength is observed in a ramp-up test (in comparison to static strength measurement) and during cyclic loading with a constant amplitude above 3000 MPa.

As it is shown in Fig. 5.25 the strengthening process depends on the number of cycles 'N' before the ramp-up test and is proportional to the amplitude of oscillations $\Delta\sigma$. After approximately 10^{11} cycles, in the test conditions, the fracture strength reaches its maximum. A strengthening is observed in a cyclic loading with amplitudes lower than 3000 MPa.

It should be assumed that a strengthening is present during the ramp-up test as well. During this time the specimen performs approximately 10^6 cycles.

An inability to examine changes in the *polycrystalline* silicon on the level of grain boundaries before and after the test, makes the definition/separation of typical fractographic features, representative for fatigue and strengthening, extremely difficult.

Based on the results of static and dynamic testing, as well as the similarity of fractured surfaces created in both regimes of loading, it is assumed that the fracture origin is placed on the surface or directly under the side surface of specimens. The defects with a size of a few nanometers are expected to be created in the exposed grain boundaries on the side of specimens. Crack growth on the interface between a silicon bulk and a 'side layer' is activated by mechanical loading and supported by the presence of chemical impurities.

The strengthening should be connected to development of compressive stress, reduction of tensile stress in the crack neighborhood or blunting of the crack tip. The existence of microcracking has been excluded in the investigations. Precise explanation of strengthening process on the atomic level has not been achieved in the thesis.

Based on knowledge about behavior of polysilicon under cyclic loading in the low pressure atmosphere, and taking into account known boundary conditions for processes of fatigue and strengthening it should be possible to complement the design rules for polysilicon MEMS. Using appropriate oscillation profile it would be theoretically possible to profit from the strengthening process in the testing or calibration phase for every new MEMS device. Results clearly show that the tuning of the trenching process could be the cost effective and successful way to extend MEMS reliability and give more tolerance for design of future generations.

The author is not aware of any publication reporting strengthening in monocrystalline silicon in literature. In order to confirm the role of grain boundaries in the fatigue/strengthening process a ramp-up and fatigue testing of monocrystalline silicon processed with the same form/roughness of the side wall should be conducted.

7

Summary

Motivated by a very fast progression in the field of MEMS technology, a key role of the polycrystalline silicon, and very high requirements for products in automotive applications author has investigated the fracture strength and fatigue behavior of Bosch polycrystalline silicon.

10 and 20μm thick n-doped, epitaxially deposited, polysilicon layers of columnar structure were investigated. In order to characterize the fracture strength, specimens with different sizes and geometries were designed and tested. Extensive Finite Element simulations have been applied to find out a correlation between mechanical deflection (force), and stress distribution in specimens. 'L'-shaped specimens with different width of the beams, size of mounting radius and mounting types were used to verify the process stability defined as a deviation of mechanical properties between charges deposited at different times. The tendency that 'L'-shaped specimens with notch anchor type (smaller area under high stress) have on average 18% higher fracture strength than the 'L'-shaped specimens with smooth anchor type (bigger area under high stress) has been observed. This indicates the applicability of a 'size effect' to Bosch polysilicon. Other measurements on straight and notched tensile specimens have shown an influence of stress concentration elements on the fracture strength of brittle materials. Also the results of three-point-bending specimens have shown an importance of the 'size effect' that should be taken into account when designing functional structures from polycrystalline silicon and other brittle materials.

Fracture strength has been correlated with effective volume and effective surface of all specimens calculated with software STAU with the assumption of Weibull m=7.9. Applicability of statistical methods based on weakest link theory in the prediction of fracture strength of polysilicon specimens has been evaluated with a positive outcome. Material scale parameters σ_{0A} and σ_{0V} have been estimated to be 3734 $MPa \cdot (meters)^{2/m}$ and 5413 $MPa \cdot (meters)^{3/m}$ respectively. However, the accuracy of predictions based on effective surface and effective volume are in the same range (-0.8% and -4.6% respectively). It should be emphasised that prediction based on effective surface has a smaller confidence interval

in the whole range of Weibull 'm' parameter. It has been shown that the statistical methods of strength prediction should be an integral part of MEMS design procedure.

Fractographic analysis has given an insight into fracture mechanism and helped to identify typical fracture modes and defects types. The roughness of the side-walls has been correlated with fracture strength and has given an indication that quality of the surface has a very important influence on the fracture strength of specimens. This observation has been consistent with successful prediction of fracture strength based on effective surface (assumption: the defect responsible for the fracture is placed on surface of the material). Measurements on specimens fabricated with different trench profile (trench param.) also support the thesis. The author has observed the modification of polysilicon structure caused by the trench process. The results have indicated that the interface between the volume of the material and a 'side-layer' might also be a weak point in the material. An average defect size for 10μm thick specimens estimated based on more than 1000 measured structures is 11nm. Maximal estimated defect size is 81nm.

It should be underlined that the typically measured fracture strength in the range of 3 - 5GPa and even for the lowest measured values of approx. 1.4 MPa, measured for biggest straight tensile specimens with the highest effective surface and volume, are a great deal higher than stresses in any Bosch MEMS application.

The fracture strength of 20μm thick specimens was lower than the strength of 10μm specimens. The experimental results were, in principle, consistent with expectations, taking into account a size effect although the differences in microstructure such as average crystal size, texture and side wall roughness made an important contribution to the results.

In order to investigate a fatigue behavior of 10 and 20μm thick polysilicon layers rotation oscillators working with a resonance frequency of approx. 90kHz were designed (R=-1). Specimens were tested in the atmosphere of a glass-frit silicon package under a pressure of 2mbar. An electronic setup that allowed parallel testing of up to 32 specimens and was developed especially to meet the needs of the project.

The strength of the rotation oscillators was characterized statically, with the use of micromanipulator and in a ramp-up test where the specimen was driven in resonance with an increasing mechanical amplitude. The high-cycle tests up to more than 10^{11} cycles were performed. Results indicate fatigue already within the first 60 seconds of a ramp-up test for both polysilicon layers.

Besides fatigue, a strengthening caused by oscillations with mechanical amplitude of up to 3000 MPa was observed in 10μm polysilicon. Measurement results have been compared with literature and the applicability of known fatigue mechanisms was discussed. It has been shown that a reaction layer mechanism proposed by Muhlstein cannot explain experimental results. Fatigue results as well as strengthening reported by Kahn seem to be consistent with the phenomenon

observed in this work. However, the mechanism of strengthening based on plasticity of grain boundaries under compressive stress resulting in residues compressive stress in material was proved not to explain the strengthening in the Bosch material. No substantial residue compressive stress was present in specimens tested.

The mechanism explaining behavior of polysilicon under cyclic loading has been proposed. The results revealed presence of two competing processes, strengthening and fatigue which influence fracture strength of the specimens. The chemical-like equilibrium between fatigue and strengthening depends on loading characteristics. The application of known boundary conditions for both processes allows to profit from the strengthening process and give clear direction for design of new MEMS generations.

8

Outlook

As the development of new materials and fabrication technologies continues, the need for reliability investigations will be strong. The trend of miniaturization will be the driving force for MEMS designers to get closer to material limits.

In this work, a big variety of specimens with different geometries and sizes were tested. Polysilicon layers with different thicknesses were investigated. Furthermore it has been shown that the statistic methods based on weakest-link theory can be successfully used in the strength prediction of brittle materials.

Accuracy of the prediction strongly depends on the number and quality of the prototype structures, fabricated from the same material, under the same conditions and tested in order to measure the fracture stress and Weibull parameter 'm' for known geometries. Statistic methods are based on the principle of comparison. Possible uncertainty in the estimation of defect distribution might have a colossal influence on the prediction results.

Obviously, an extension in the quantity of geometries tested, especially those with high effective volume and surface, would be of value for this work. The tensile testing setup available for the investigations was not free of specimens alignment issues. Further development of the test equipment should be in focus before a new charge of specimens will be tested. Placement of the setup in the chamber of a Scanning Electron Microscope, and application of image processing to measure the deflection, would lead to a substantial increase in accuracy.

The aim of the fatigue characterization performed in this thesis was to investigate the fatigue phenomenon, in the high cycle range, on a high number of specimens. The electronic testing setup was optimized to test up to 32 specimens in parallel. The major drawback of these solutions is the variation of the temperature of the specimens during in parallel. It has been shown, that for more precise measurements of frequency shift a system with controlled temperature should be considered. An optimal solution would be the availability of both systems at the same time, because the task of measuring the Woehler curve and the investigation of fatigue mechanisms are not redundant.

Crack growth investigations in resonant oscillators was infeasible during the

test. Access of precise microscopic methods to the specimens tested was not given due to the presence of the silicon glass-frit bonded package. Obviously, an opportunity to observe crack development or changes on the specimen's surface gives the investigator much more information needed to understand the failure mechanism. Nevertheless the task of this thesis was the characterization of fatigue behavior in a given package atmosphere.

In order to explain the phenomenon of fatigue and strengthening in polysilicon on the level of microstructure, similar measurements on single crystal silicon with the same quality of surface should be performed. High-cycle investigations should be also conducted on polysilicon layers of few different thicknesses fabricated with the same technology. A slight modification to the parameters of epitaxial deposition could modify the microstructure of the material, texture, the structure and the amount of grain boundaries as well. Comparison of all the experimental results joined with a detailed fractography could help us to separate influencing factors and contribute to better understanding of the root cause of the fatigue and strengthening mechanism.

Notation and Symbols

Symbols

a : Length of the crack

A_{eff} : Effective surface

c : half of the specimen's thickness

$\Delta\sigma$: amplitude in fatigue test

E : Young's modulus

F : force

$g(K_I, K_{II}, K_{III})$: mixed-mode failure criterion

I : moment of inertia of cross section

K_{Ic} : fracture toughness

K_{Ieq} : equivalent mode I stress intensity factor

m : Weibull parameter

M : maximum bending moment

P_f : faiulre probability

r_0 : equilibrium spacing between atoms

σ^* : maximal stress in the FE model

σ_0 : Weibull characteristic strength

σ_m : mean stress

σ_{0A} : material scale parameter

σ_A : maximal stress in point A

σ_c : cohesive stress

$\sigma(x, y, z)$: uniaxial stress at a point location (x,y,z)

V_{eff} : effective volume

$Y(a)$: geometric function

ρ : radius of curvature

Abbreviations

AFM : Atomic Force Microscopy

CCD : Charge-Coupled Device

$EBSD$: lectron Back Scattering Diffraction

ESP : Electronic Stability Program

FE : Finite Element

FEM : Finite Element Method

FIB : Focus Ion Beam

IC : integrated circuit

$MEMS$: Micro-Electro-Mechanical System

PC : Personal Computer

SEM : Scanning Electron Microscopy

$Secco\,etch$: Etch based on HF + $K_2Cr_2O_7 + H_2O$

$STAU$: STatistische AUswertung

TEM : Transmission Electron Microscopy

Zusammenfassung

Angeregt durch rapide Fortschritte im Bereich der MEMS Technologie (eine der Schlüsselanwendungen für polykristallines Silizium) und steigenden Anforderungen an Produkte für automobile Anwendungen, wurden im Rahmen dieser Dissertation Untersuchungen zur Bruch- und Dauerfestigkeit von polykristallinem Silizium durchgeführt.

Die untersuchten Polysiliziumschichten sind n-dotiert, epitaktisch abgeschieden worden und haben eine Dicke von 10 bis 20μm.

Um die Bruchfestigkeit zu ermitteln, wurden Proben unterschiedlicher Größe und Geometrie entwickelt, gefertigt und geprüft. Zur Bestimmung des Zusammenhanges zwischen mechanischer Dehnung und resultierender Spannungsverteilung innerhalb des Probenkörpers, sind umfangreiche Simulationen mit Hilfe der Finiten Elemente Methode durchgeführt worden.

Zur Ermittlung der Prozessstabilität, wurden Probekörper ('L'-Form) mit verschiedenen Schenkelweiten, Einspannradien und - art aus unterschiedlichen Fertigungschragen untersucht.

Auffällig ist, dass Probenkörper mit Kerbwinkeln (Spannungskonzentration auf geringer Fläche) eine durchschnittlich höhere Bruchfestigkeit (ca.18%) aufweisen, als Probekörper mit großflächiger Spannungsverteilung. Dies weist darauf hin, dass ein 'Größeneffekt' bei den Bosch-Polysilizium-Strukturen vorliegt. Mit weitere Messungen an glatten und gekerbten Zugproben konnte ein Einfluss von Strukturelementen zur gezielten Spannungskonzentration auf die Bruchfestigkeit spröder Materialien nachgewiesen werden. Die Ergebnisse aus Dreipunkt-Biegeversuchen zeigten ebenfalls einen deutlichen Einfluss des 'Größeneffekts', der folglich bei der Auslegung von Funktionsbauteilen aus Polysilizium oder anderen spröden Materialien berücksichtigt werden sollte.

Der Zusammenhang zwischen der Bruchfestigkeit und dem effektiven Volumen bzw. der effektiven Oberfläche wurde untersucht. Die effektiven Volumen und Flächen für alle Probenkörper wurden mit dem Programm STAU berechnet. Dabei wurde ein Weibull-Faktor von m=7.9 angenommen. Die Untersuchung der Anwendbarkeit statistischer Methoden, basierend auf der 'Weakest-Link-Theory' nach Weibull zeigte, dass diese zur Abschätzung der Bruchfestigkeit von Polysilizium geeignet sind. Die Materialwerte wurden dementsprechend zu $\sigma_{0A} = 3734$ $MPa{\cdot}(meters)^{2/m}$ und $\sigma_{0V} = 5413\ MPa{\cdot}(meters)^{3/m}$ festgelegt. Die Genauigkeit

der Abschätzungen basieren auf der effektiven Oberfläche und dem effektiven Volumen in einem vergleichbaren Bereich (-0.8% bzw. -4.6%). Dabei muss allerdings betont werden, dass Vorhersagen auf Basis der effektiven Oberfläche ein geringeres Vertrauensintervall bezüglich des Wertebereichs des Weibullparameters 'm' haben. Die Ergebnisse legen nahe, dass diese statistischen Methoden zur Ermittlung der Bruchfestigkeit als integraler Bestandteil in den Entwicklungsprozess mikroelektromechanischer Systeme integriert werden sollten.

Fraktographische Analysen lieferten einen Einblick in Bruchmechanismen und ermöglichten es, typische Brucharten und Fehlertypen zu identifizieren.

Einen wichtigen Einfluss auf die Bruchfestigkeit hat ebenfalls die Oberflächenqualität der Seitenwände. Diese Untersuchung stimmt mit den Annahmen der Bruchfestigkeit basierend auf der effektiven Oberfläche überein. Angenommen wird hierbei, dass der Bruch an der Oberfläche initiiert wird. Auch Messungen an Probekörpern mit unterschiedlichen Trenchprofilen stützen diese Theorie. Der Autor konnte Änderungen der Polysiliziumstruktur feststellen, die durch den Trenchprozess verursacht wurden. Die Ergebnisse zeigen, dass die Grenzfläche zwischen dem Körpervolumen und der Randschicht ebenfalls eine Schwachstelle darstellt.

Die durchschnittliche Defektgröße in mehr als 1000 Messungen bei Probekörpern mit einer Dicke von 10μm wurde zu 11nm abgeschätzt. Die maximale Fehlergröße beträgt 81nm.

Hierbei muss hervorgehoben werden, dass die typische gemessene Bruchfestigkeit im bereich zwischen 3 und 5 GPa lag. Selbst die geringsten gemessenen Werte von ca. 1.4 MPa, die an Zugproben mit glatter Oberfläche gemessen wurden, die dabei die größte effektive Oberfläche und Volumen aufwiesen, waren deutlich größer, als die Spannungen in sämtlichen Bosch MEMS Anwendungen.

Die Bruchfestigkeit von Proben mit Dicken von 20μm war geringer als diejenige von Proben mit 10μm Dicke. Dieses Versuchsergebnis stimmt mit der Vorhersage überein, dass sowohl der Größeneffekt als auch Unterschiede in der Mikrostruktur (Durchschnittliche Kristallgröße, Oberflächenstruktur, Rauheit der Seitenwand) die Bruchfestigkeit beeinflussen.

Um das Ermüdungsverhalten der 10 und 20μm Polysiliziumschichten zu untersuchen, wurden Rotationsschwinger mit einer Resonanzfrequenz von etwa 90kHz aufgebaut (R=-1). Die Probenkörper wurden dabei in der Atmosphäre eines Glas-Frit gebondeten Packages bei 2 mbar erprobt. Der elektrische Aufbau erlaubte dabei die parallele Erprobung von 32 Prüflingen und wurde speziell auf die Anforderungen des Projekts zugeschnitten.

Die Festigkeit des Schwingers wurde vor dem Langzeittest ermittelt. Es wurde sowohl ein Mikromanipulator eingesetzt, als auch die Probe in ihrer Eigenfrequenz angeregt um maximale Amplituden zu erzielen. Dabei wurden Tests mit mehr als 1011 Zyklen durchgeführt. Die Ergebnisse des Ramp-Up Tests an beiden Polysiliziumschichten lassen darauf schließen, dass bereits innerhalb der ersten 60

sec mit Ermüdung zu rechnen ist.

Neben der Ermüdung wurde bei Proben mit einer Schichtdicke von 10μm eine Festigkeitssteigerung beobachtet, die durch die Amplitudenanregung bis zu 3000 MPa verursacht wurde. Die Messwerte wurden mit bisherigen Literaturangaben verglichen und die Mechanismen diskutiert. Es konnte gezeigt werden, dass der 'Reaktionsschichtmechanismus' nach Muhlstein keine ausreichende Erklärung für die Ergebnisse liefert. Die Erkenntnisse von Kahn hinsichtlich Ermüdung und Festigkeitssteigerung scheinen jedoch in Übereinstimmungen mit den Ergebnissen dieser Arbeit zu stehen. Dennoch konnte der Verfestigungsmechanismus, der auf Plastizität der Korngrenzen unter Druckspannungen basiert, keine Erklärung für die Festigkeitssteigerung liefern, da keine erhebliche Restspannung in der Struktur festzustellen war.

Im Rahmen der Dissertation wurde ein Prozess zur Beschreibung des Verhaltens von Polysilizium unter zyklischer Belastung vorgeschlagen. Die Ergebnisse zeigen, dass sich zwei gegenläufige Effekte auf die Bruchfestigkeit der Probekörper auswirken. Zum Einen wirkt sich die Festigkeitssteigerung des Materials und zum Anderen der Ermüdungseffekt auf die Bruchfestigkeit aus. Das Gleichgewicht zwischen Ermüdung und Festigkeits- steigerung hängt dabei von der Art der Belastung ab. Die Anwendung und Umsetzung der durch die Untersuchungen bekannten Rahmenbedingungen für beide Prozesse ermöglicht somit, von der Festigkeitssteigerung zu profitieren und gibt dabei eine klare Richtung für die Gestaltung zukünftiger mikromechanischer Systeme vor.

Bibliography

[1] M. Gad-el Hak, editor. *The MEMS handbook*. CRC Press, 2002.

[2] B. Lawn. *Fracture of brittle solids*. Cambridge University Press, 2 edition, 1993.

[3] H. Kahn, L. Chen, R. Ballarini, and A.H. Heuer. Mechanical fatigue of polysilicon: Effects of mean stress and stress amplitude. *Acta Materialia*, 54:667–678, 2006.

[4] H. Kahn, R. Ballarini, J. Bellante, and A.H. Heuer. Fatigue failure in polysilicon not due to simple stress corrosion. *Science*, 298:1215–1219, November 2002.

[5] G. Stellman. Bruchmechanische zuverlässigkeitsaspekte mikromechanischer sensoren. Master's thesis, Universitaet Kassel and Robert Bosch GmbH, 2005.

[6] M. Offenberg, F. Larmer, B. Elsner, and H. Munzel. Novel process for a monolithic integrated accelerometer. In *Proceedings of the 8th International Conference on Solid-State Sensors and Actuators and Eurosensors IX*, pages 589–592, 1995.

[7] K. Glien, J. Graf, R. Mueller-Fiedler, H. Hoefer, M. Ebert, and J. Bagdahn. Strength and reliability properties of glass frit bonded micro packages. In *Proceedings of the Conference on Design, Test, Integration and Packaging of MEMS/MOEMS (DTIP)*, pages 119–124, Montreux, Switzerland, May 2004.

[8] T.L. Anderson. *Fracture Mechanics - Fundamentals and Applications*. CRC Press, 3 edition, 2005.

[9] O.N. Pierron and C.L. Muhlstein. The critical role of environment in fatigue damage accumulation in deep-reactive ion-etched single-crystal silicon structural films. *Journal of Microelectromechanical Systems*, 15(1):111–119, February 2006.

[10] K.-S. Chen and K.-S. Ou. Equivalent strengths for reliability assessment of mems structures. *Sensors and Actuators A: Physical*, 112:163–174, 2004.

[11] N.N. Nemeth, G.M. Beheim, O.M. Jadaan, W.N. Sharpe Jr., G.D. Quinn, L.J. Evans, and M.A. Trapp. Fracture strength simulation of sic microtensile specimens - accounting for stochastic variables. *Ceramic engineering and science proceedings*, 26(8):223–237, 2005.

[12] N.N. Nemeth, J.L. Palko, C.A. Zorman, O. Jadaan, and J.S. Mitchell. Structural modeling and probabilistic characterization of mems pressure sensor membranes. In *Proceedings of the MEMS: Mechanics and Measurements Symposium*, pages 46–51, June 2001.

[13] A. Brueckner-Foit, A. Heger, K. Heiermann, P. Huelsmeier, A. Mahler, A. Mann, and Ch. Zieger. *STAU 4 User's Manual*. Institut fuer Materialforschung II, Forschungszentrum Karlsruhe, 2003.

[14] W. Weibull. A statistical distribution function of wide applicability. *Journal of Applied Mechanics*, 18:293–297, 1951.

[15] K. Trustrum and A. De S. Jayatilaka. Statistical approach to brittle fracture. *Journal of Materials Science*, 12:1426–1430, 1977.

[16] K. Trustrum and A. De S. Jayatilaka. Applicability of weibull analysis for brittle materials. *Journal of Materials Science*, 18:2765–2770, 1983.

[17] K. Trustrum and A. De S. Jayatilaka. On estimating the weibull modulus for a brittle material. *Journal of Materials Science*, 14:1080–1084, 1979.

[18] H.A. Richard. Bruchvorhersagen bei ueberlagerter normal- und schubbeanspruchung von risen. *VDI Vorschungsheft*, 631(85), 1985.

[19] G. Schumiki and P. Seegebrecht. *Prozesstechnologie*. Springer-Verlag Berlin, 1991.

[20] T.I. Kamins. Design properties of polycrystalline silicon. *Sensors and Actuators A*, 21-23:817–824, 1990.

[21] M. Madou. *Fundamentals of microfabrication*. CRC Press, 1997.

[22] J.M. Bustillo, R.T. Howe, and R.S. Muller. Surface micromachining for microelectromechanical systems. In *Proceedings of the IEEE*, volume 86, pages 1552–1574, August 1998.

[23] H.-W. Zhou, B.G. Kharas, and P.I. Gouma. Microstructure of thick polycrystalline silicon films for mems application. *Sensors and Actuators A: Physical*, 104(1):1–5, March 2003.

[24] L. Michelutti, A. Chovet, J. Stoemenos, J.M.Terrot, and A.M. Ionescu. Polycrystalline silicon thin films for microsystems:correlation between technological parameters, film structure and electrical properties. *Journal of Thin Solid Films*, 401:235–242, 2001.

[25] P.J. French. Polysilicon: a versatile material for microsystems. *Sensors and Actuators A: Physical*, 99(1):3–12, April 2002.

[26] S. S. Dana, M. Anderle, G. W. Rubloff, and A. Acovic. Cvd growth of rough-morphology silicon films over a broad temperature range. *Applied Physics Letters*, 63(10):1387–1389, September 1993.

[27] P. Lange, M. Kirsten, J.A. Schweitz, F. Ericson J.R. Morante, W. Riethmuller, B. Wenk, and G. Zwicker. Thick polycrystalline silicon for surface-micromechanical applications: Deposition, structuring and mechanical characterization. *Sensors and Actuators A: Physical*, 54(1):674–678, June 1996.

[28] S. Greek, F. Ericson, S. Johansson, and J.-A. Schweitz. In situ tensile strength measurement and weibull analysis of thick film and thin film micromachined polysilicon structures. *Thin Solid Films*, 292(1):247–254, January 1997.

[29] J.A. Walker, K.J. Gabriel, and M. Mehregany. Mechanical integrity of polysilicon films exposed to hydrofluoric acid solutions. *Journal of Electronic Materials*, 20(9):665–670, 1991.

[30] R. Ballarini, H. Kahn, N. Tayebi, and A.H. Heuer. Effects of microstructure on the strength and fracture toughness of polysilicon: a wafer level testing approach. In C.L. Muhlstein and S. Brown, editors, *Mechanical Properties of Structural Films, STP 1413*, pages 37–51. ASTM, 2001.

[31] C.V. Thompson. Grain growth in polycrystalline thin films of semiconductors. *Interface Science*, 6(1-2):85–93, February 1998.

[32] John E Jr Sanchez. Effects of crystallographic orientation on film morphological evolution. In *Proceedings of the Material Research Society Symposium*, volume 343, pages 641–652, 1994.

[33] H. Kahn, A.Q. He, and A.H. Heuer. Homogeneous nucleation during crystallization of amorphous silicon produced by low-pressure chemical vapour deposition. *Philosophical Magazine A*, 82(1):137–165, 2002.

[34] M. Fuertsch, M. Offenberg, H. Munzel, and J.R. Morante. Influence of anneals in oxygen ambient on stress of thick polysilicon layers. *Sensors and Actuators A: Physical*, 76(1):335–342, August 1999.

[35] S. Lee, C. Cho, J. Kim, S. Park, S. Yi, J. Kim, and D.D. Cho. The effect of post-deposition processes on polysilicon young's modulus. *Journal of Micromechanics and Microengineering*, 8:330–337, 1998.

[36] B. Lee, L.J. Quinn, P.T. Baine, S.J.N. Mitchell, B.M. Armstrong, and H.S. Gamble. Polycrystalline silicon film growth in a sif4/sih4/h2 plasma. *Thin Solid Films*, 337(1-2):55–58, January 1999.

[37] B. Caussat, J. Couderc, L. Vasquez, A. Figueras, A. Vander Lee, D. Cot, J. Durand, V. Paillard, E. Scheid, B. de Mauduit, A. Vila, and J. Morante. Influence of deposit thickness on the mmicrostructure and surface roughness of silicon films deposited from silane. *Solid State Phenomena*, 67-68:125–130, 1999.

[38] R Angelucci, M. Severi, and S. Solomi. Effect of impurities on the grain growth of chemical vapor deposition polycrystalline silicon films. *Materials Chemistry and Physics*, 9:235–245, 1983.

[39] S. Kamiya, J. Kuypers, A. Trautmann, P. Ruther, and O. Paul. Annealing temperature dependent strength of polysilicon measured using a novel tensile test structure. In *The 17th IEEE International Conference on Micro Electro Mechanical Systems*, pages 185–188, 2004.

[40] J. Bagdahn, J. Schischka, M. Petzold, and Jr. Sharpe, W. N. Fracture toughness and fatigue investigations of polycrystalline silicon. In *SPIE - Reliability, Testing, and Characterization of MEMS/M0EMS*, volume 4558, pages 159–168, October 2001.

[41] W.N. Sharpe Jr., B. Yuan, and R.L. Edwards. Fracture tests of polysilicon film. In *Proceedings of the Materials Research Society Symposium*, volume 505, pages 51–56, 1997.

[42] H. Kahn, N. Tayebi, R. Ballarini, R.L. Mullen, and A.H. Heuer. Fracture toughness of polysilicon mems devices. *Sensors and Actuators A*, 82(1-3):274–280, 2000.

[43] R. Boroch, J. Wiaranowski, R. Mueller-Fiedler, M. Ebert, and J. Bagdahn. Characterization of strength properties of thin polycrystalline silicon films for mems applications. *Fatigue and Fracture of Engineering Materials and Structures*, 30(1):2–12, 2007.

[44] R.J. Myers and B.M. Hilberry. Effect of notch root radius on the fracture behaviour of monocrystalline silicon. In *Procedings 4th International Conference on Fracture*, pages 1001–1005, June 1977.

130

[45] C.L. Muhlstein, R.T. Howe, and R.O. Ritchie. Fatigue of polycrystalline silicon for microelectromechanical system applications: crack growth and stability under resonant loading conditions. *Mechanics of Materials*, 36:13–33, 2004.

[46] S. Kalainathan, R. Dhanasekaran, and P. Ramasamy. Grain size and size distribution in heavily phosphorus doped polycrystalline silicon. *Journal of crystal growth*, 104(2):250–256, 1990.

[47] R. Ballarini, R.L. Mullen, H. Kahn, and A.H. Heuer. The fracture toughness of polysilicon microdevices. In *Proceedings of Microelectromechanical Structures for Materials Research*, volume 518, pages 137–142, April 1998.

[48] M. Saif and N.C. MacDonald. Microinstruments for submicron material studies. *Journal of Materials Research*, 13(12):3353–3356, 1998.

[49] T. Tsuchiya, A. Inoue, and J. Sakata. Tensile testing of insulating thin films; humidity effect on tensile strength of sio2 films. *Sensors and Actuators A: Physical*, 82:286–290, 2000.

[50] T. Tsuchiya, O. Tabata, J. Sakata, and Y. Taga. Specimen size effect on tensile strengh of surface-micromachined polycrystalline silicon thin films. *Journal of Microelectromechanical Systems*, 7(1):106–113, March 1998.

[51] A. Corigliano, B. De Masi, A. Frangi, C. Comi, A. Villa, and M. Marchi. Mechanical characterization of polysilicon through on-chip tensile tests. *Journal of Microelectromechanical Systems*, 13(2):200–219, April 2004.

[52] B. De Masi, A. Villa, A. Corigliano, A. Frangi, C. Comi, and M. Marchi. On-chip tensile test for epitaxial polysilicon. In *The 17th IEEE International Conference on Micro Electro Mechanical Systems*, pages 129–132, 2004.

[53] W.N. Sharpe Jr., K.T. Turner, and R.L. Edwards. Tensile testing of polysilicon. *Experimental mechanics*, 39(3):162–170, September 1999.

[54] T. Ando, M. Shikida, and K. Sato. Tensile-mode fatigue testing of silicon films as structural materials for mems. *Sensors and Actuators A: Physical*, 93(1):70–75, August 2001.

[55] S. Johansson, J.-A. Schweitz, L. Tenerz, and J. Tiren. Fracture testing of silicon microelements in situ in a scanning electron microscope. *Journal of Applied Physics*, 63(10):4799–4803, 1988.

[56] K.P. Larsen, A.A. Rasmussen, J.T. Ravnkilde, M. Ginnerup, and O. Hansen. Mems device for bending test: measurements of fatigue and creep of electroplated nickel. *Sensors and Actuators A: Physical*, 103(1):156–164, January 2003.

[57] S. Johansson, J.-A. Schweitz, L. Tenerz, and J. Tiren. Fracture testing of silicon microelements in situ in a scanning electron microscope. *Journal of applied physics*, 63(10):4799–4803, 1988.

[58] J.A. Walker, K.J. Gabriel, and M. Mehregany. Mechanical integrity of polysilicon films exposed to hydrofluoric acid solution. In *Proceedings of the IEEE Micro Electro Mechanical Systems Workshop*, pages 56–60, February 1990.

[59] O. Tabata, K. Kawahata, S. Sugiyama, and I. Igarashi. Mechanical property measurement of thin films using load-deflection of composite rectangular membrane. In *Proceedings of the MEMS*, pages 152–156, February 1989.

[60] D. Maier-Schneider, A. Koprululu, S.B. Holm, and E. Obermeier. Elestic properties and microstructure of lpcvd polysilicon films. *Journal of Micromechanics and Microengineering*, 6:436–446, 1996.

[61] K. Petersen and C. Guarnieri. Young's modulus measurement of thin films using micromechanics. *Journal of Applied Physics*, 50(11):6761–6766, 1979.

[62] H.A.C. Tilmans. *Micro-Mechanical Sensors using Encapsulated Built-in Resonant Strain Gauges*. PhD thesis, MESA Research Institute of the University of Twente, Enschede, The Netherlands, 1993.

[63] L.M. Zhang, D. Uttamchandani, and B. Culshaw. Measurement of the mechanical properties of silicon resonators. *Sensors and Actuators A: Physical*, 29:79–84, 1991.

[64] H.-C. Tsai and W. Fang. Determining of poisson's ratio of thin film materials using resonant method. *Sensors and Actuators A: Physical*, 103:377–383, 2003.

[65] H. Kahn, S. Stemmer, K. Nandakumar, A.H. Heuer, R.L. Mullen, R. Ballarini, and M.A. Huff. Mechanical properties of thick, surface micromachined polysilicon films. In *Proceedings of the 9th IEEE International Workshop on Microelectromechanical Systems*, pages 343–348, February 1996.

[66] X. Li, B. Bhushan, K. Takashima, C.W. Baek, and Y.K. Kim. Mechanical characterization of micro/nanoscale structures for mems/nems applications using nanoindentation techniques. *Ultramicroscopy*, 97(1-4):481–494, 2003.

[67] S. Greek, F. Ericson, S. Johansson, M. Fuertsch, and A. Rump. Mechanical charakterization of thick polysilicon films: Young's modulus and fracture strength evaluated with microstructures. *Journal of Micromechanics and Microengineering*, 9:245–251, 1999.

[68] I. Chasiotis and W.G. Knauss. Tests with the aid of probe microscopy for the study of mems materials. In *Proceedings of SPIE*, volume 4175, pages 92–99, September 2000.

[69] W.G. Knauss, I. Chasiotis, and Y. Huanga. Mechanical measurements at the micron and nanometer scales. *Mechanics of Materials*, 35(3-6):217–231, 2003.

[70] T. Tsuchiya, O. Tabata, J. Sakata, and Y. Taga. Tensile testing of polycrystalline silicon thin films using electrostatic force grip. *T.IEE Japan*, 116-E(10):441–446, 1996.

[71] W.N. Sharpe Jr., B. Yuan, R. Vaidyanathan, and R.L. Edwards. Measurements of young's modulus, poisson's ratio, and tensile strengh of polysilicon. In *Proceedings of the 10th IEEE International Workshop on Micromechanical Systems*, pages 424–429, 1997.

[72] W.N. Sharpe Jr., B. Yuan, and R.L. Edwards. A new technique for measuring the mechanical properties of thin films. *Journal of Microelectromechanical Systems*, 6(3):193–199, September 1997.

[73] W.N. Sharpe Jr., B. Yuan, and R.L. Edwards. A new technique for measuring the mechanical properties of thin films. *Journal of Microelectromechanical Systems*, 6(3):193–199, 1997.

[74] T. Yi and C.-J. Kim. Tension test with single-crystalline-silicon microspecimen. In *Proceedings of MEMS, ASME International Mechanical Engineering Congress and Exposition*, volume 1, pages 81–86, November 1999.

[75] A. Villa, B. De Masi, A. Corigliano, A. Frangi, and C. Comi. Mechanical characterization of epitaxial polysilicon in mems. In *Proceedings of the 2nd MIT Conference on Computational Fluid and Solid Mechanics*, volume 1, pages 722–726, June 2003.

[76] T. Yi and C.-J. Kim. Measurements of mechanical properties for mems materials. *Measurement Science and Technology*, 10:706–716, 1999.

[77] G.L. Pearson, W.T. Read Jr., and W.L. Feldmann. Deformation and fracture of small silicon crystals. *Acta Metallurgica*, 5:181–191, 1957.

[78] H. Kapels, R. Aigner, and J. Binder. Fracture strength and fatigue of polysilicon determined by a novel thermal actuator. *IEEE Transitions on Electron Devices*, 47(7):1522–1528, July 2000.

[79] J.N. Ding, Y.G. Meng, and S.Z. Wen. Specimen size effect on mechanical properties of polysilicon microcantilever beams measured by deflection using a nanoindenter. *Materials Science and Engineering: B*, 83(1):42–47, 2001.

[80] S. Sundararajan, B. Bhushan, T. Namazu, and Y. Isono. Mechanical property measurements of nanoscale structures using an atomic force microscope. *Ultramicroscopy*, 91:111–118, 2002.

[81] S. Sundararajan and B. Bhushan. Development of afm-based techniques to measure mechanical properties of nanoscale structures. *Sensors and Actuators A: Physical*, 101:338–351, 2002.

[82] T. Namazu, Y. Isono, and T. Tanaka. Evaluation of size effect on mechanical properties of single crystal silicon by nanoscale bending test using afm. *Journal of Microelectromechanical Systems*, 9(4):450–458, December 2000.

[83] F. Carli, V. Benedetto, R. Cambie, and C. Combi. Polysilicon failure stress and young's modulus evaluation in mems devices. In *The 2003 ASME International Mechanical Engineering Congress and R&D Expo*, November 2003.

[84] A. Villa, B. De Masi, A. Corigliano, A. Frangi, and C. Comi. Mechanical characterization of epitaxial polysilicon in mems. In K.J. Bathe, editor, *Procedings Second MIT Conference on Computational Fluid and Solid Mechanics*, volume 1, pages 722–726. Elsevier, June 2004.

[85] F. Cacchione, A. Corigliano, B. De Masi, and M. Ferrera. Out of plane flextural behaviour of thin polysilicon films: mechanical characterization and application of the weibull approach. In *The 6th International Conference on Thermal, Mechanical and Multiphysics Simulation and Experiments in Micro-Electronics and Micro-Systems*, pages 100–104, April 2005.

[86] R. Ballarini, R.L. Mullen, and A.H. Heuer. The fracture toughness of polysilicon microdevices: A first report. *Journal of Materials Research*, 12(4):915–922, 1997.

[87] W.G. Knauss, I. Chasiotis, and Y. Huang. Mechanical measurements at the micron and nanometer scales. *Mechanics of Materials*, 35:217–231, 2003.

[88] A. Kelly. *Strong Solids*. Clarendon Press, Oxford, 1966.

[89] T. Tsuchiya. Tensile testing of mems materials. In *The 13th International Conference on Solid-State Sensors, Actuators and Microsystems*, pages 1953–1956, June 2005.

[90] J.N. Ding, Y.G. Meng, and S.Z. Wen. Specimen size effect on mechanical properties of polysilicon microcantilever beams measured by deflection using nanoindenter. *Materials Science and Engineering B*, 83:42–47, 2001.

[91] W.N. Sharpe Jr., S. Brown, G.C. Johnson, and W. Knauss. Round-robin tests of modulus and strength of polysilicon. In *Proceedings of the Materials Research Society Symposium*, volume 518, pages 57–65, April 1998.

[92] J. Bagdahn, W.N. Sharpe Jr., and O. Jadaan. Fracture strength of polysilicon at stress concentrations. *Journal of Microelectromechanical Systems*, 12(3):302–312, June 2003.

[93] O.M. Jadaan, N.N. Nemeth, J. Bagdahn, and W.N. Sharpe Jr. Specimen size effect on mechanical properties of polysilicon microcantilever beams measured by deflection using a nanoindenter. *Journal of Materials Science*, 38(20):4087–4113, 2003.

[94] E. Peeker. *Extended Numerical Modeling of Fatigue Behavior*. PhD thesis, Ecole Polytechnique Federale de Lausanne, 1997.

[95] J.A. Connally and S.B. Brown. Slow crack growth in single-crystal silicon. *Science*, 256(5063):1537–1539, 1992.

[96] M. Spearing. Strength characterization and analysis. In *Proceedings of Mechanical Reliability of Silicon MEMS - Recent progress and further requirements*, 27/28 February 2006.

[97] K. Minoshima, T. Terada, and K. Komai. Influence of nanometre-sized notch and water on the fracture behaviour of single crystal silicon microelements. *Fatigue and Fracture of Engineering Materials and Structures*, 23(12):1033, December 2000.

[98] J. Bagdahn and W.N. Sharpe Jr. Fatigue of polycrystalline silicon under long-term cyclic loading. *Sensors and Actuators A: Physical*, 103:9–15, 2003.

[99] J. Bagdahn and Jr. Sharpe, W. N. Reliability of polycrystalline silicon under long-term cyclic loading. *Sensors and Actuators A*, 103:9–15, 2003.

[100] T. Tsuchiya, A. Inoue, J. Sakata, M. Hashimoto, A. Yokoyame, and M. Sugimoto. Fatigue test of single crystal silicon resonator. In *Technical Digest of the Sensor Symposium*, volume 16, pages 277–280, June 1998.

[101] C.L. Muhlstein, S.B. Brown, and R.O. Ritchie. High-cycle fatigue and durability of polycrystalline silicon thin films in ambient air. *Sensors and Actuators A: Physical*, 94:177–188, 2001.

[102] W.W. Van Arsdell and S.B. Brown. Crack growth in polysilicon mems. In *Proceedings of the ASME Dynamic Systems and Control Division*, volume 66, pages 267–272, November 1998.

[103] W.W. Van Arsdell and S.B. Brown. Subcritical crack growth in silicon mems. *Journal of Microelectromechanical Systems*, 8(3):319–325, September 1999.

[104] S.M. Allameh, B. Gally, S. Brown, and W.O. Soboyejo. Surface topology and fatigue in si mems structures. In C.L. Muhlstein and S. Brown, editors, *Mechanical properties of structural thin films, STP 1413*, pages 3–16. ASTM, 2001.

[105] H. Kahn, R. Ballarini, R.L. Mullen, and A.H. Heuer. Electrostatically actuated failure of microfabricated polysilicon fracture mechanics specimens. *Proceedings: Mathematical, Physical and Engineering Sciences*, 455(1990):3807–3823, October 1999.

[106] C. Muhlstein and S. Brown. Reliability and fatigue testing of mems. In *Tribology Issues and Opportunities in MEMS, NSF/AFOSR/ASME Workshop*, pages 80–89, November 1997.

[107] C.L. Muhlstein, E.A. Stach, and R.O. Ritchie. A reaction-layer mechanism for the delayed failure of micron-scale polycrystalline silicon structural films subjected to high-cycle fatigue loading. *Acta Materialia*, 50:3579–3595, 2002.

[108] D.H. Alsem, E.A. Stach, C.L. Muhlstein, and R.O. Ritchie. Fatigue failure in thin-film polycrystalline silicon is due to subcritical cracking within the oxide layer. *Applied Physics Letters*, 86:041914, 2005.

[109] D.H. Alsem, E.A. Stach, C.L. Muhlstein, M.T. Dugger, and R.O. Ritchie. Utilizing on-chip testing and electron microscopy to study fatigue and wear in polysilicon structural films. In *Materials Research Society Symposium Proceedings*, volume 821, pages P2.5.1–6, 2004.

[110] C.L. Muhlstein, E.A. Stach, and R.O. Ritchie. Mechanism of fatigue in micron-scale films of polycrystalline silicon for microelectromechanical systems. *Applied Physics Letters*, 80(9):1532–1534, March 2002.

[111] C.L. Muhlstein and R.O. Ritchie. High-cycle fatigue of micron-scale polycrystalline silicon films: fracture mechanics analyses of the role of the silica/silicon interface. *International Journal of Fracture*, 119(4):449–474, 2003.

[112] C.L. Muhlstein, S.B. Brown, and R.O. Ritchie. High-cycle fatigue of single-crystal silicon thin films. *Journal of Microelectromechanical Systems*, 10(4):593–600, December 2001.

[113] S.M. Allameh, B. Gally, S. Brown, and W.O. Soboyejo. On the evolution of surface morphology of polysilicon mems structures during fatigue. In *Proceedings of the Materials Research Society Symposium*, volume 657, pages EE2.3.1–6, 2001.

136

[114] S.M. Allameh, P. Shrotriya, A. Butterwick, S.B. Brown, and W.O. Soboyejo. Surface topography evolution and fatigue fracture in polysilicon mems structures. *Journal of Microelectromechanical Systems*, 12(3):313–324, June 2003.

[115] W. Van Arsdell. *Sub-Critical Crack Growth in Polysilicon MEMS*. PhD thesis, Massachusetts Institute of Technology, 1997.

[116] H. Kahn, R. Ballarini, and A.H. Heuer. Dynamic fatigue of silicon. *Current Opinion in Solid State and Materials Science*, 8:71–76, 2004.

[117] H. Kahn, R. Ballarini, and A.H. Heuer. Surface oxide effects on static fatigue of polysilicon mems. In *Materials Research Society Symposium Proceedings*, volume 741, pages J3.4.1–6, 2003.

[118] H. Kahn, R. Ballarini, and A.H. Heuer. Surface oxide effects on static fatigue of polysilicon mems. In *Proceedings of the Materials Research Society Symposium*, volume 741, pages J3.4.1–6, December 2002.

[119] H. Kahn, R. Ballarini, and A.H. Heuer. Effects of varying mean stress and stress amplitude on the fatigue of polysilicon. In *Materials Research Society Symposium Proceedings*, volume 795, pages U4.7.1–9, 2004.

[120] W.N. Sharpe Jr., K.M. Jackson, K.J. Hemker, and Z. Xie. Effect of specimen size on young's modulus and fracture strengh of polysilicon. *Journal of Microelectromechanical Systems*, 10(3):317–325, September 2001.

[121] R. Boroch, W. Bernhard, K. Kehr, J. Hauer, and R. Müller-Fiedler. Fracture strength and the fatigue of polycrystalline silicon under static and long term high frequency cyclic load. In *Proceedings of the Conference on Design, Test, Integration and Packaging of MEMS/MOEMS (DTIP)*, May 2004.

[122] M. Ebert, S. Knorr, J. Bagdahn, R. Boroch, and R. Mueller-Fiedler. Consideration of measured grains orientations in numerical simulations of polycrystalline brittle materials for mems. In *Proceedings of 23rd CADFEM Users' Meeting 2005 International Congress on FEM Technology with ANSYS CFX and ICEM CFD Conference*, 9-11 November 2005.

[123] I. Chasiotis and W.G. Knauss. The mechanical strength of polysilicon films: Part 2. size effects associated with elliptical and circular perforations. *Journal of the Mechanics and Physics of Solids*, 51:1551–1572, 2003.

[124] W. Suwito, M. L. Dunn, and S.J. Cunningham. Fracture initiation at sharp notches in single crystal silicon. *Journal of Applied Physics*, 83(7):3574–3582, April 1998.

[125] Standard practice for reporting uniaxial strength data and estimating weibull distribution parameters for advanced ceramics - astm c1239-00. In *ASTM Book of Standards*, volume 15.01. ASTM International, March 2005.

[126] T. Yi, L. Li, and C.-J. Kim. Microscale material testing of single crystalline silicon: process effects on surface morphology and tensile strength. *Sensors and Actuators A: Physical*, 83:172–178, 2000.

[127] R.O. Ritchie. Mechanisms of fatigue-crack propagation in ductile and brittle solids. *International Journal of Fracture*, 100:55–83, 1999.

[128] W.N. Sharpe Jr. and J. Bagdahn. Fatigue testing of polysilicon - a review. *Mechanics of Materials*, 36:3–11, 2004.

[129] O.N. Pierron, D.D. Macdonald, and C.L. Muhlstein. Galvanic effects in si-based microelectromechanical systems: Thick oxide formation and its implications for fatigue reliability. *Applied Physics Letters*, 86:211919, 2005.

[130] M. Huh, Y. Yu, H. Kahn, J.H. Payer, and A.H. Heuer. Galvanic corrosion during processing of polysilicon microelectromechanical systems: The effect of au metallization. *Journal of the Electochemical Society*, 153(7):G644–G649, 2006.

[131] H. Kahn, Ch. Deeb, I. Chasiotis, and A.H. Heuer. Anodic oxidation during mems processing of silicon and polysilicon : Native oxides can be thicker than you think. *Journal of microelectromechanical systems*, 14(5):914.923, 2005.

[132] O.N. Pierron and C.L. Muhlstein. The extended range of reaction-layer fatigue susceptibility of polycrystalline silicon thin films. *International Journal of Fracture*, 135:1–18, 2005.

CURRICULUM VITAE

Robert Edward BOROCH

Personal Details:

Nationality	Polish
Age	27 years, born May 5th 1979
Sex	male
Address	e-mail: Robert.Boroch@gmail.com

Education:

Feb. 2003 - Jan. 2006	Industry Ph.D. at Robert Bosch GmbH, Corporate Research, Microsystems Technologies supervised by Prof. P. Gumbsch, University of Karlsruhe, Faculty of Mechanical Engineering. Subject: "Mechanical Properties and Fatigue of Polycrystalline Silicon under Static and High Frequency Cyclic Loading"
Oct. 1998 - June 2003	Warsaw University of Technology, Faculty of Chemistry Specialization: Solid State Characterization and Technology M.Sc. Thesis: "Novel polymer-in-salt electrolytes based on poly(N,N-dimethylacrylamide)". • Granted with Individual Program of Studies for outstanding results • Dean's scientific scholarship for the whole period of studies • For 5 years full-time study program graduation within 4 years with excellent result
Sept. 1994 - June 1998	"Stefan Batory" High School in Warsaw, Poland – extended program in Mathematics and Physics

Professional Experience:

Feb. 2006 -	Robert Bosch GmbH, Division: Automotive Electronics. Member of Centre of Competence for manufacturing processes with AE-wide responsibility for Al-thick wire bonding.
Feb. 2003 - Jan. 2006	Corporate Research of Robert Bosch GmbH, Microsystems Technologies
July – Oct. 2002	Robert Bosch GmbH, Forschung und Vorausentwicklung, Forschung Leitung Werstoffe.
August 2000	A/S Roulunds Fabriker - part of AP Moller (Maersk) Group, Odense, Denmark - non-obligatory practical training in R&D Department.
July - August 2001	Technische Universität Bergakademie Freiberg, Institute of Energy Processes and Chemical Engineering, Freiberg, Germany.

Computer Skills:

Operating systems	Windows (2000, XP) - very good Linux - good
Software	Ansys (FEM), Mathematica, MsOffice (full), Corel Draw, Adobe Photoshop

Languages:

Polish: mother tongue
English: very good
German: very good

Other Activities:

2007 -	Member of interdisciplinary network THESIS
2004 - 2006	Organizer and coordinator of "Arbeitskreis Werstoffe" for Ph.D. students of Robert Bosch GmbH
1998 - 2003	Member of International Association for the Exchange of Students for Technical Experience (IAESTE)
2000 - 2002	President of the IAESTE Local Committee in Warsaw – two terms of office. One term of office I was a member of Advisory Committee of IAESTE Poland.
1994 - 1998	Member of the Polish Scout Association

Hobbies: Geography was always my hobby. Hiking, badminton and fitness help me to feel fit. I am often traveling inspired with international and intercultural variety. Activities involving creation and organization are the source of my satisfaction.